Physik-Department
Institut für Hadronenstruktur und Fundamentale Symmetrien

Magnets, polarizers, systematics, and optimizations of the neutron-lifetime experiment PENeLOPE

Dipl.-Phys. Univ. Wolfgang Sebastian Schreyer

Vollständiger Abdruck der von der Fakultät für Physik der Technischen Universität München zur Erlangung des akademischen Grades eines Doktors der Naturwissenschaften genehmigten Dissertation.

Vorsitzender: Prof. Dr. Martin Beneke

Prüfende der Dissertation:

1. Prof. Dr. Stephan Paul
2. Prof. Dr. Lothar Oberauer

Die Dissertation wurde am 8. November 2016 bei der Technischen Universität München eingereicht und durch die Fakultät für Physik am 31. Januar 2017 angenommen.

The odyssey continues ...

Abstract

The beta-decay lifetime of free neutrons of $(880.3 \pm 1.1)\,\mathrm{s}$ plays an important role in Big Bang nucleosynthesis and the element V_{ud} of the CKM matrix. So far, measurements of the neutron lifetime relied on one of two different methods. Trap experiments store ultracold neutrons and count the remaining neutrons after different storage times. Beam experiments observe a beam of cold neutrons with known intensity and determine the rate of decay products—protons and electrons. Recently, the accuracy of trap experiments suffered from poor understanding of systematic effects and their measured lifetimes diverged from the less precise beam experiments.

The **P**recision **E**xperiment on **Ne**utron **L**ifetime **O**perating with **P**roton **E**xtraction (PENeLOPE) aims for a precision and accuracy of 0.1 s, one order of magnitude better than previous experiments. PENeLOPE will trap ultracold neutrons in a magnetic field with a strength of several Tesla produced by a superconducting multipole magnet and detect decay protons in situ, combining both types of experiments.

In a typical experimental cycle, PENeLOPE is filled with ultracold neutrons and absorbers remove marginally trapped neutrons that have energies high enough to overcome the magnetic trapping potential. Then, the superconducting magnet ramps up, ultracold neutrons are magnetically stored for up to several thousand seconds, and a proton detector determines the rate of neutron decay. At the end of the cycle, the superconducting magnet ramps down again and the remaining neutrons are counted.

In this thesis I follow such a cycle and show how each stage can introduce unwanted systematic effects. I show how these effects can be mitigated with polarized ultracold neutrons and a combined analysis of both measurement principles. I present an optimized geometry of the UCN inlet and arrangement of proton detectors, which improve statistical precision. I present design and test results of a prototype system to polarize ultracold neutrons in PENeLOPE. And I present results of successful tests of the first superconducting coils.

Kurzfassung

Die Lebensdauer des freien Neutrons von $(880{,}3 \pm 1{,}1)\,\mathrm{s}$ spielt eine wichtige Rolle für die primordiale Nukleosynthese und das Element V_{ud} der CKM-Matrix. Bisherige Messungen der Neutronenlebensdauer verwendeten zwei verschiedene Methoden. Speicherexperimente speichern ultrakalte Neutronen und zählen die verbliebenen Neutronen nach verschiedenen Speicherzeiten. Strahlexperimente beobachten einen Strahl kalter Neutronen mit bekannter Intensität und bestimmen die Rate der Zerfallsprodukte—Protonen und Elektronen. In den letzten Jahren mussten mehrere Ergebnisse von Speicherexperimenten nach unten korrigiert werden, da sich herausstellte, dass systematische Effekte ungenügend verstanden waren. Das führte zu einer Diskrepanz zwischen Speicherexperimenten und den bisher weniger genauen Strahlexperimenten.

Das **P**recision **E**xperiment on **Ne**utron **L**ifetime **O**perating with **P**roton **E**xtraction (PENeLOPE) soll die Neutronenlebensdauer mit einer um eine Größenordnung verbesserten Präzision von $0{,}1\,\mathrm{s}$ bestimmen. PENeLOPE wird ultrakalte Neutronen in einem einige Tesla starken Magnetfeld, erzeugt von einem supraleitenden Multipol-Magneten, speichern und parallel Zerfallsprotonen detektieren. Es stellt damit eine Kombination beider Arten von Neutronenlebensdauerexperimenten dar.

In einem typischen Experimentzyklus wird PENeLOPE mit ultrakalten Neutronen gefüllt und ein Absorber entfernt Neutronen mit Energien, die hoch genug sind um das magnetische Speicherpotential zu überwinden. Dann wird der supraleitende Magnet hochgefahren und die ultrakalten Neutronen werden für bis zu mehrere tausend Sekunden magnetisch gespeichert. Währenddessen bestimmt ein Protonendetektor die Rate des Neutronenzerfalls. Am Ende des Zyklus wird der Magnet wieder heruntergefahren und die verbliebenen Neutronen werden gezählt.

In dieser Arbeit folge ich einem solchen Zyklus und zeige, wie jede Phase des Experiments unerwünschte systematische Effekte verursachen kann. Ich zeige, wie diese Effekte mit polarisierten Neutronen und einer kombinierten Analyse beider Messprinzipien kompensiert werden können. Ich präsentiere eine optimierte Geometrie des Neutroneneinlasses und eine optimierte Anordnung der Protonendetektoren, um die statistische Genauigkeit zu verbessern. Ich präsentiere Design und Testergebnisse eines Prototyp-Systems zur Polarisation ultrakalter Neutronen in PENeLOPE. Und ich zeige die Resultate erfolgreicher Tests der ersten supraleitenden Spulen.

Contents

1 Introduction

1.1 A short history of the neutron

In 1930, Bothe and Becker [1] saw first signs of a new, neutral radiation while bombarding different elements with alpha particles. Unfortunately, they mistook it for gamma radiation. In the following year, Chadwick [2] showed in a series of experiments that this radiation consisted of particles with a mass close to that of a proton. The discovery of these neutrons won him the Nobel prize in 1935.

Heisenberg [3] quickly proposed that neutrons are part of atomic nuclei, resolving many issues of the prevailing proton-electron model of early nuclear physics. In 1934, Fermi [4] realized that an unstable neutron could also explain nuclear beta decays—postulating the existence of the neutrino in the process.

Since free neutrons are not stable, they have to be produced in nuclear reactions. The study of neutron production, absorption, and scattering mechanisms ultimately led to the discovery of nuclear fission by Meitner and Frisch [5] and Hahn and Strassmann [6], and found large-scale applications in nuclear weapons and power generation.

1.2 Ultracold neutrons

Neutrons produced in nuclear reactions typically have energies of several mega-electronvolts. Their lack of electric charge makes it impossible to accelerate, guide, or focus them into an experiment. However, when elastically scattered on light nuclei with low neutron-absorption cross sections, the neutrons lose large parts of their energy until their temperature equalizes with the surrounding material in a process called moderation.

Depending on the temperature of the moderating material, the energies of the neutrons are reduced to milli-electronvolts or less (table 1.1). These thermal, cold, and very cold neutrons have wavelengths so long that their interaction with matter is dominated by coherent scattering on collections of nuclei and can be described by a uniform optical potential.

This optical potential is small compared to the energies of thermal, cold, and very-cold neutrons, but they are still reflected when hitting a material at glancing angles. This effect can be used to build neutron guides allowing transport of neutrons to experiments.

A special case are ultracold neutrons (UCN). Their energy is so low—less than 300 neV—that they are reflected by the optical potential of some materials at all incident angles. Their temperature is less than 3 mK and cannot be achieved by classical moderation.

Several methods to produce large numbers of ultracold neutrons have been implemented. Wavelengths and energies of very cold neutrons can be Doppler-shifted on

Table 1.1: Classification of neutrons in energy and velocity regimes.

Class	Energy (µeV)	Velocity ($\mathrm{m\,s^{-1}}$)
thermal	10 000 to 50 000	1400 to 3100
cold	50 to 10 000	100 to 1400
very cold	0.3 to 50	8 to 100
ultracold	<0.3	<8

moving neutron mirrors [7, 8]. Very cold neutrons can be vertically extracted from their source, slowing them down to ultracold velocities [9]. And a special moderation process can directly produce ultracold neutrons in super-thermal sources. Super-thermal sources use a moderator with a dispersion relation of phonons[1] that intersects the dispersion relation of free neutrons once at thermal energies and once at energies close to zero. Scattering thermal neutrons off the moderator can excite a phonon and reduce the neutron energy to almost zero. The moderator is cooled to cryogenic temperatures to reduce the population of excited phonon states and the probability of the inverse process—upscattering an ultracold neutron on an excited phonon. Most current sources [10–15] and all future sources [16–18] are super-thermal sources using either super-fluid helium or frozen deuterium as moderator.

Ultracold neutrons have energies so low that they can be significantly influenced by gravity and strong magnetic fields. Gravitational acceleration, g_0, acting on the mass, m_n, and a magnetic field acting on the magnetic moment, μ_n, yield potentials[19]

$$m_\mathrm{n} g_0 = 102.519\,455\,56(64)\,\mathrm{neV\,m^{-1}} \text{ and} \tag{1.1}$$

$$\mu_\mathrm{n} = 60.307\,740(15)\,\mathrm{neV\,T^{-1}}. \tag{1.2}$$

One can use these potentials and the optical potential of suitable materials to trap and observe ultracold neutrons for hundreds of seconds.

1.3 Neutron lifetime

Due to their lack of electric charge, free neutrons—especially ultracold neutrons—are an ideal tool to study the underlying strong, weak, and gravitational forces, unhampered by the electromagnetic force. Precise measurements of the basic properties of neutrons, such as mass, charge, lifetime, decay modes, magnetic dipole moment, and electric dipole moment helped cementing the foundations of the Standard Model of particle physics.

The beta decay of a free neutron into a proton, an electron, and an electron antineutrino,

$$\mathrm{n} \rightarrow \mathrm{p} + \mathrm{e}^- + \bar{\nu}_\mathrm{e}, \tag{1.3}$$

is especially interesting. Measurements of asymmetries in the decay of polarized neutrons yield the ratio, λ, of axial-vector coupling strength to vector coupling strength of the weak

---

[1] Other solid-state excitations—like rotons and spinons—often play a role, too.

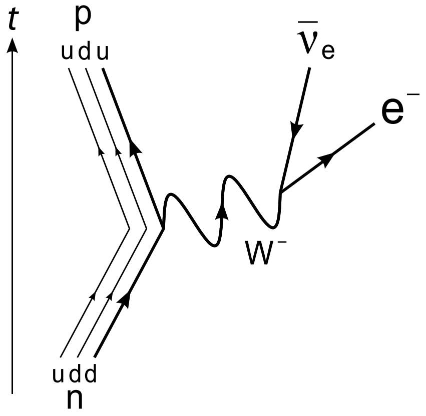

Figure 1.1: Feynman diagram of the beta decay of a free neutron. [20]

interaction. Additionally, such measurements could give indications of physics beyond the $V - A$ theory of the Standard Model in form of a tensor coupling.

1.3.1 Unitarity of the CKM matrix

The neutron lifetime, τ_n, depends on the probability of charged-current conversion of a down quark into an up quark (figure 1.1), which is proportional to the squared CKM-matrix element V_ud [21],

$$|V_\mathrm{ud}|^2 = \frac{(4908.7 \pm 1.9)\,\mathrm{s}}{\tau_\mathrm{n}\,(1+3\lambda^2)}, \tag{1.4}$$

with a theoretical uncertainty in the calculation of radiative corrections. With this relation, measurements of the neutron lifetime and the ratio λ can determine V_ud. Together with measurements of V_us and V_ub, or V_cd and V_td one can test the unitarity of the CKM matrix, a fundamental prediction of the Standard Model.

Currently, the most precise measurement

$$V_\mathrm{ud} = 0.97425 \pm 0.00022. \tag{1.5}$$

comes from experiments with $0^+ \to 0^+$ transitions in super-allowed nuclear beta decays [23]. The mean values and uncertainties obtained from neutron-decay measurements are (figure 1.2, [22]):

$$\tau_\mathrm{n} = (880.3 \pm 1.1)\,\mathrm{s}, \tag{1.6}$$

$$\lambda = -1.2723 \pm 0.0023, \text{and} \tag{1.7}$$

$$V_\mathrm{ud} = 0.97579 \pm 0.00061_\tau \pm 0.00146_\lambda \pm 0.00019_\mathrm{RC}. \tag{1.8}$$

Next-generation experiments like PENeLOPE and PERC [26] aim for a relative precision of 10^{-4} for the measurements of neutron lifetime and λ—an improvement by one order of magnitude. The resulting precision of V_ud would be similar or better than that from super-allowed decays and provide an independent check of CKM-matrix unitarity.

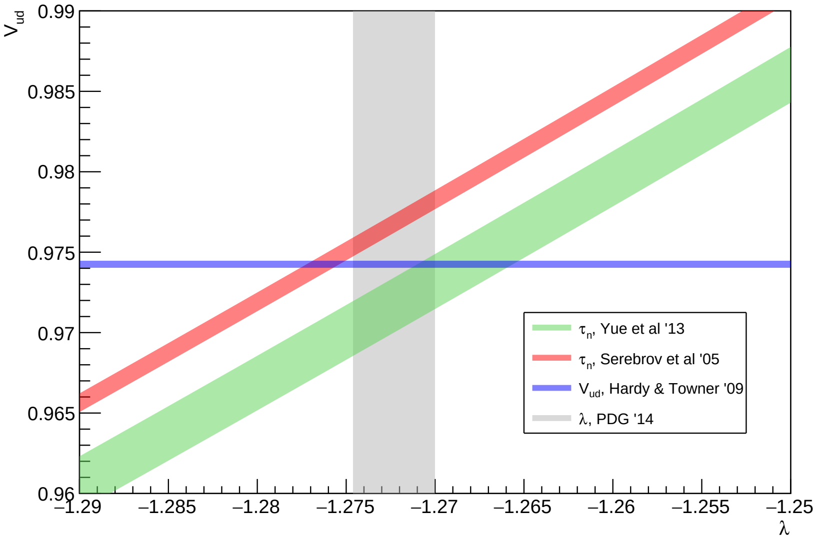

Figure 1.2: Mean values of λ [22] and V_{ud} (Hardy and Towner [23]) measurements and the most precise results from neutron-lifetime measurements with beam (Yue et al. [24]) and trap experiments (Serebrov et al. [25]).

1.3.2 Big Bang nucleosynthesis

Less than one tenth of a second after the Big Bang, the matter in the universe consisted mostly of protons, neutrons, electrons, positrons, and neutrinos. Their densities were high enough that neutrinos regularly interacted with the other species. Since the temperature, $k_{\mathrm{B}}T$, was much larger than the mass difference between neutron and proton, $m_{\mathrm{n}} - m_{\mathrm{p}}$, of 1.293 MeV, protons and neutrons were in thermal equilibrium via the reactions

$$\begin{aligned} &\mathrm{n} + \nu_e \leftrightharpoons \mathrm{p} + \mathrm{e}^- \quad \text{and} \\ &\mathrm{p} + \bar{\nu}_{\mathrm{e}} \leftrightharpoons \mathrm{n} + \mathrm{e}^+, \end{aligned} \tag{1.9}$$

and the ratio of neutrons to protons was given by the Boltzmann factor

$$\frac{N_{\mathrm{n}}}{N_{\mathrm{p}}} = \exp\left(-\frac{m_{\mathrm{n}} - m_{\mathrm{p}}}{k_{\mathrm{B}}T}\right). \tag{1.10}$$

After one tenth of a second, the density dropped far enough that neutrinos started to decouple from the equilibrium and the forward reactions in (1.9) stopped. One second later the temperature dropped below 1 MeV, no new electrons and positrons were created, the reactions (1.9) stopped altogether, and the neutron-to-proton ratio froze out at a value of about 1/6. However, the neutrons were now free to decay. About 200 s later—when the temperature had dropped far enough that protons and neutrons started to fuse into deuterium and heavier elements—the neutron-to-proton ratio had shifted to about 1/7

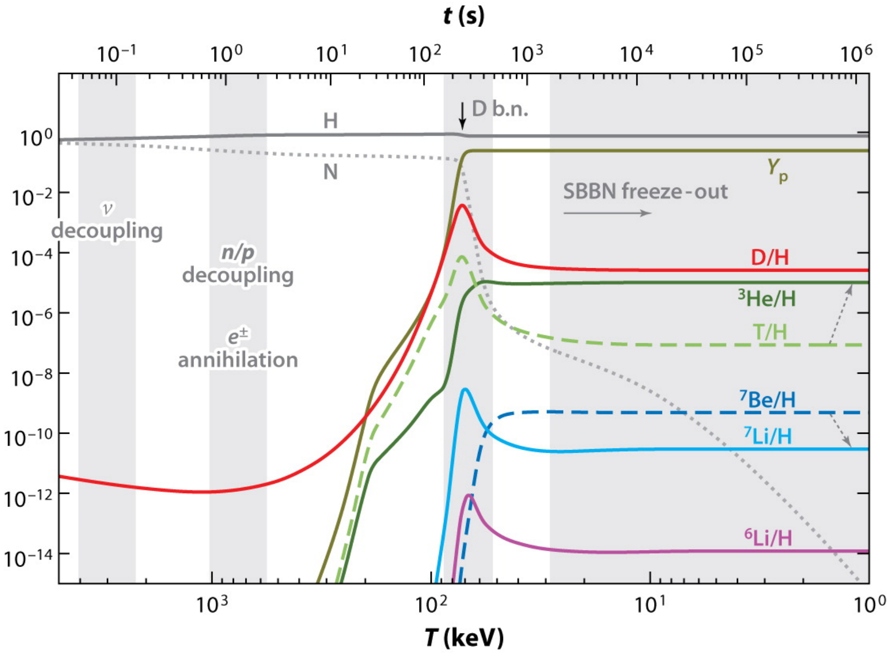

Figure 1.3: Time and temperature evolution of all nuclear abundances relevant for standard Big Bang nucleosynthesis (SBBN). [27]

(figure 1.3). The final abundances of the elements produced in this nucleosynthesis are strongly dependent on this ratio.

When modeling these processes, the neutron lifetime comes into play twice. It determines the rates of reactions (1.9) and the exact time of neutrino freeze-out. And it determines the reduction of the neutron-to-proton ratio between its freeze-out and the start of nucleosynthesis. The limited precision of the neutron lifetime therefore is the dominating uncertainty in these Big Bang-nucleosynthesis models.

1.3.3 Previous measurements

So far, the neutron lifetime has been determined with two different techniques—beam measurements and trap measurements.

In beam measurements, one observes a neutron beam and determines the decay rate from the rate of decay protons and electrons extracted from the beam. Such a measurement requires precise knowledge of intensity and volume of the observed neutron beam and extraction and detection efficiency for protons and electrons.

In trap experiments, ultracold neutrons are filled into a bottle, stored for some time, and then counted. Repeating this for longer and longer storage times yields an exponentially decreasing number of detected neutrons. The main uncertainty in this type of measurement are losses of UCN, e.g. during reflection from the trap walls, reducing the apparent lifetime of neutrons in the trap.

In the last years, the accuracy of several trap measurements suffered from insufficient

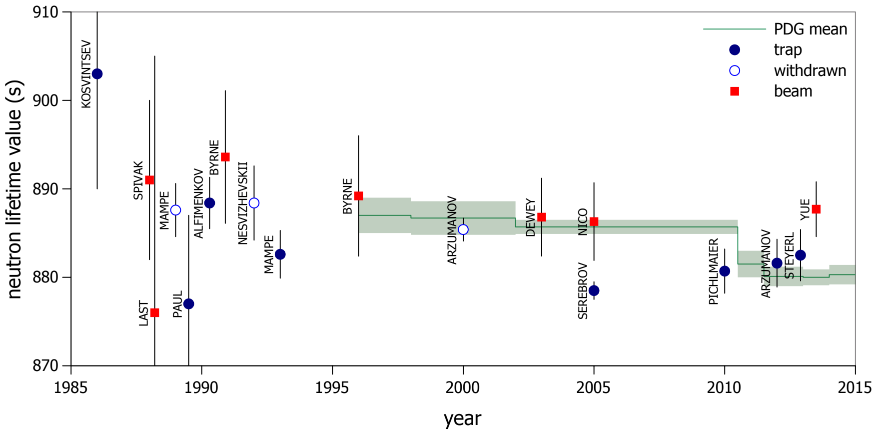

Figure 1.4: Previous measurements of neutron lifetime with beam and trap experiments. [22]

understanding of such losses [28, 29] and led to a large correction in the mean neutron lifetime compiled by the Particle Data Group (figure 1.4). This large shift in neutron lifetime also caused shifts in predictions from Big Bang nucleosynthesis and contributed to the reactor-antineutrino anomaly [30].

Meanwhile, Yue et al. [24] achieved major improvements in their beam measurement and determined a neutron lifetime of $(887.7 \pm 3.1)\,\mathrm{s}$. This value differs by three standard deviations from the most precise value obtained from a trap measurement, $(878.5 \pm 1.0)\,\mathrm{s}$, by Serebrov et al. [25].

1.4 PENeLOPE

1.4.1 Magnetic trapping of ultracold neutrons

Vladimirskiy [31] was the first to suggest magnetic traps for ultracold neutrons. A stack of magnets with alternating magnetization directions leads to a large magnetic-field gradient. Depending on the polarization of the magnetic moment, a neutron is either repelled (low-field-seeker) or attracted (high-field-seeker) by such a gradient (figure 1.5).

Paul et al. [32] and Ezhov et al. [33] first demonstrated magnetic trapping of neutrons using superconducting and permanent magnets. Several magnetic traps are operating or in construction, e.g. UCNτ [34], HOPE [35], τSPECT [36], and PENeLOPE.

Magnetic traps can completely eliminate losses of UCN at the walls. Additionally, the magnetic field can be designed such that decay protons and electrons can penetrate the magnetic barrier. Similar to beam measurements, a charged-particle detector behind the barrier can directly observe the exponentially falling decay rate of UCN in the trap and determine their lifetime—without knowledge of UCN density or detector efficiency.

Such a combination of beam- and trap-experiment techniques eliminates the dominant uncertainties of both types of experiment and could significantly improve the accuracy

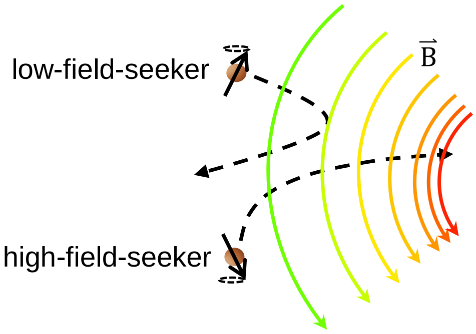

Figure 1.5: Repulsion and attraction of low- and high-field-seekers by a magnetic field gradient.

of neutron-lifetime measurements.

1.4.2 Description

The *Precision Experiment on Neutron Lifetime Operating with Proton Extraction* (PENeLOPE) aims to do such a combined measurement with a final precision of less than 0.1 s—one order of magnitude better than any previous measurement. The heart of the experiment is a magnetic trap with twenty-four superconducting coils, cooled by a liquid-helium reservoir, and isolated by a cryostat (figure 1.6). The coils are arranged in an outer and an inner cylindrical stack of nine and eleven coils with a height of 80 cm and an outer diameter of 1 m. Four bottom coils form the floor of the trap. The coils have alternating current directions to create the large gradient needed to trap low-field-seekers without wall contact. Low-energy UCN cannot leave the trap at the top due to gravity and it can remain open. Instead, a proton and electron detector can be placed there.

The total trap volume is 500 l. Its magneto-gravitational storage potential,

$$V = m_\mathrm{n} g z + \mu_\mathrm{n} B, \tag{1.11}$$

at a height z above the bottom coils can trap low-field-seekers with an energy of up to 115 neV without them being able to reach the walls or leave the trap (figure 1.7). Protons and electrons from decays of stored UCN are partly reflected by the magnetic-mirror effect in the field gradients at the walls and follow the field lines to the top of the trap where they can be detected. If the detector is placed on an electrical potential of at least −25 kV, the number of protons reaching the detector is significantly increased (see chapter 5.3).

In small parts of the storage volume, the magnetic fields of the coils cancel each other and the total field becomes zero. In these regions the spins of the trapped neutrons cannot align to the magnetic field and can be flipped—turning low-field-seekers into high-field-seekers, which are quickly lost. To avoid a distortion of the lifetime measurement, a large central current of at least 12 500 A running vertically through the center of the magnet creates an azimuthal field. This azimuthal field fills up the regions with zero field and

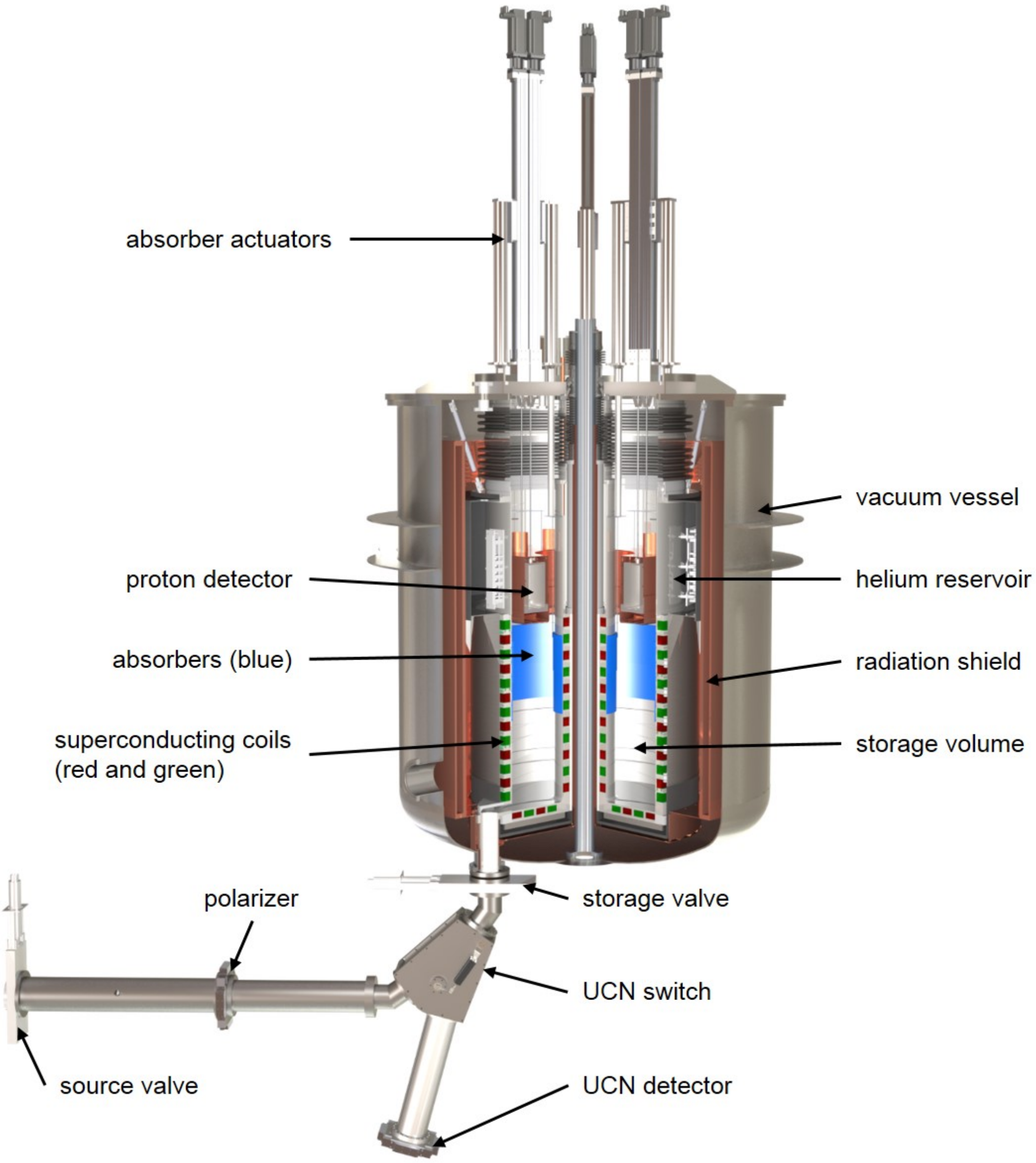

Figure 1.6: Rendering of cryostat and UCN guides of the PENeLOPE experiment.

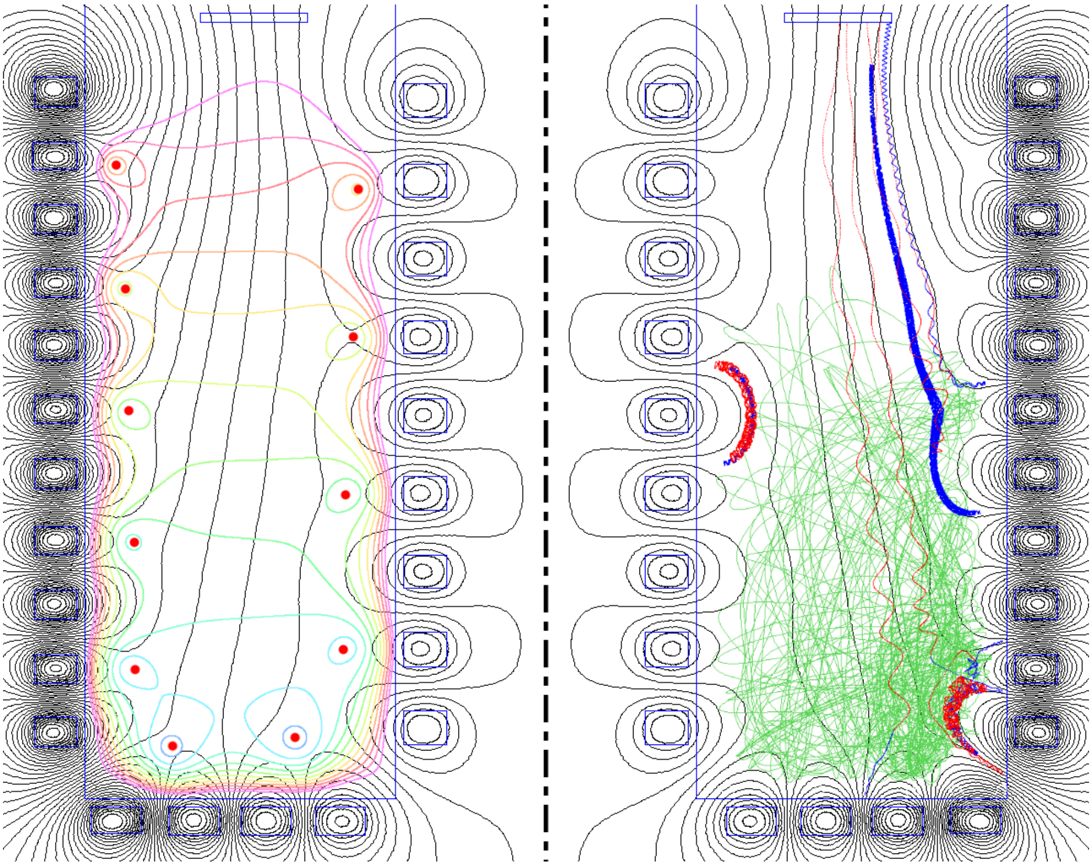

Figure 1.7: Cut view of PENeLOPE's magnet with magnetic field lines (black). Left: equipotential lines of the magneto-gravitational storage potential (colored) from 15 neV to 115 neV. Right: trajectories of low-field-seekers (green), beta-decay protons (red), and beta-decay electrons (blue). The proton detector (box above the storage volume) is placed on an electrical potential of −33 kV. The red dots on the left indicate regions where the magnetic field is zero.

reduces the probability of such spin flips. The inner coil stack is required to keep neutrons from hitting this central current.

PENeLOPE will be installed at the UCN source currently in construction at the Forschungs-Neutronenquelle Heinz Maier-Leibnitz (FRM II) [18]. Its expected UCN flux of $6 \cdot 10^5\,\mathrm{s}^{-1}\,\mathrm{cm}^{-2}$ yields a very small statistical uncertainty. These high statistics and the novel combination of neutron-lifetime measurements with its improved systematics will allow an unprecedented precision and accuracy.

2 Experimental stages of PENeLOPE

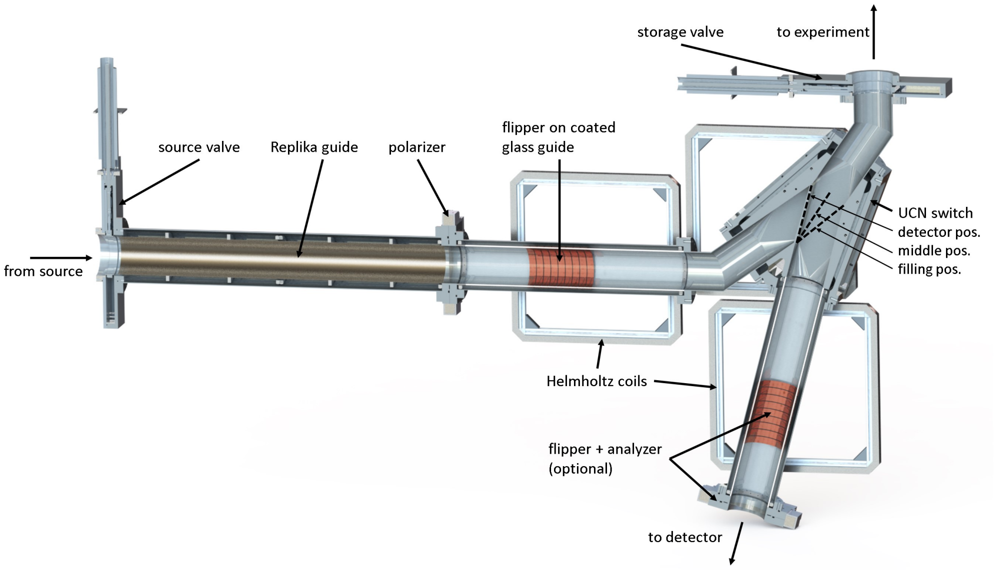

Figure 2.1: Cut through UCN guides, valves, and polarizers below PENeLOPE's cryostat.

A measurement cycle of PENeLOPE starts with a filling stage (see chapter 3). The magnet is powered down and both the source valve and the storage valve open (figure 2.1). UCN are transported from the source through the UCN switch in filling position into the storage volume. Since UCN leaving the solid-deuterium converter of the source get an kinetic-energy boost of 106 neV [37], the storage volume is located 1 m above the source level. The kinetic-energy spectrum of UCN entering the storage volume will be shifted down by the gravitational potential, into the energy range that can be magnetically stored. The storage volume fills with neutrons until, after about 200 s, a density plateau is reached. Then the storage valve and source valve close, the UCN switch moves into the middle position, UCN remaining in the guides between source and storage valve are dumped into the UCN detector, and the cleaning stage begins.

The cleaning stage is required to remove UCN with total energies above 80 neV, which would be sufficient to overcome the magneto-gravitational barrier during the storage phase. These marginally trapped neutrons would occasionally hit the walls of the storage volume even when the magnet is powered and can be lost there, reducing their lifetime in the trap and shifting the measured lifetime to smaller values. They are removed by

Table 2.1: Experimental stages of PENeLOPE

Stage		Valve positions Source v.	 Storage v.	 Switch	Duration (s)
I	filling	open	open	filling	∼200
II	cleaning	closed	closed	middle	150–200
III	ramping up magnet	closed	closed	middle	<100
IV	magnetic storage	closed	open	detector	variable
V	ramping down magnet	closed	open	detector	<100
VI	counting neutrons	closed	open	detector	∼200

two rings of neutron-absorbing material, suspended at a height of ca. 70 cm above the floor of the storage volume. Only UCN with total energies high enough to overcome the gravitational potential are able to reach this absorber. Picker et al. [38] showed the feasibility of this method in the preliminary Absorber Experiment AbEx.

After about 200 s of cleaning, the superconducting magnet is ramped up (see chapter 4). To minimize losses of UCN at the walls and due to beta decay, the magnet is ramped to its nominal current in less than 100 s. Low-field-seekers become trapped in the magnetic field while high-field-seekers are accelerated towards the walls of the storage volume.

Once the magnet has reached its nominal current, the storage valve opens again and any UCN trapped between storage valve and storage volume are dumped into the UCN detector. The absorbers move down to the bottom of the storage volume to remove almost all high-field-seekers. The large majority of remaining UCN are now losslessly trapped in the magnetic field. This marks the beginning of the magnetic-storage phase during which the proton detector can directly observe the beta decay of neutrons in the storage volume (see chapter 5).

After a storage time of up to several thousand seconds, the magnet is quickly ramped down again in less than 100 s. UCN remaining in the storage volume can leave the storage volume, enter the UCN detector, and are counted in the following 200 s (chapter 6).

This cycle is then repeated with varying storage times until the desired statistical precision is reached.

The following chapters describe each experiment stage in detail, potential systematic effects on the neutron-lifetime measurement associated with each stage, and measures to mitigate these effects. Chapter 3 describes the interaction of UCN with matter, an optimization of the filling and cleaning stages, and a method to pre-polarize UCN that are filled into the storage volume. Chapter 4 describes design and tests of the superconducting magnet. Chapter 5 describes a moving absorber to polarize UCN in situ and the general proton-detector concept. And chapter 6 describes a Bayesian analysis scheme for the neutron-lifetime measurement.

3 Stages I and II: Filling and cleaning

This chapter describes a model of the interaction of UCN with matter used to optimize the filling and cleaning stages with Monte Carlo simulations; design, construction, and test of a pre-polarizer for UCN; and potential systematic effects on the neutron-lifetime measurement that could be induced during the filling and cleaning stages.

3.1 Interaction of ultracold neutrons with matter

To be able to study the filling and cleaning processes we need a model to describe the interaction of ultracold neutrons with matter. Fermi [39] showed that interaction of ultracold neutrons with matter can be described with a complex potential

$$U = V - iW = \frac{2\pi\hbar^2}{m_\mathrm{n}} \sum_i n_i b_i, \tag{3.1}$$

where m_n is the neutron mass and n_i are the number densities of the nuclear species in the material. b_i are the complex-valued bound coherent scattering lengths, which can be related to the bound coherent scattering cross section [40]

$$\sigma_\mathrm{c} = 4\pi\, |b|^2 \tag{3.2}$$

and the loss cross section

$$\sigma_\mathrm{l} = \frac{4\pi}{k}\mathrm{Im}(b). \tag{3.3}$$

To simulate UCN interacting with matter reflection at material boundaries, transmission through material boundaries, and absorption in bulk material have to be considered.

Transmission

A neutron with energy E—traveling in a material with potential V and impinging on a surface in the y-z plane with potential V' at an angle θ_i—can be considered a planar wave, $\psi_\mathrm{i} = \exp(ikx)$, traveling in x direction with a wave vector $k = \sqrt{2m_\mathrm{n}E\cos^2\theta_\mathrm{i}}$. If the neutron's perpendicular energy component $E_\perp = E\cos^2\theta_\mathrm{i}$ is larger than the potential step at the boundary, $V' - V$, the waves

$$\psi_\mathrm{r} = R\exp(-ikx) \text{ and} \tag{3.4}$$

$$\psi_\mathrm{t} = T\exp(ik'x) \tag{3.5}$$

are reflected and transmitted with wave vectors

$$k = \frac{1}{\hbar}\sqrt{2m_\mathrm{n}E_\perp} \text{ and} \tag{3.6}$$

$$k' = \frac{1}{\hbar}\sqrt{2m_\mathrm{n}(E_\perp - (V' - V))}. \tag{3.7}$$

Demanding continuity at the boundary gives the reflected and transmitted waves' amplitudes:

$$R = \frac{k - k'}{k + k'} \tag{3.8}$$

$$T = \frac{2k}{k + k'}. \tag{3.9}$$

To get the actual reflection and transmission probabilities, r and t, the ratios of probability-current densities

$$\mathbf{j} = \frac{\hbar}{2m}(\psi^*\nabla\psi - \psi\nabla\psi^*) \tag{3.10}$$

have to be calculated:

$$r = \frac{j_\mathrm{r}}{j_\mathrm{i}} = |R|^2 = \left(\frac{k - k'}{k + k'}\right)^2 \tag{3.11}$$

$$t = \frac{j_\mathrm{t}}{j_\mathrm{i}} = \frac{k'}{k}|T|^2 = \frac{4kk'}{(k + k')^2}. \tag{3.12}$$

As expected, $r + t = 1$.

If the UCN has been transmitted into a material, its energy, $E_\perp$, and its velocity component perpendicular to the surface, $v_\perp = v\cos\theta_\mathrm{i}$, are changed due to the new potential. The velocity component parallel to the surface, $v_\parallel = v\sin\theta_\mathrm{i}$, remains unchanged. This results in a refraction of its velocity, similar to Snell's law:

$$\mathbf{v}' = \mathbf{v}_\parallel + \mathbf{v}'_\perp = \mathbf{v}_\parallel + \frac{k'}{k}\mathbf{v}_\perp = \mathbf{v} + \left(\frac{k'}{k} - 1\right)\mathbf{v}_\perp. \tag{3.13}$$

Absorption

Inside a material, the neutron can be absorbed and inelastically scattered. Inelastic scattering typically increases the neutron's energy far above the ultracold regime and the neutron is lost to any ultracold-neutron experiment.

As described in Golub et al. [41, chap. 2.4], such losses can be included with an imaginary potential, W, in the potential (3.1):[1]

$$W = \frac{2\pi\hbar^2}{m_n}\sum_i n_i \mathrm{Im}\,(b_i) = \frac{\hbar}{2}v\sum_i n_i\sigma_l^{(i)}. \tag{3.14}$$

---

[1] This expression is dependent on the neutron velocity v, but since σ_l is proportional to $1/v$, the potential W is independent of velocity.

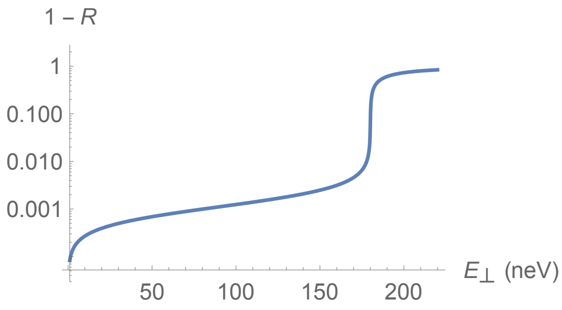

Figure 3.1: Probability that a UCN is not reflected on a stainless-steel surface with $U_{ss} = (183 + 0.0190\mathrm{i})\,\mathrm{neV}$.

Absorption cross sections are well documented—Sears [40] lists cross sections of a wide range of isotopes. The up-scattering cross section, however, depends on the temperature-dependent density of vibrational and rotational states of the material and is often dominated by impurities like hydrogen adsorbed at the surface. Thus, in most experiments, the up-scattering cross section is an unknown parameter that has to be adapted to experimental data to do reliable simulations.

Including this imaginary potential into the neutron's wave vector (3.7) gives

$$k = \sqrt{2m(E + iW)}/\hbar \tag{3.15}$$

and a decaying probability-current density

$$j \propto e^{-2\mathrm{Im}(k)x}. \tag{3.16}$$

Total reflection

If the perpendicular energy component of the neutron is smaller than the potential step at the material boundary it cannot be transmitted,[2] only reflected. However, the neutron penetrates into the new material as an evanescent wave and can be lost there. This behavior is described by equation (3.11), if the wave vector k' is modified:

$$k' = \frac{1}{\hbar}\sqrt{2m(E_\perp - (V' - V) + iW')}. \tag{3.17}$$

This yields a small absorption probability even in case of total reflection (figure 3.1).

Diffuse reflection

Smooth surfaces of typical neutron guides mainly reflect specularly; i.e. the outgoing polar angle, θ, is equal to the incoming angle, θ_i, and the outgoing azimuth, φ, is rotated by 180° to the incoming azimuth, φ_i. The reflected intensity is then

$$I_\mathrm{s}(\theta_\mathrm{i}, \theta, \varphi)d\Omega \propto \frac{1}{2\pi}\delta\left(\theta - \theta_\mathrm{i}\right)\delta\left(\varphi - \varphi_\mathrm{i} - \pi\right)d\Omega. \tag{3.18}$$

---

[2] Except in the case of tunneling, which can be neglected except for very thin films.

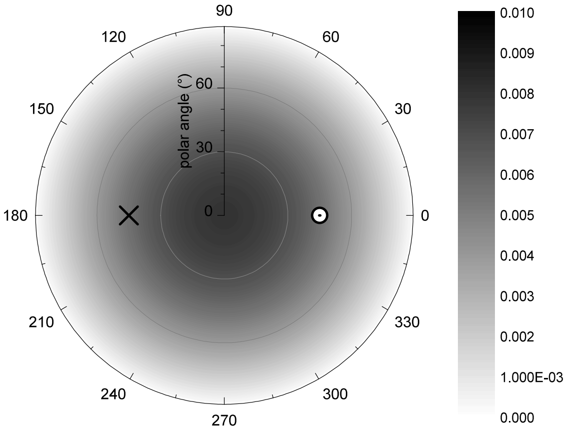

Figure 3.2: Intensity of Lambertian reflection, I_L, with 5 % total probability. The cross indicates the incoming direction, the dot the direction of specular reflection.

However, a certain percentage of reflections—usually in the order of 1 % to 10 % for typical UCN guide surfaces [42]—is diffuse. The diffuse-reflection distribution is often modeled with a simple Lambert model with a $\cos\theta$-distributed outgoing intensity and a predefined probability P_L of diffuse reflection (figure 3.2):

$$I_\mathrm{L}(\theta)d\Omega = \frac{P_\mathrm{L}}{\pi}\cos\theta d\Omega. \tag{3.19}$$

Steyerl [43] worked out the scattering distributions more rigorously for surfaces with small roughness and an isotropic short-range correlation of gaussian form and established the micro-roughness model. It gives scattering distributions for reflection (figure 3.3),

$$I_+\left(k,\theta_\mathrm{i},\theta,\varphi\right)d\Omega = \frac{k_\mathrm{l}^4}{4\cos\theta_\mathrm{i}}\left|S\left(\theta_\mathrm{i},k\right)\right|^2\left|S\left(\theta,k\right)\right|^2 F\left(k,\theta_\mathrm{i},\theta,\varphi\right)d\Omega, \tag{3.20}$$

and for transmission (figure 3.4),

$$I_-\left(k,\theta_\mathrm{i},\theta,\varphi\right)d\Omega = \frac{k_\mathrm{l}^4}{4\cos\theta_\mathrm{i}}\frac{k'}{k}\left|S\left(\theta_\mathrm{i},k\right)\right|^2\left|S\left(\theta,k'\right)\right|^2 F\left(k,\theta_\mathrm{i},\theta,\varphi\right)d\Omega, \tag{3.21}$$

where

$$S\left(\theta,k\right) = \frac{2\cos\theta}{\cos\theta+\sqrt{\cos^2\theta-k_\mathrm{l}/k}} \tag{3.22}$$

is the incoming, reflected, or transmitted amplitude and

$$F\left(k,\theta_\mathrm{i},\theta,\varphi\right) = \frac{b^2w^2}{2\pi}\exp\left[-\frac{k^2w^2}{2}\left(\sin^2\theta_\mathrm{i}+\sin^2\theta-2\sin\theta_\mathrm{i}\sin\theta\cos\varphi\right)\right] \tag{3.23}$$

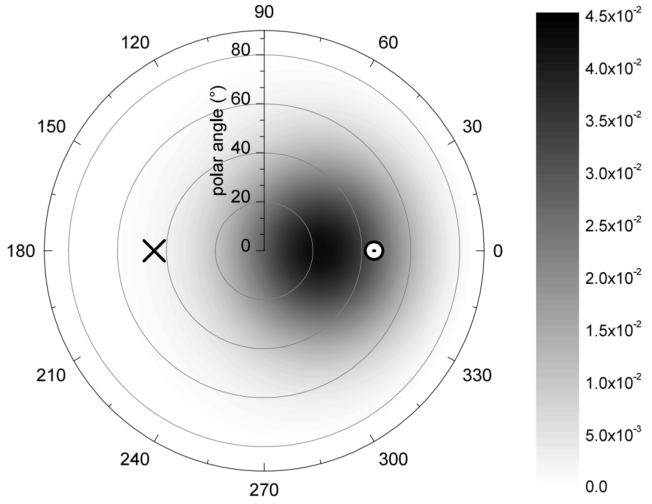

Figure 3.3: Intensity of micro-roughness reflection, I_+, of a UCN with an energy of 150 neV and an incident angle of 45° on a stainless-steel surface with a potential of 183 neV, a roughness amplitude of 2.5 nm, and a correlation length of 20 nm—resulting in a total diffuse-reflection probability of 4.9 %. The cross indicates the incoming direction, the dot the direction of specular reflection.

is the Fourier transform of the correlation function characterizing the surface with a mean roughness amplitude b, a correlation length w, and a critical wave number

$$k_\mathrm{l} = \frac{1}{\hbar}\sqrt{2m_\mathrm{n}\left(V' - V\right)}. \tag{3.24}$$

Equations (3.20) and (3.21) are properly normalized and the total probability of diffuse scattering is the integral over the scattering hemisphere

$$P_\mathrm{d}\left(k, \theta_\mathrm{i}\right) = \int_{2\pi} I_\pm\left(k, \theta_\mathrm{i}, \theta, \varphi\right) d\Omega = \int_0^{\pi/2}\int_0^{2\pi} I_\pm\left(k, \theta_\mathrm{i}, \theta, \varphi\right) d\varphi \sin\theta d\theta, \tag{3.25}$$

which can be split into two integrations over φ and θ. Only the correlation function (3.23) is relevant to the φ integration, which can be solved with the identity

$$\int_0^{2\pi} \exp\left(x\cos\varphi\right) d\varphi = 2\pi I_0(x) \tag{3.26}$$

with the modified Bessel function of the first kind I_0. The remaining one-dimensional θ integration can be done very quickly with numerical quadrature—e.g. an adaptive Gauss-Kronrod algorithm as included in Bochkanov [44].

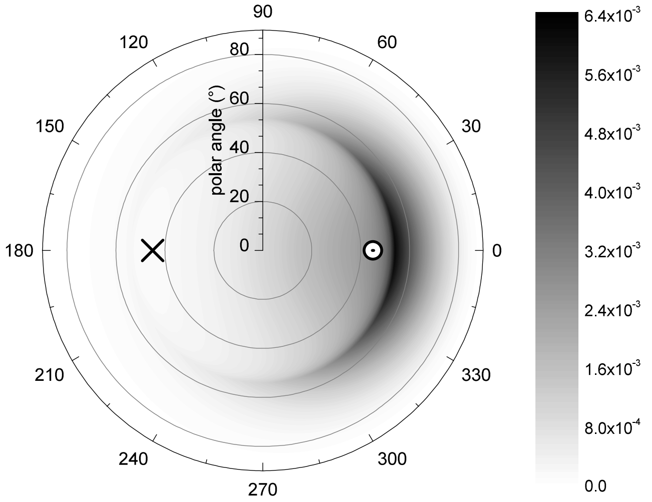

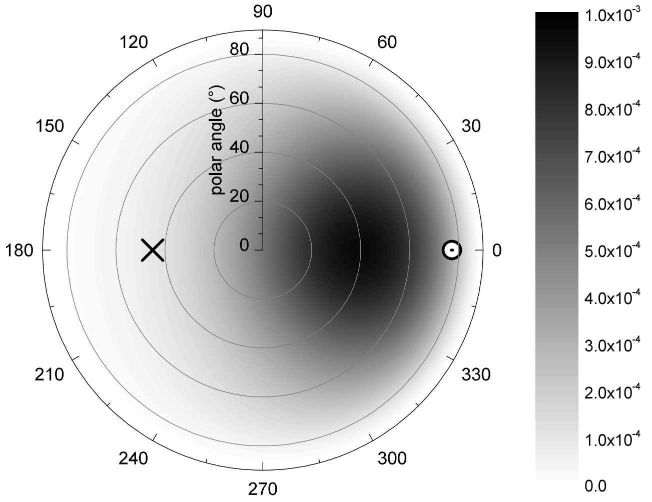

Figure 3.4: Intensity of micro-roughness reflection, I_+, (top) and transmission, I_-, (bottom) of a UCN with an energy of 150 neV and an incident angle of 45° on an aluminium surface with a potential, V', of 54 neV, a roughness amplitude of 2.5 nm, and a correlation length of 20 nm. The cross indicates the incoming direction, the dot the direction of specular reflection (top) and transmission according to Snell's law (bottom). If the reflected angle is larger than the critical angle, i.e. $E\cos^2\theta < V'$, the reflection probability sharply increases, leading to a ring structure in the distribution (top).

Simulations

Specular reflection and Lambert reflection were already included in my simulation code PENTrack, as described in Schreyer [45]. To be able to study the filling and cleaning stages in more detail, I also implemented transmission, absorption in matter, and micro-roughness reflection.

The experiment geometry can be imported into the simulation from almost all computer-aided design software via the StL format, which describes the geometry's surfaces with triangle meshes [46]. PENTrack can detect collisions of a particle with such a surface with the Computational Geometry Algorithms Library [47]. This easy-to-use geometry import allowed me to simulate different experiment geometries and optimize them.

3.2 Optimization of the neutron feeder

To achieve a neutron-lifetime measurement with high precision, the number of UCN in PENeLOPE's storage volume after filling and cleaning should be as large as possible. The geometry of the UCN guide feeding neutrons into the storage volume is crucial to this task and should provide

- a high UCN density,
- a long material-storage lifetime of magnetically trappable UCN, and
- a short cleaning stage.

The length of the cleaning stage is determined by the material-storage lifetime of marginally trapped neutrons with an energy above 80 neV. After cleaning, their number should be 10 000 times smaller than the number of magnetically trappable UCN with an energy below 80 neV—as shown in section 6.1.3.

3.2.1 Comparison of feeder topologies with Monte Carlo simulations

With these goals in mind I simulated several different feeder shapes using PENTrack:

- the original, very large feeder volume below the storage volume, connecting both via eight inlets (figure 3.5a);
- a ring-shaped feeder volume, reaching around the storage volume, and connecting both via eight inlets (figure 3.5b);
- and very small feeders, connecting the UCN guides directly to the storage volume (figure 3.5c).

In the simulations, PENeLOPE was filled for 200 s, then the valves closed and marginally trapped neutrons were removed for 200 s (figure 3.6). To determine the optimal cleaning time, I fit an exponential to the fraction of marginally trapped neutrons in the storage volume and extrapolated to a fraction of 10^{-4}.

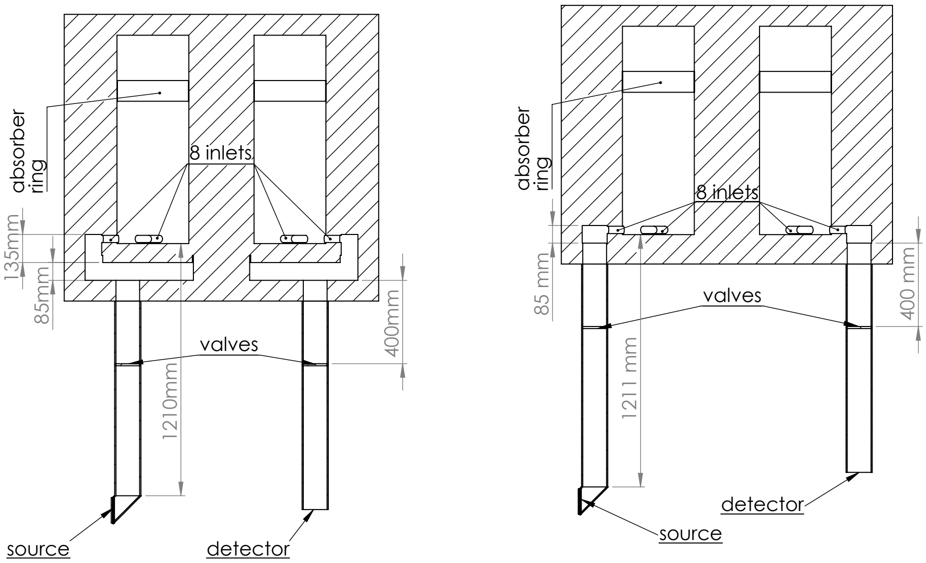

(a) Original feeder volume

(b) Ring-shaped feeder volume

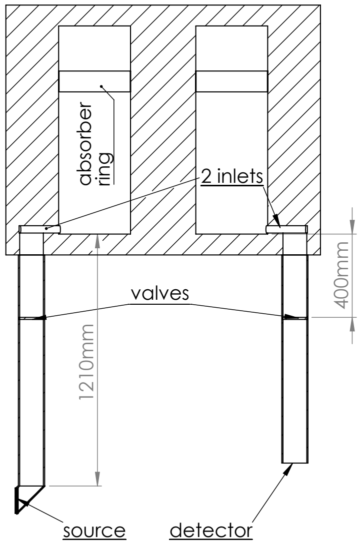

(c) Two guides, small feeder

Figure 3.5: Cutaway view of simulation geometries used in the feeder optimization.

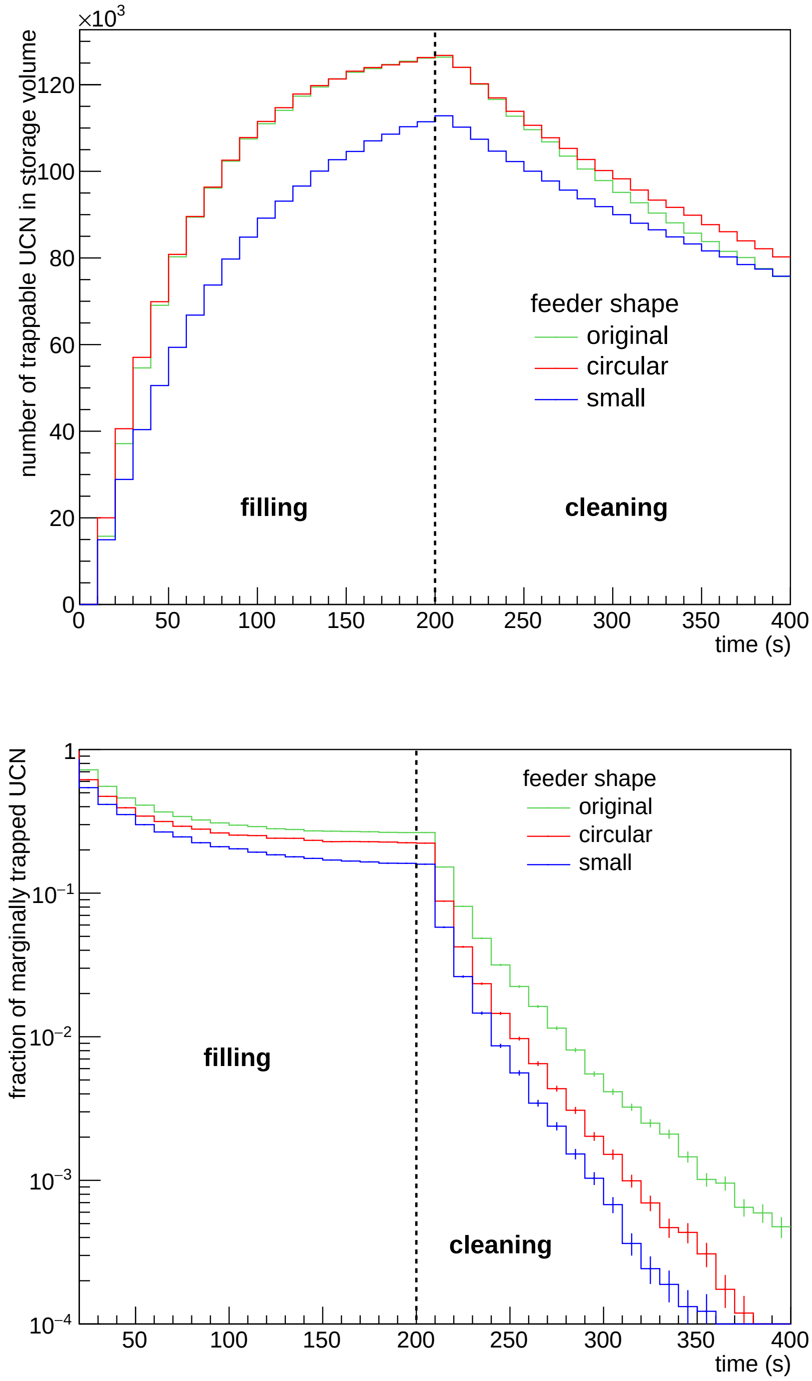

Figure 3.6: Number of trapped UCN (top) and fraction of marginally trapped UCN (bottom) in the storage volume during filling and cleaning for different feeder shapes. Optimistic surface properties are assumed.

Table 3.1: Optimal cleaning times and relative UCN densities after the optimal cleaning times for different feeder configurations. Optimistic surface properties are assumed.

		Relative UCN density (%)	
Feeder	Optimal cleaning time (s)	after filling	after cleaning
original	250	100	100
ring-shaped	180	100	125
small (two guides)	150	90	125

The energy spectrum of UCN from a solid-deuterium source has an offset of about 106 neV [37]. Since PENeLOPE cannot store UCN with more than 80 neV, they have to be slowed down. For every feeder shape and simulation run, I kept the height of the storage volume above the source at roughly 1.2 m, corresponding to a gravitational potential that the UCN have to overcome of 123 neV. Each inlet had a cross section of 62 cm^2 and I attached ideal UCN valves with no leakage 0.4 m below the feeder.

Optimistic surface properties

At first, I assumed that the guides are made of nickel, with an optical potential of $(245 - 0.0297\mathrm{i})$ neV, and the storage vessel is made of stainless steel, with an optical potential of $(183 - 0.0190\mathrm{i})$ neV.

The simulations showed that the original feeder shape was far from optimal (table 3.1). Although the initial UCN density in the storage volume is quite high, the material-storage lifetime is low due to the irregular shape and large surface-to-volume ratio of the feeder. The large surface area compared to the cross section of the inlets also reduces the chance of UCN in the feeder to reach the storage volume, making cleaning very inefficient and requiring a very long cleaning time of 250 s.

Additionally, the large feeder volume could potentially introduce another systematic effect: a small number of neutrons could be trapped inside the feeder volume during the storage phase, especially high-field-seekers. These would be detected together with the remaining stored neutrons once the magnet is ramped down and would directly impact the neutron-lifetime measurement.

The ring-shaped feeder allows similarly high UCN densities during filling but due to the smaller surface area cleaning is much more efficient, resulting in a 20 % to 25 % higher UCN density after the optimal cleaning time of 180 s.

With small feeder volumes directly connecting the guides to the storage volume, the UCN density after filling is 15 % lower than in the other cases. But due to the even shorter cleaning time of 150 s, the density after cleaning is comparable to that of the ring-shaped feeder volumes.

Table 3.2: Optimal cleaning times and relative UCN densities after the optimal cleaning times for different feeder configurations. Pessimistic surface properties are assumed.

		Relative UCN density (%)	
Feeder	Optimal cleaning time (s)	after filling	after cleaning
original	200	100	100
ring-shaped	150	107	170
small	150	97	180
small (single guide)	150	82	170

Pessimistic surface properties

The simulations so far used the ideal optical potential without taking into account upscattering. This lead to unrealistically high material-storage lifetimes of 400 s to 500 s. Hence, I used more pessimistic surface properties: I changed the guide material to stainless steel and increased the imaginary part of its potential by a factor of 4.5. This reduced the material-storage lifetime to 150 s to 250 s, which is closer to those achieved in experiments like AbEx [48].

The results in table 3.2 show that the changed surface properties further reduce the performance of the original feeder design. After the optimal cleaning times of 150 s, the ring-shaped feeder volume and the small feeder volumes directly connecting the guides to the storage volume achieve densities that are 70 % to 80 % larger.

A single feeder

To reduce complexity of the feeder assembly and heat transfer to the cold magnet, I finally simulated a configuration with only a single small feeder directly connecting a single guide to the storage volume. In this case, I attached an external UCN switch designed by Andreas Frei, guiding the neutrons either from the source into the experiment or from the experiment to the detector (figure 3.7). Due to this additional component, the UCN density after cleaning is reduced by about 10 % compared to the case with two guides (table 3.2). Since heat transfer through the feeder to the magnet is one of the main contributors to liquid-helium boil-off [49] and compensation of thermal contraction proved quite difficult (section 3.2.2), we accepted the small drop in UCN density and ultimately chose the single feeder as the best solution.

3.2.2 Detailed feeder design

Feeder shape

The ultracold-neutron guides that are planned to be used at the UCN source at FRM II have an inner diameter of 115 mm. The simulation results led to the requirement that the slot in the magnet support structure should have a cross section at least as large as

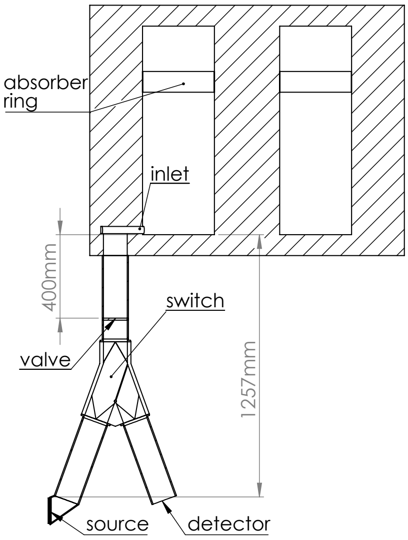

Figure 3.7: Cutaway view of a configuration with a small feeder and a single guide with UCN switch.

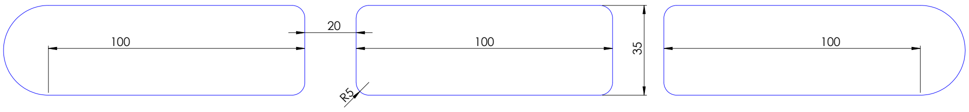

Figure 3.8: Cross section of the final design of the UCN inlet through the magnet structure. The area is about 115 cm^2.

the guide—104 cm^2 (figure 3.8). I simulated the connection of the feeder to this inlet in more detail to find the optimal shape. Several variations were considered (figure 3.9):

- an elbow-shaped feeder with a sharp 90° kink,
- a 45° elbow with and without a miter, and
- a smooth 60° bend,

each one smoothly tapered to the inlet through the magnet structure.

The results show that any reduction in cross section along the feeder—the 90° elbow (figure 3.9a) and the 45° elbow without miter (figure 3.9b)—reduce UCN density in the storage volume by about 10 % compared to the smoother feeders with large cross sections (figure 3.9c, 3.9d). The smooth bend was chosen as the final design.

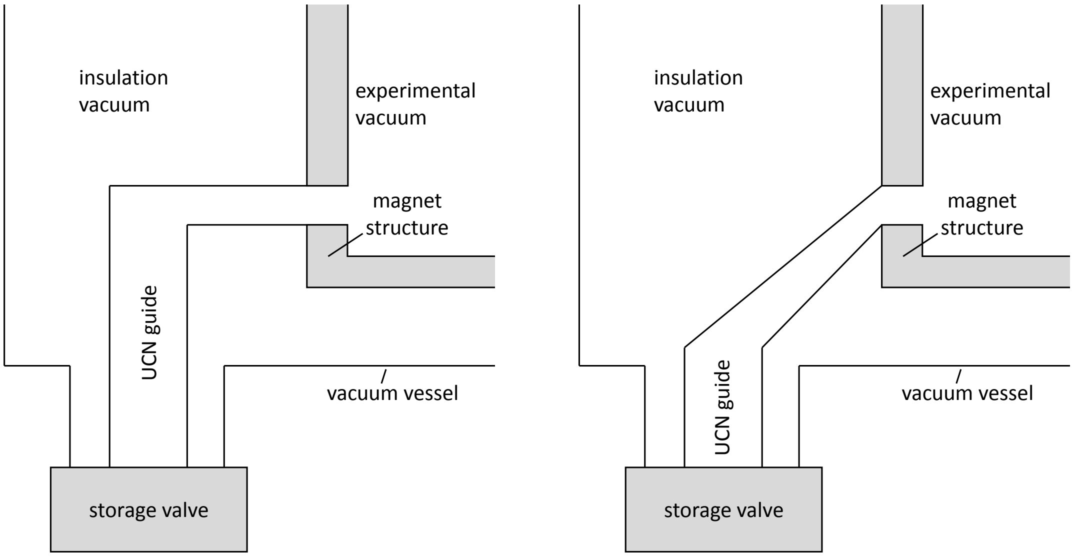

(a) 90° elbow

(b) 45° elbow w/o miter

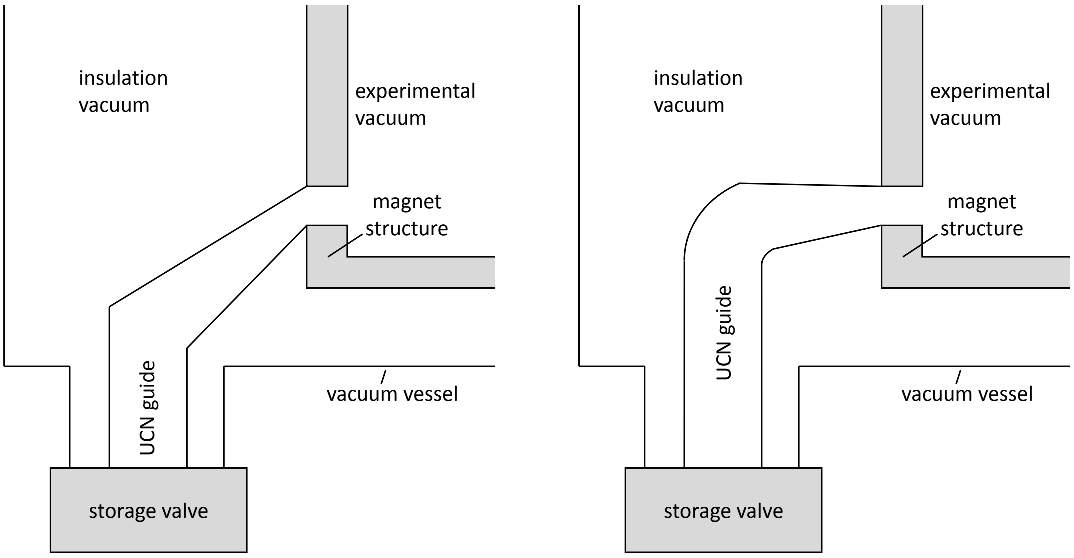

(c) 45° elbow w/ miter

(d) Smooth 60° bend

Figure 3.9: Simulated feeder shapes.

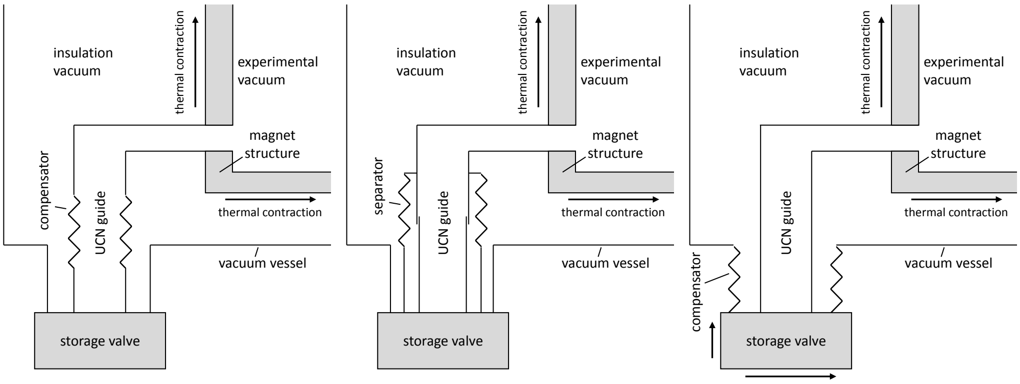

(a) Flexible feeder (b) Split feeder (c) Rigid feeder

Figure 3.10: Possible feeder schematics allowing compensation of thermal contraction and separation of vacua.

Feeder assembly

Since the feeder connects the liquid-helium-cooled magnet to the external UCN guides the feeder has to compensate the thermal contraction of the magnet during cool-down. The support structure of the magnet, made from stainless steel, experiences a contraction of $3\,\mathrm{mm\,m^{-1}}$ when cooled down from room temperature to $4\,\mathrm{K}$ [50]. Thus, the feeder will move up to $2.5\,\mathrm{mm}$ in radial and $6\,\mathrm{mm}$ in vertical direction. Additionally, to avoid losses during interaction of UCN and protons with rest gas, a very small rest-gas pressure of $10^{-8}\,\mathrm{mbar}$ or less is required [51]. Rest gas contamination of the storage volume can be greatly reduced if the insulation vacuum is separated from the experimental vacuum, further complicating the feeder design.

Three different feeder designs to fulfill these criteria were considered (figure 3.10):

- replacing the UCN guide with a flexible compensation bellow,
- splitting the guide and letting the lower half extend into the upper half with a larger diameter, or
- attaching the storage valve to a rigid guide so the valve also moves with the feeder. The thermal compensation would have to take place below the valve, outside of the storage volume.

The flexible feeder would be the mechanically simplest solution and would allow rather thin guide walls, reducing heat conduction from the storage valve to the magnet structure. However, the corrugated bellow surface reduces UCN transmission into the storage volume.

The split guide would improve transmission, but, since the guide is part of the storage volume during cleaning, any gaps in the guide will lead to a large reduction of UCN density. A 1-mm gap, corresponding to an area of $360\,\mathrm{mm}^2$, is almost as large as the effective loss area—the wall-loss probability multiplied by the surface area—of the whole storage volume—about $\approx 10^{-4} \cdot 8\,\mathrm{m}^2$—and would double the loss rate during the cleaning phase. This design should only be considered if the gap can be reduced to 0.1 mm or less. Since the split guide would no longer be vacuum tight, an additional separation bellow would have to be foreseen, further complicating assembly.

The last design, a rigid guide, would provide the best transmission and storage properties. It would, however, have to bear large forces: the weight of the storage valve and all forces required to deform the external compensators during thermal contraction. Depending on the required wall thickness, it might significantly increase heat conduction into the magnet structure and liquid-helium consumption.

During assembly, the whole magnet with the feeder is inserted into the vacuum vessel from the top and the feeder is threaded into the corresponding port at the bottom of the vacuum vessel. Finally, the storage valve is attached to the guide and the vacuum vessel is closed.

The split and rigid guides are prone to buckling and tearing during assembly and cool-down. Tolerances and forces would have to be tightly controlled to avoid time-consuming repairs.

When simulations showed that replacing the UCN guide with a flexible hydroformed bellow with 10 convolutions would reduce the intial UCN density by just 5 %, the choice ultimately fell onto this simplest solution.

3.3 Pre-polarization of ultracold neutrons

In Schreyer [45], I showed that UCN with magnetic moments parallel to the magnetic field, so called high-field-seekers, could introduce a sizable systematic effect to the lifetime measurement.

As shown in section 5.1, to achieve a lifetime-measurement accuracy better than 0.1 s, the number of high-field-seekers, N_{hfs}, has to be reduced compared to the number of low-field-seekers, N_{lfs}, and the polarization

$$p = \frac{N_{\mathrm{lfs}} - N_{\mathrm{hfs}}}{N_{\mathrm{lfs}} + N_{\mathrm{hfs}}} \tag{3.27}$$

of UCN that are filled into the trap has to be larger than 90 %.

3.3.1 Theoretical Background

Spin filter

UCN can be polarized during filling with a magnetic barrier. Neutrons in a strong magnetic field are subjected to a potential

$$V_{\pm} = \pm\mu_n \left|\mathbf{B}\right|, \tag{3.28}$$

where the sign depends on the direction of their magnetic moment

$$\mu_{\mathrm{n}} = 60.3\,\mathrm{neV\,T^{-1}} \tag{3.29}$$

with respect to the magnetic field, **B**. When high-field-seekers travel through a strong magnetic field of several Tesla they see a potential well, which they can easily traverse. Low-field-seekers see a potential barrier, which they cannot pass if their energy is too low.

With this method—using a superconducting magnet producing a field of several Tesla—Serebrov et al. [52] achieved a polarization of 100 %. However, a much more cost-effective method with ferromagnetic films can be used. When neutrons pass through a magnetically saturated ferromagnetic film with an internal saturation field, B_s, they are subjected to a potential

$$V_\pm = V \pm \mu_\mathrm{n} B_\mathrm{s} \tag{3.30}$$

with the Fermi potential, V, from equation (3.1).

For iron, the saturation field is 2.16 T [53], so $V_\pm = 210\,\mathrm{neV} \pm 130\,\mathrm{neV}$. Ideally, the Fermi potential and magnetic potential compensate each other—so V_- is close to 0 neV—to achieve highest transmission of high-field-seekers. This is the case for a special mixture of iron isotopes with a Fermi potential of 130 neV [54], or for $\mathrm{Fe}_{0.5}\mathrm{Co}_{0.5}$ alloys with a Fermi potential of 135 neV [40] and a saturation field of 2.4 T [53].

With iron films, Herdin et al. [55] and Lauer [56] demonstrated polarization efficiencies of 90 % or more in the energy window between V_- and V_+.

Spin flipper

Since only high-field-seekers can traverse the magnetized foil but PENeLOPE can only store low-field-seekers, the neutron spins have to be reversed with respect to the magnetic field before they are filled into PENeLOPE.

For thermal neutron beams, such a spin flip is usually achieved by inverting the magnetic field non-adiabatically within a short distance [57]. However, due to the low velocity of ultracold neutrons, their spins can follow much larger spatial field gradients and this method cannot be applied. Instead, a nuclear-magnetic-resonance device, a so-called adiabatic fast-passage (AFP) spin flipper, can be used.

An AFP flipper consists of a static, inhomogeneous magnetic field, $B_0\hat{\mathbf{z}}$, along the unit vector $\hat{\mathbf{z}}$ and a perpendicular field, $\mathbf{B}_1$, rotating around $\hat{\mathbf{z}}$ with frequency ω. Rabi et al. [58] showed that in a frame of reference centered on the neutron's rest frame and rotating around $\hat{\mathbf{z}}$ with frequency ω the precession of the neutron's spin, $\mathbf{I}$, is described by the Bloch equation

$$\frac{\mathrm{d}\mathbf{I}}{\mathrm{d}t} = \gamma_\mathrm{n} \mathbf{I} \times \mathbf{B}_\mathrm{eff}(t) \tag{3.31}$$

with an effective field

$$\mathbf{B}_\mathrm{eff}(t) = \left(B_0(t) - \frac{\omega}{\gamma_\mathrm{n}} \right) \hat{\mathbf{z}} + B_1(t)\hat{\mathbf{x}}'. \tag{3.32}$$

The gyro-magnetic ratio of the neutron, γ_n, is $1.832\,471\,72(43) \cdot 10^8\,\mathrm{s}^{-1}\,\mathrm{T}^{-1}$ [19], and $\hat{\mathbf{x}}'$ is the x-direction in the rotating reference frame.

If the rotating field is applied to the neutron while it travels through the resonance point where $B_0 - \omega/\gamma_\mathrm{n} = 0$, the effective field smoothly inverts its direction and—if the

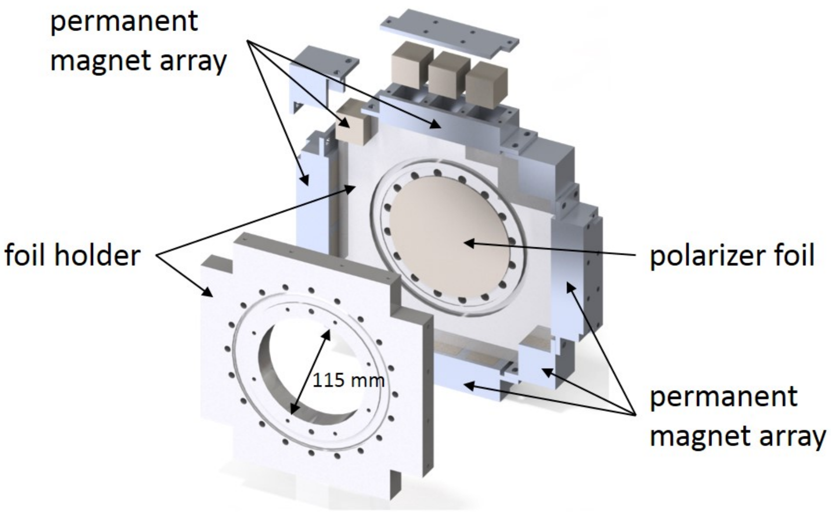

Figure 3.11: Explosion view of the polarization foil holder. The improved version with 16 permanent magnets is shown. The previous version used only a single magnet on each side instead of three in a row.

inversion is slow enough—the spin follows this changing field. The result a flipped spin with respect to the static field.

Two different field geometries are commonly used to realize such an AFP flipper for ultracold neutrons. The static field can be chosen parallel to the beam axis—often produced by a superconducting polarizer magnet—while the rotating field is transverse to the beam axis—produced by a so-called birdcage resonator [59]. Or the static field can be transverse to the beam tube—e.g. produced by Helmholtz coils—and the rotating field is oscillating along the beam axis—produced by a solenoid wound onto the beam tube [55, 60].

For polarizers with a magnetized film the latter field geometry is preferable.

3.3.2 Characterization of first prototype

Experimental setup

To use such a spin filter and flipper for PENeLOPE, I adapted them to the planned *Replika*-guide geometry of the UCN source. The Replika guides are rolled-up $\mathrm{Ni}_{0.93}\mathrm{V}_{0.07}$ sheets with an inner diameter of 115 mm and a length of 1 m contained in vacuum-tight cladding tubes with an inner diameter of 168.3 mm [61].

The polarizer consists of a 0.1 mm-thick aluminium-6061 foil coated with 150 nm to 300 nm of iron in a magnetron-sputtering facility with carefully chosen argon atmosphere [56]. The foil should also separate the guide vacuum with a pressure of about 10^{-4} mbar from the high vacuum in PENeLOPE with a pressure of less than 10^{-8} mbar. I designed a special foil holder, which clamps the foil between two polished stainless steel surfaces

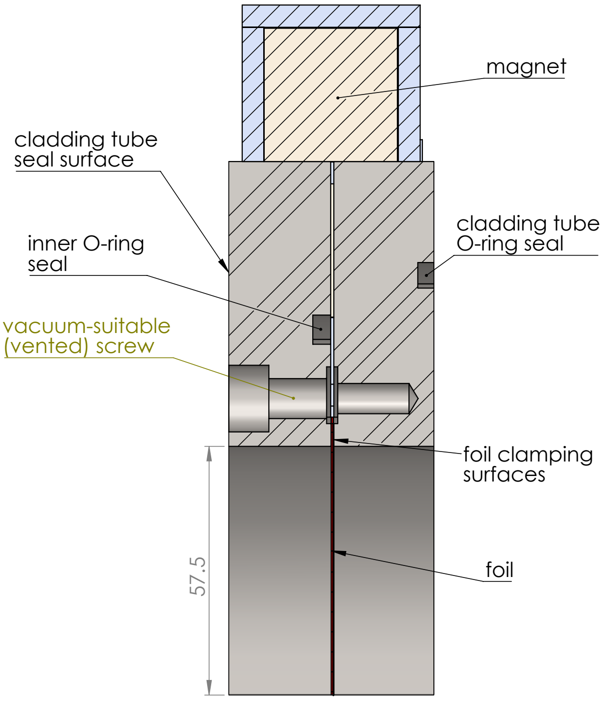

Figure 3.12: Cut through the upper half of the foil holder showing the vacuum seals. The foil thickness is exaggerated.

(figs. 3.11, 3.12).

Leakage through the thin metal seal provided by the clamped foil could contaminate PENeLOPE's experimental vacuum. We determined the leak rate through the foil by evacuating a Replika cladding tube on one side and filling it with low helium pressures, while the other side of the foil holder was pumped by a leak detector with a mass spectrometer sensitive to helium. Extrapolating the upper limit of the leak rate to the expected pressure difference of less than $10^{-3}\,\mathrm{mbar}$ gives a leak rate lower than $10^{-8}\,\mathrm{mbar\,l\,s^{-1}}$ (fig: 3.13). Hence, a pumping speed of $1\,\mathrm{l\,s^{-1}}$ is sufficient to sustain a vacuum pressure of less than $10^{-8}\,\mathrm{mbar}$. At least one high-vacuum pump—with a typical pumping speed of several hundred liters per second—will pump the guides volume below PENeLOPE to avoid contamination of the storage volume.

A transverse magnetic field of at least 10 mT was assumed to be sufficient to magnetically saturate the iron film [56]. To achieve this field, I mounted a so-called Halbach array [62] of eight NdFeB permanent magnets on the edges of the foil holder, which produces a transverse magnetic field with a minimum of 13 mT (figure 3.14). To avoid distortions of the polarizing field the foil holder was manufactured from non-magnetic stainless steel 1.4401.

Downstream of the polarizer its fringe field is smoothly brought down to a level of

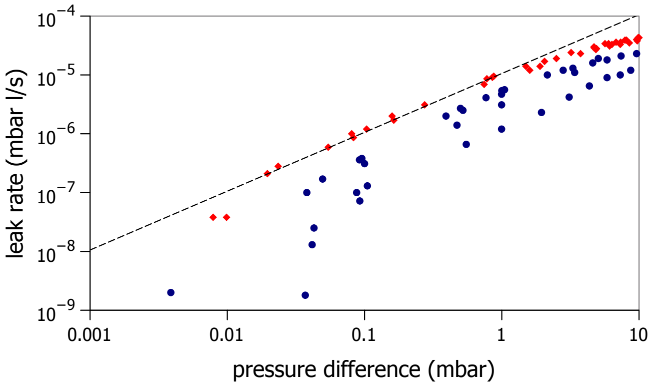

Figure 3.13: Measured leak rates through the foil. Red and blue indicate leak rates in opposite directions.

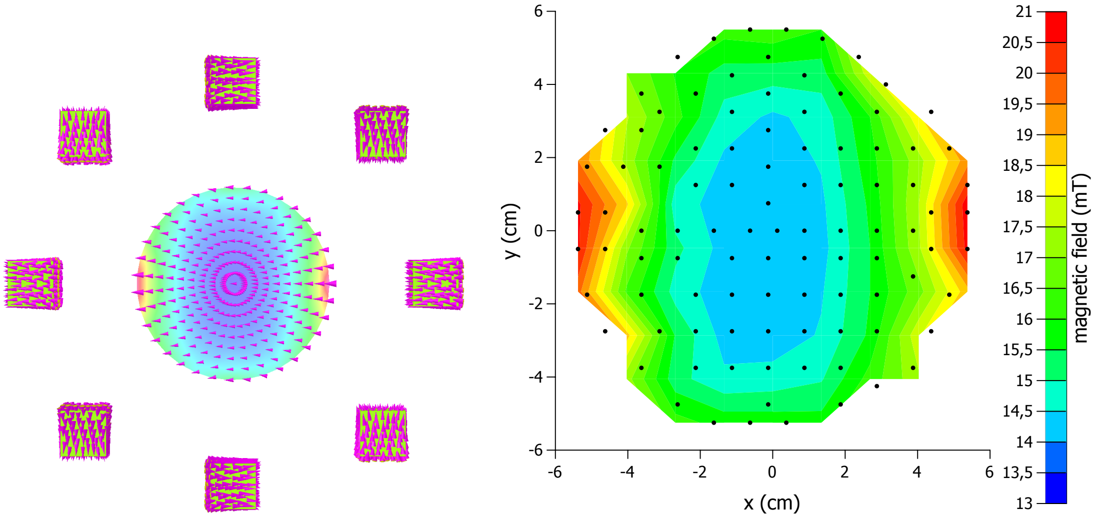

Figure 3.14: Color plot of simulated (left) and measured magnetic field (right) of the Halbach array of eight permanent magnets. The minimum field is 13.9 mT.

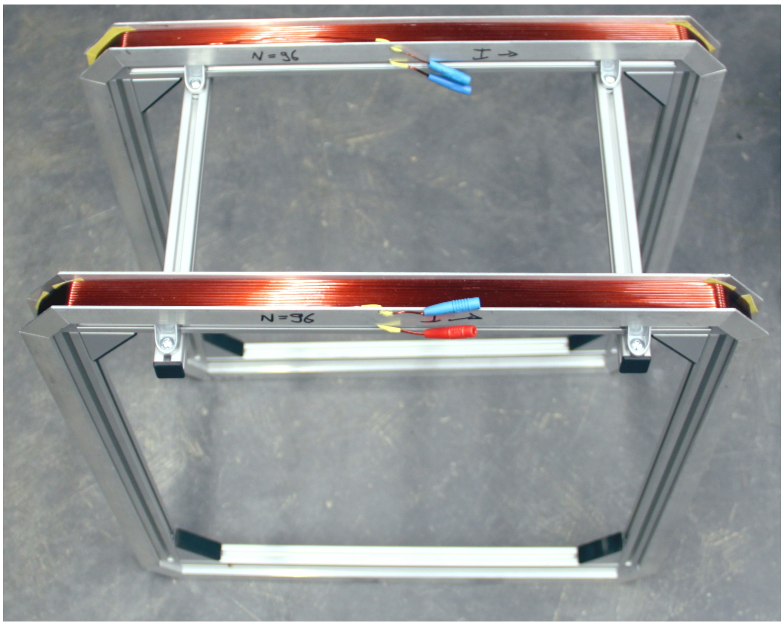

Figure 3.15: Pair of Helmholtz coils. Their side lengths are 45 cm.

about 1 mT (figure 3.16) by square Helmholtz coils with side lengths of 45 cm and 96 windings of enameled copper wire (figure 3.15).

The rotating field is produced by a solenoid with 28 windings of conductive, adhesive tape on Kapton foil, which was slid onto the guide (figure 3.17).

In a static field, B_0, of 1 mT the resonant frequency is

$$f = \frac{\gamma_\mathrm{n} B_0}{2\pi} = 29.165\,\mathrm{kHz}, \tag{3.33}$$

which can conveniently be driven by a sine-wave generator and a commercial *Reloop Dominance 702* audio amplifier [63]. The flipper's impedance was approximately tuned to the amplifier, which expects an impedance of 4 Ω to 8 Ω. The flipper coil has an inductance, L, of 50 µH, giving an impedance, $2\pi f L$, of 9.4 Ω at a frequency, f, of 30 kHz.

Schuldt [64] determined the current through the flipper with a clamp-on current probe capable of measuring AC currents up to frequencies of 100 kHz [65]. As expected, the current is maximal in a frequency range of 15 kHz to 30 kHz (figure 3.18). Even at frequencies up to 60 kHz the peak current reaches more than 2.5 A—corresponding to a peak magnetic field of 0.3 mT—which is sufficient to achieve good flipper performance, as demonstrated by Geltenbort et al. [60].

Electromagnetic fields at these frequencies experience a so-called skin effect. When penetrating a conducting material with resistivity ρ and magnetic permeability μ the field is damped exponentially within a characteristic skin depth

$$\delta = \sqrt{\frac{2\rho}{\omega\mu}}. \tag{3.34}$$

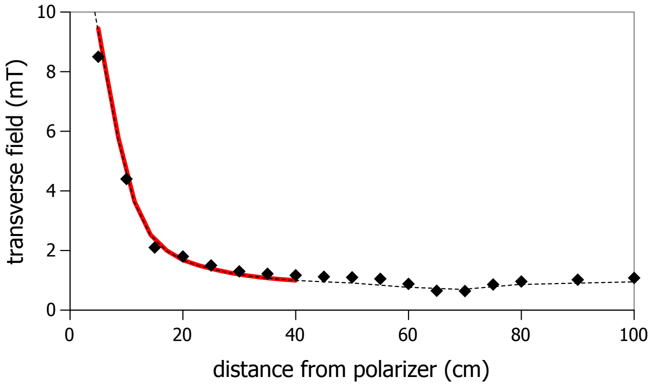

Figure 3.16: Simulation (dashed line) and real map (dots) of the field of polarizer and Helmholtz coils on the central guide axis. The red line indicates the field gradient in which a flipper could be effectively operated.

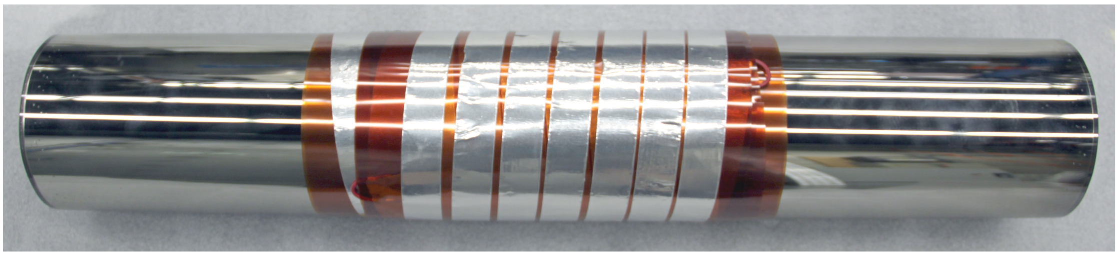

Figure 3.17: Spin-flipper coil on a $Ni_{0.85}Mo_{0.15}$-coated glass guide. The guide has a length of 700 mm and an outer diameter of 125 mm.

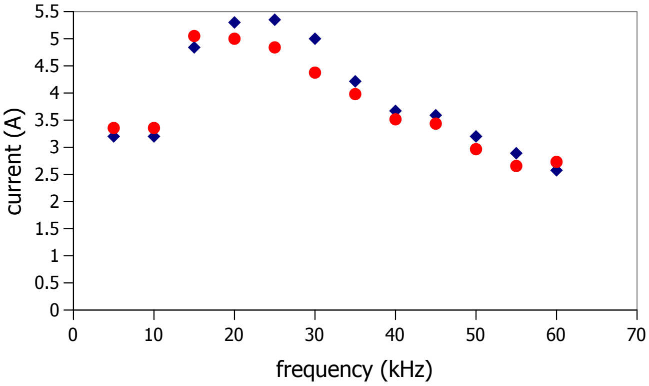

Figure 3.18: Current through flipper one (blue) and flipper two (red) at different frequencies. [64]

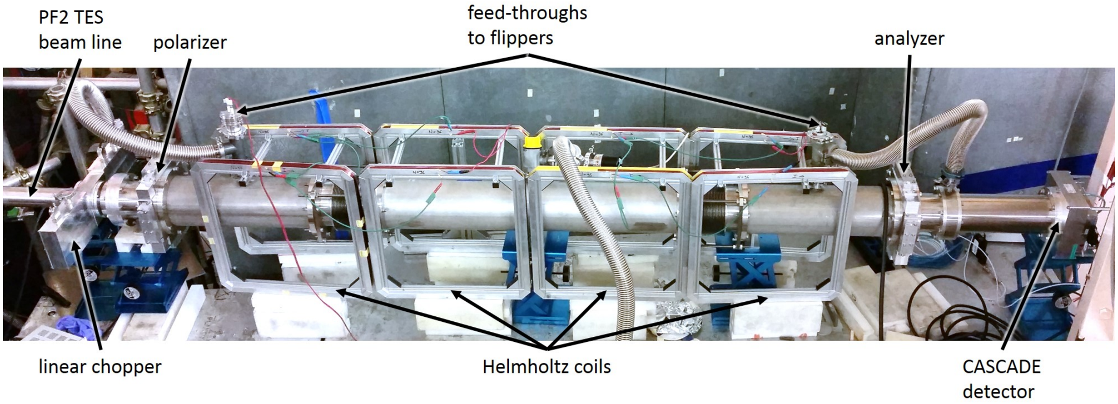

Figure 3.19: Experimental setup at the TES beam line of the UCN turbine PF2 at ILL. The improved setup with a chopper instead of a spectrum shaper is shown.

In nickel, the skin depth is smaller than 80 µm[3] and the field produced by the spin flipper can hardly penetrate the 500 µm-thick Nickel foil of the Replika guides. Instead, I replaced it with a glass guide with the same inner diameter, coated on the inside with 500 nm of non-magnetic $\mathrm{Ni}_{0.85}\mathrm{Mo}_{0.15}$ alloy by Lauer [56] (figure 3.17).

To determine the polarization efficiency and spin-flipper efficiency of this setup we built each component twice and arranged them in the order *polarizer–flipper one–flipper two–analyzer*. We measured the UCN transmission through this setup for four different cases: no flipper active, flipper one active, flipper two active, and both flippers active. The incoming UCN spectrum was cut off at low energies at 54 neV by the aluminium foils of the polarizers and at high energies at 245 neV by a nickel-coated spectrum shaper. The shaper consists of two short guide pieces that are radially offset in a cylindrical vacuum vessel. UCN can only traverse this shaper after several wall bounces and UCN with energies above the optical potential of nickel are lost with very high probability. A CASCADE-U detector [66] mounted directly behind the analyzer foil counted the UCN transmitted through the whole setup.

Analysis

The polarization of UCN can be described by a two-component vector, where the first component is the number of high-field-seekers and the second component is the number of low-field-seekers. Consequently, polarizer and spin flipper are characterized by 2 × 2 matrices. The rate of transmitted UCN, N_{ij}, for the different flipper combinations is

---

[3] $\rho_{\mathrm{Ni}} = 7 \cdot 10^{-8}\,\Omega\,\mathrm{m}$, $\mu_{\mathrm{Ni}} \geq 100\mu_0$ [53]

then given by the sequences

$$N_{00} = D \cdot P \cdot P \cdot I_0 \tag{3.35}$$
$$N_{10} = D \cdot P \cdot F_1 \cdot P \cdot I_0 \tag{3.36}$$
$$N_{01} = D \cdot P \cdot F_2 \cdot P \cdot I_0 \tag{3.37}$$
$$N_{11} = D \cdot P \cdot F_1 \cdot F_2 \cdot P \cdot I_0 \tag{3.38}$$

where

$$I_0 = \begin{pmatrix} i_0 \\ i_0 \end{pmatrix} \tag{3.39}$$

is the initial unpolarized beam;

$$P = \begin{pmatrix} t_{\mathrm{hfs}} & d_{\mathrm{lfs}} \\ d_{\mathrm{hfs}} & t_{\mathrm{lfs}} \end{pmatrix} \tag{3.40}$$

is the polarizer matrix[4] with transmission probabilities for high- and low-field-seekers, t_{hfs} and t_{lfs}, and the respective depolarization probabilities, d_{hfs} and d_{lfs};

$$F_i = \begin{pmatrix} 1 - f_i & f_i \\ f_i & 1 - f_i \end{pmatrix} \tag{3.41}$$

are the flipper matrices with spin-flipper efficiencies f_i; and

$$D = \begin{pmatrix} 1 & 1 \end{pmatrix} \tag{3.42}$$

is the detector efficiency for each spin state.

Solving equations (3.35)–(3.38) for the spin-flipper efficiencies, f_i, yields

$$f_1 = \frac{1}{2}\left(1 + \frac{N_{11} - N_{10}}{N_{00} - N_{01}}\right) \tag{3.43}$$
$$f_2 = \frac{1}{2}\left(1 + \frac{N_{11} - N_{01}}{N_{00} - N_{10}}\right). \tag{3.44}$$

Similarly to equation (3.27), the polarization efficiency of one polarizer foil is given by the difference of the numbers of high- and low-field-seekers in the beam after traversing the polarizer:

$$p = \frac{\begin{pmatrix} 1 & -1 \end{pmatrix} \cdot P \cdot I_0}{\begin{pmatrix} 1 & 1 \end{pmatrix} \cdot P \cdot I_0} = \frac{t_{\mathrm{hfs}} + d_{\mathrm{lfs}} - t_{\mathrm{lfs}} - d_{\mathrm{hfs}}}{t_{\mathrm{hfs}} + d_{\mathrm{lfs}} + t_{\mathrm{lfs}} + d_{\mathrm{hfs}}}. \tag{3.45}$$

To be able to calculate this quantity from equations (3.35)–(3.38), one has to make several assumptions. Depending on these, one arrives at different values, p_i, for the polarization.

One can assume a perfect polarizer, which only transmits high-field-seekers, which are partly depolarized when leaving the magnetized film—i.e. $t_{\mathrm{lfs}} = 0$ and $d_{\mathrm{lfs}} = 0$. If one

---

[4] The polarizer matrix is assumed to be the same for polarizer and analyzer.

also assumes that $f_1 = 1$ or $f_2 = 1$—which can be verified with equations (3.43) and (3.44)—the polarization is given by

$$p_1 = \frac{N_{00} - N_{10}}{N_{00} + N_{10}} \text{ or} \tag{3.46}$$

$$p_2 = \frac{N_{00} - N_{01}}{N_{00} + N_{01}}, \tag{3.47}$$

or, if one assumes that $f_1 = f_2$, the polarization is given by

$$p_3 = \frac{(N_{00} - N_{10})^2}{N_{00}N_{11} - N_{10}^2} \text{ and} \tag{3.48}$$

$$p_4 = \frac{(N_{00} - N_{01})^2}{N_{00}N_{11} - N_{01}^2}. \tag{3.49}$$

AFP spin flippers can achieve efficiencies of more than 99 %, as demonstrated by Herdin et al. [55] and Geltenbort et al. [60], fulfilling both assumptions very well.

However, if one assumes a symmetric polarizer matrix—i.e. $d_{\text{lfs}} = d_{\text{hfs}}$—the polarization is given by

$$p_i' = \sqrt{p_i}. \tag{3.50}$$

This assumption has commonly been used for similar transmission experiments [54, 56, 60] but potentially yields overly optimistic polarization values for the same measured rates [55, 67].

Results

We did first measurements with the previously described setup in May 2013 at the *TES* beam line of the UCN source *PF2* at Institute Laue-Langevin (ILL). We achieved UCN transmission rates of

$$N_{00} = \frac{C_{00}}{TP} \approx 1.3\,(\text{MWs})^{-1} \tag{3.51}$$

with a number of UCN, C_{00}, counted during a measurement time T. The reactor power, P, was recorded every minute and had a narrow gaussian distribution during seven days of beam time (figure 3.20). For the analysis, I assumed that it was constant at 53.40 MW with an uncertainty of 0.13 MW. Background measurements with a vacuum shutter closing the beam line showed a very small background rate of $(0.0020 \pm 0.0004)\,(\text{MWs})^{-1}$.

To find the optimal operating point for spin flipper and Helmholtz coils, I scanned the flipper frequency and Helmholtz-coil current in different combinations, which reduced the UCN count rates with one flipper active, N_{10} and N_{01}, to about $0.4\,(\text{MWs})^{-1}$ when the flipper reached its optimal efficiency (figure 3.21, 3.22).

I achieved the best results either with flipper frequencies of 30 kHz at a coil current of 2.5 A, or with flipper frequencies of 21 kHz at a coil current of 1.6 A. The measured efficiencies given by equations (3.43)–(3.50) are shown in table 3.3.

I used two sets of iron foils produced during the same coating process, which yielded the same polarization. Unfortunately, the polarization efficiency of 60 % was much smaller

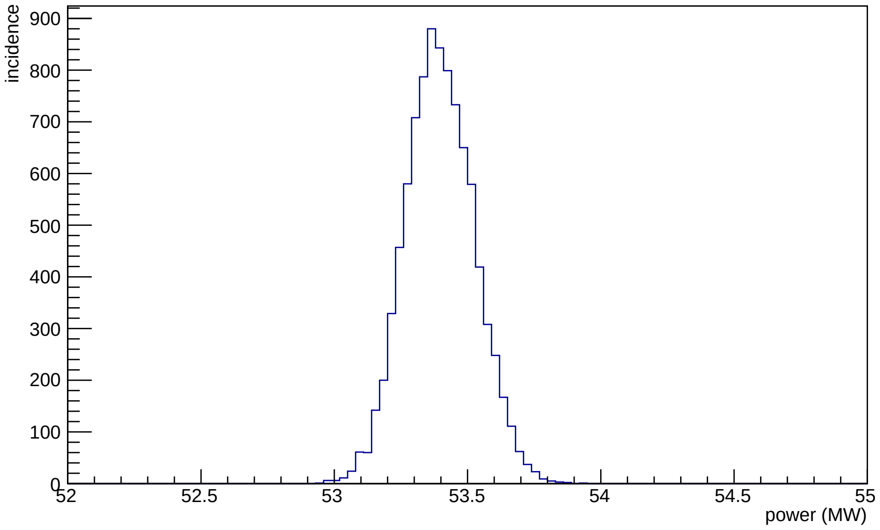

Figure 3.20: Fluctuation of ILL's reactor power between 17th and 24th of May 2013.

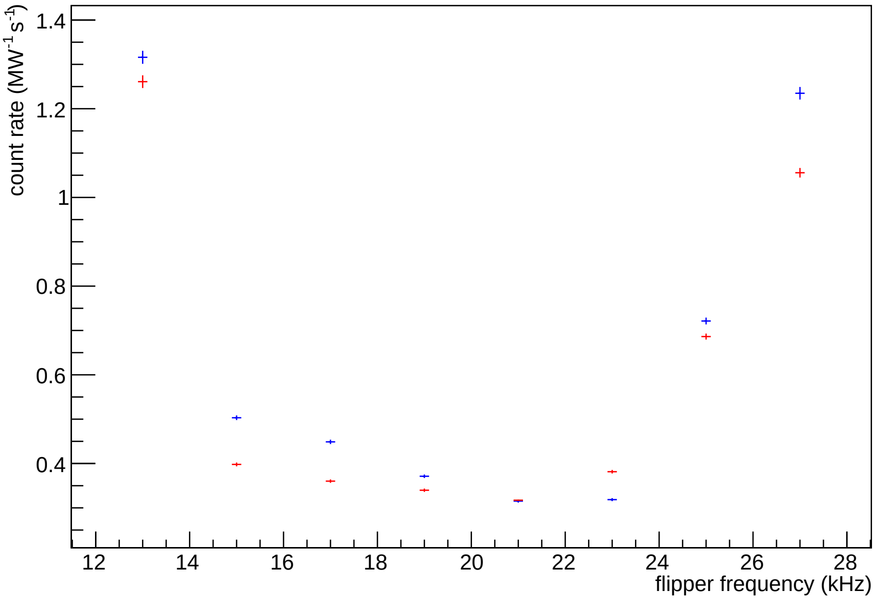

Figure 3.21: UCN count rates during a sweep of the frequencies of flipper one (blue) and flipper 2 (red) with a Helmholtz-coil current of 1.6 A. Best efficiency is achieved at 21 kHz, corresponding to a resonant, static field of 0.72 mT.

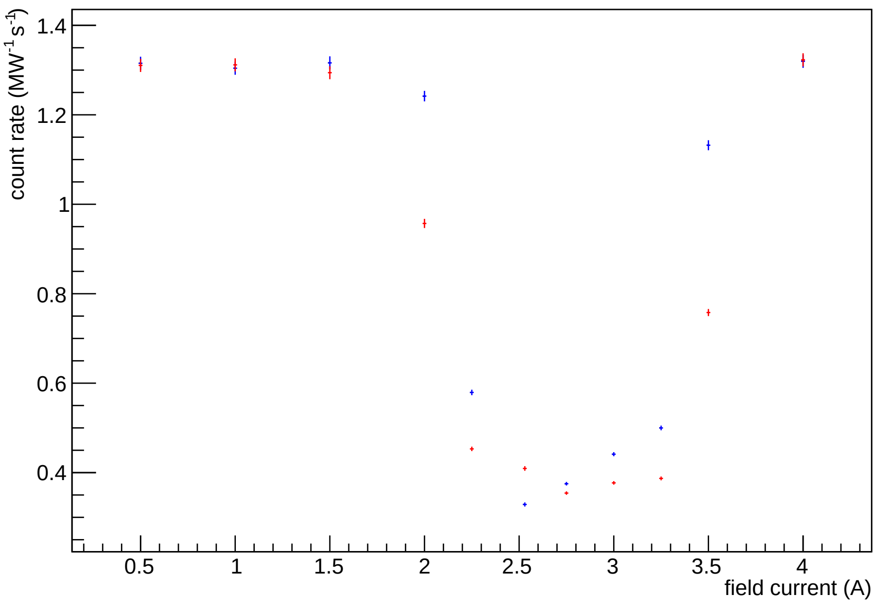

Figure 3.22: UCN count rates during a sweep of the Helmholtz-coil current with flipper one (blue) or flipper 2 (red) set to 30 kHz.

Table 3.3: Flipper and polarization efficiencies measured during the first run with different flipper frequencies and Helmholtz-coil currents.

Foil set	1	1	2	2
Frequency (kHz)	30	21	21	30
Current (A)	2.5	1.6	1.6	2.5
f_1 (%)	99.7 ± 2.0	99.8 ± 1.7	101.7 ± 1.9	100.2 ± 1.6
f_2 (%)	100.4 ± 2.0	99.6 ± 1.8	99.3 ± 1.8	98.2 ± 1.6
p_1 (%)	59.7 ± 0.9	61.3 ± 0.9	61.6 ± 0.9	62.2 ± 0.8
p_2 (%)	60.4 ± 1.0	61.1 ± 0.9	59.3 ± 0.9	60.1 ± 0.8
p_3 (%)	59.7 ± 2.0	61.6 ± 1.9	61.1 ± 1.9	63.0 ± 1.7
p_4 (%)	60.4 ± 2.1	61.4 ± 1.9	58.8 ± 1.8	60.9 ± 1.7
p'_1 (%)	77.3 ± 0.6	78.3 ± 0.6	78.5 ± 0.6	78.9 ± 0.5
p'_2 (%)	77.7 ± 0.6	78.2 ± 0.6	77.0 ± 0.6	77.6 ± 0.5
p'_3 (%)	77.2 ± 1.3	78.5 ± 1.2	78.2 ± 1.2	79.4 ± 1.1
p'_4 (%)	77.7 ± 1.3	78.3 ± 1.2	76.7 ± 1.2	78.1 ± 1.1

than the aspired 90 % while the flippers performed very well with efficiencies of more than 99 %. This made a second run with an improved setup necessary.

3.3.3 Optimization and second measurement

Since the polarization efficiency in the first run was lower than expected we performed a second measurement with an improved setup. Three possible effects were considered to have lowered the polarization:

- the polarization field might have been to small, so that it did not completely saturate the iron film;
- UCN with energies high enough that they could traverse even the fully magnetized polarizer might have been transmitted through the spectrum shaper;
- zero-field regions in the static field produced by the Helmholtz coils might have led to depolarization; and
- multiple reflections of low-field-seekers between polarizer and spectrum shaper might increase the probability that low-field-seekers traverse the polarizer.

Experimental setup

We reused the basic *polarizer–flipper–flipper–analyzer* geometry as previously described. To address the possible shortcomings I increased the polarizer field by adding another eight permanent magnets to the foil holder (figure 3.11), effectively doubling the minimum field to 27 mT (figure 3.23). We prepared a new pair of polarizer foils with 300 nm-thick iron films. And I replaced the UCN-spectrum shaper with a linear chopper to do a time-of-flight measurement.

A time-of-flight measurement allows a velocity-dependent measurement and reduces the effects of higher-energy UCN and mutliple reflections. The chopper consists of two titanium gratings housed in a vacuum chamber. Two linear motors can rapidly move the two gratings against each other; if the opening in the gratings overlap about half of the incominng UCN can pass, if the openings are offset UCN are absorbed in the titanium gratings. The chopper control electronics send a trigger pulse to the CASCADE detector which starts a measurement. With a slight delay, t_0, the chopper opens and lets pass UCN for a short time, t_1, until it closes again. After a certain measurement time the next trigger pulse is sent, the CASCADE detector returns the previously recorded time distribution of UCN entering the detector, and the whole cycle can start again.

I determined the chopper opening function by placing a light-sensitive diode on one side of the chopper and a flashlight on the other side of the chopper and recorded the control pulses and diode response with an oscilloscope (figure 3.24). I determined a delay of 17 ms. As opening time I chose 19 ms or—to increase count rates for shorter measurements—39 ms.

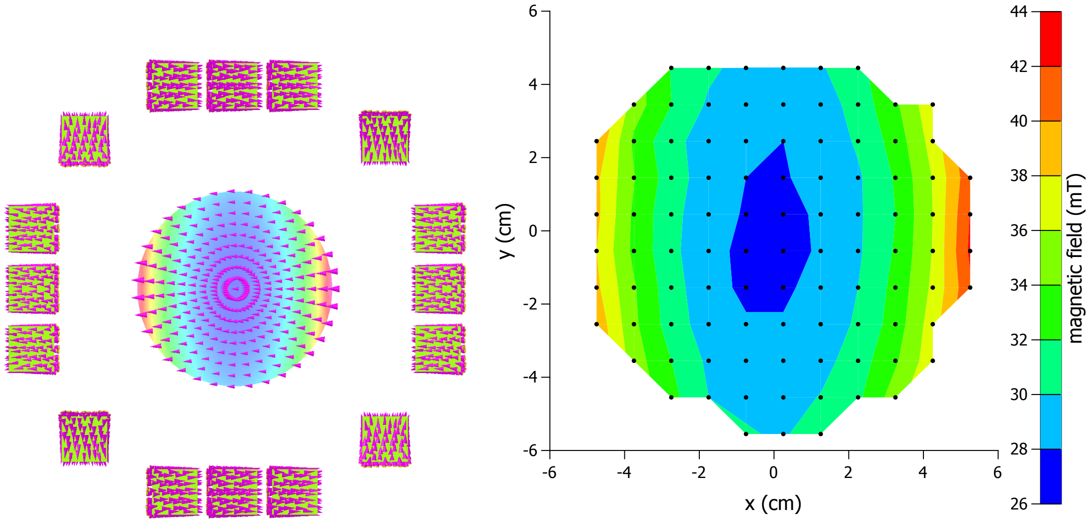

Figure 3.23: Color plot of simulated (left) and measured magnetic field (right) of the Halbach array of 16 permanent magnets [64]. The minimum field is 27.4 mT.

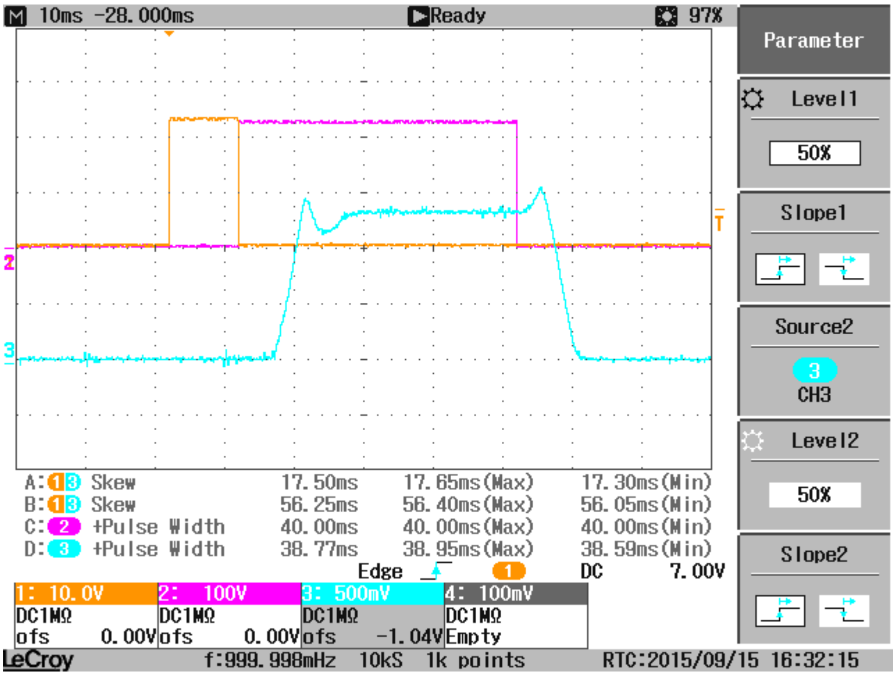

```
A:1 3 Skew          17.50ms   17.65ms(Max)   17.30ms(Min)
B:1 3 Skew          56.25ms   56.40ms(Max)   56.05ms(Min)
C:2 +Pulse Width    40.00ms   40.00ms(Max)   40.00ms(Min)
D:3 +Pulse Width    38.77ms   38.95ms(Max)   38.59ms(Min)
                           Edge    1    DC        7.00V
1: 10.0V     2:  100V     3: 500mV     4: 100mV
DC1MΩ        DC1MΩ        DC1MΩ        DC1MΩ
ofs    0.00V ofs    0.00V ofs   -1.04V Empty
         f:999.998mHz   10kS   1k points      RTC:2015/09/15 16:32:15
```

Figure 3.24: Trigger pulse (yellow), chopper control pulse (purple), and chopper opening function (light blue) recorded with an oscilloscope. A chopper opening time of 40 ms was chosen; the real opening time was determined to be 39 ms with a delay of 17 ms after the beginning of the 10 ms-long trigger pulse.

To determine the proper measurement time one needs to estimate the minimum neutron velocity of interest. The energy required to traverse the aluminium foils of polarizers and detector is 54 neV, corresponding to a velocity of $3.2\,\mathrm{m\,s^{-1}}$. Since the whole setup—from chopper window to detector foil—had a length, L, of 3205 mm I chose a measurement time of 1000 ms.

Analysis

Again, a measurement of polarization and flipper efficiencies consisted of four UCN-rate measurements with no flipper active, flipper one active, flipper two active, and both flippers active. Typical time-of-flight spectra recorded during the beam time in September 2015 are shown in figure 3.25. These spectra can be transformed into velocity spectra by calculating new boundaries, v_i, of velocity bins from the boundaries, t_i, of the time-of-flight bins:

$$v_i = \frac{L}{t_i - (t_0 + t_1/2)}. \tag{3.52}$$

This gives velocity spectra as shown in figure 3.26. The energy range of UCN in the guide that can be magnetically stored in PENeLOPE is about 100 neV to 215 neV, corresponding to a velocity range of $4.5\,\mathrm{m\,s^{-1}}$ to $6.5\,\mathrm{m\,s^{-1}}$.

I determined the polarization and flipper efficiencies with the Bayesian Analysis Toolkit [68] (see chapter 6). For the four polarization measurements, I described the likelihood, $\mathcal{L}$, of measuring UCN counts C_{ij} over a time T—separately in each time-of-flight bin—with a Poisson process. The expected rate of the Poisson process is the sum of the rate of transmitted UCN, N_{ij}, and the background rate, B_{ij}:

$$\mathcal{L}(C_{00}, C_{01}, C_{10}, C_{11} | P, F_1, F_2, I_0, B_{ij}) = \prod_{i,j=0,1} P_{\text{poisson}}\left[C_{ij} | (N_{ij} + B_{ij})T\right]. \tag{3.53}$$

I assumed that the prior-probability distributions of the four polarizer-matrix elements and the two flipper efficiencies are flat between zero and one. The prior-probability distribution of the background I set to a Poisson distribution with an average rate determined from the first few time-of-flight bins, where $t_i < t_0 + t_1/2$. Other assumptions about the parameters of polarizer or spin-flipper matrices, as in the analysis of the previous experiment, are not required.

Results

Such a Bayesian analysis of the spectra shown in figure 3.25 yields posterior-probability distributions for polarizer and flipper efficiencies as shown in figures 3.27 and 3.28.

If one assumes that only a small, constant fraction of low-field-seekers below the critical velocity, v_c, and all low-field-seekers above the critical velocity can traverse the polarizer one can describe the time-of-flight dependence of the polarization efficiency with a step function. A convolution with a gaussian resolution function with width σ results in the function

$$p(t) = \frac{p_0}{2} \mathrm{Erfc}\left(-\frac{t - L/v_\mathrm{c}}{\sqrt{2}\sigma}\right) \tag{3.54}$$

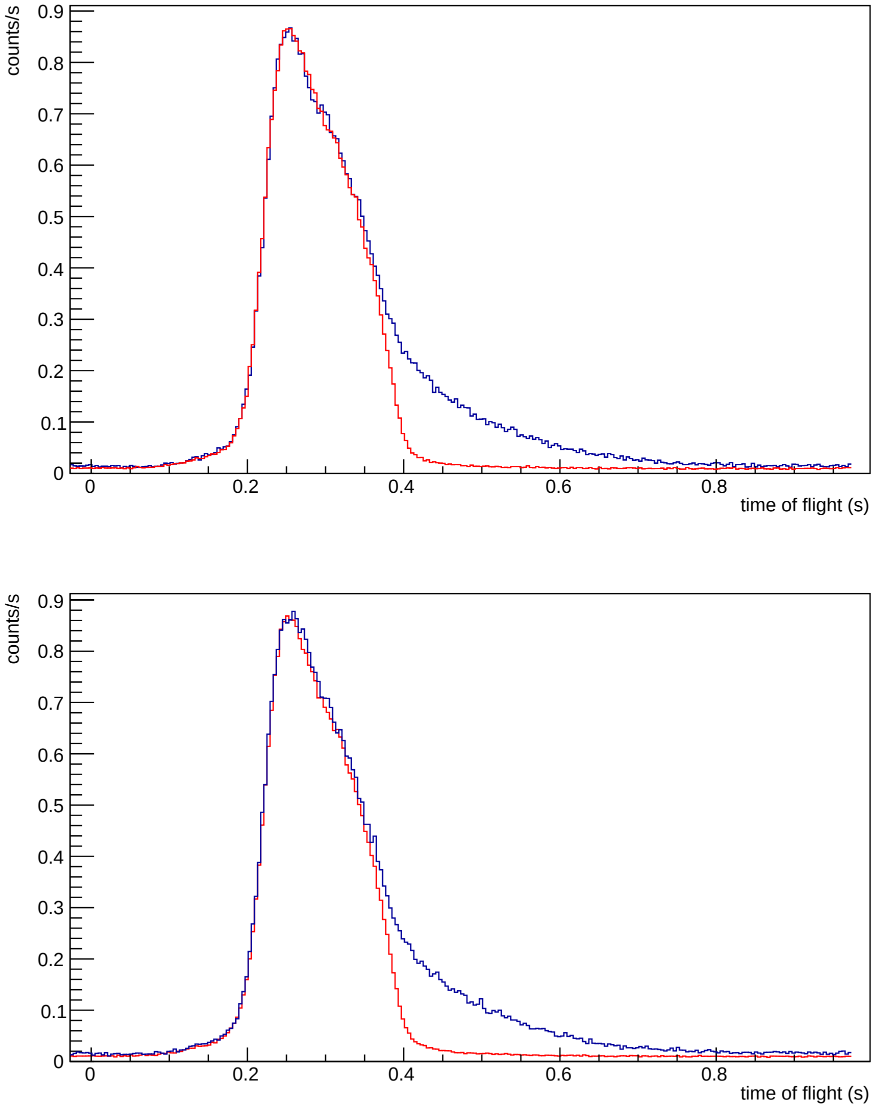

Figure 3.25: Time-of-flight spectra of UCN accumulated over 1.5 h with no flipper active (top, blue), 4 h with flipper one active (top, red), 6 h with flipper two active (bottom, red), and 1.5 h with both flippers active (bottom, blue). A pair of polarizer foils with 150 nm-thick iron films and flipper frequencies of 62 kHz and 60 kHz were used. The chopper delay, $t_0 + t_1/2$, of 27 ms is already subtracted.

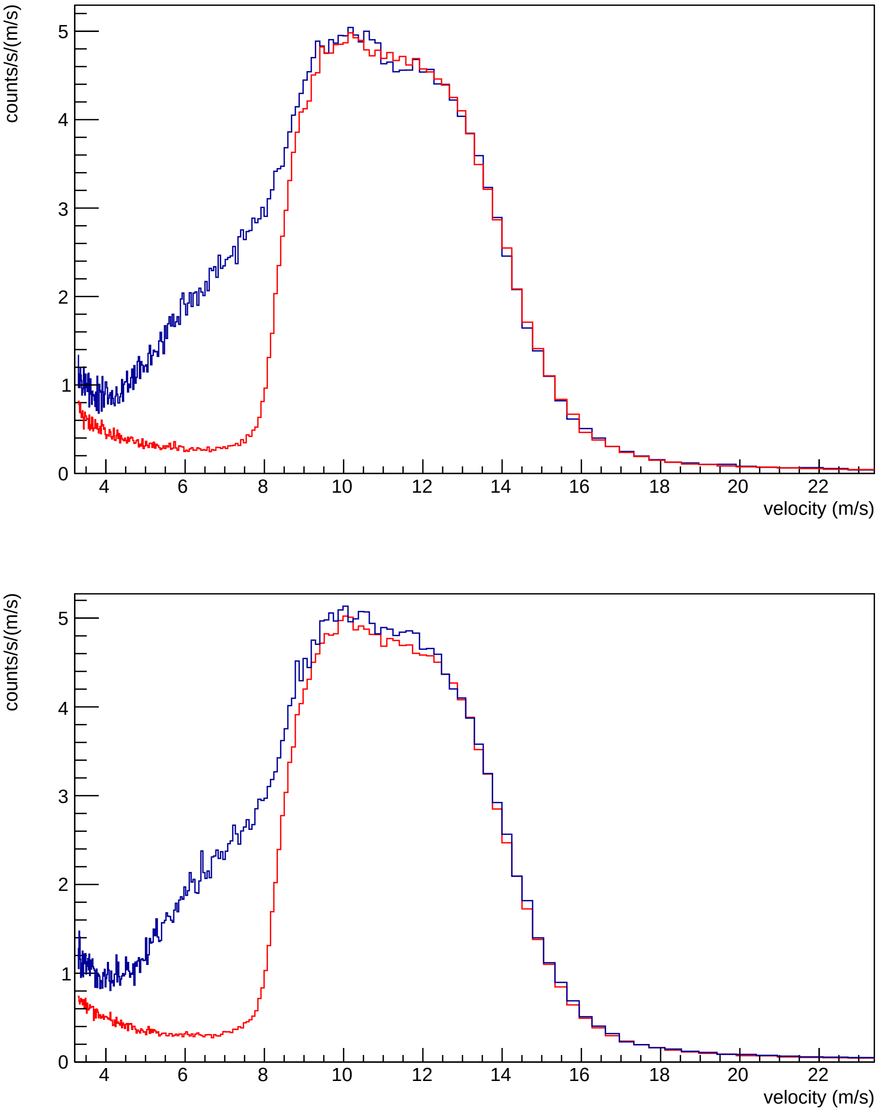

Figure 3.26: Velocity spectra calculated from figure 3.25 using equation (3.52), with no flipper active (top, blue), with flipper one active (top, red), flipper two active (bottom, red), and both flippers active (bottom, blue). The bin entries are divided by the bin width, transforming the flat background in the time-of-flight spectra into a background indirectly proportional to velocity.

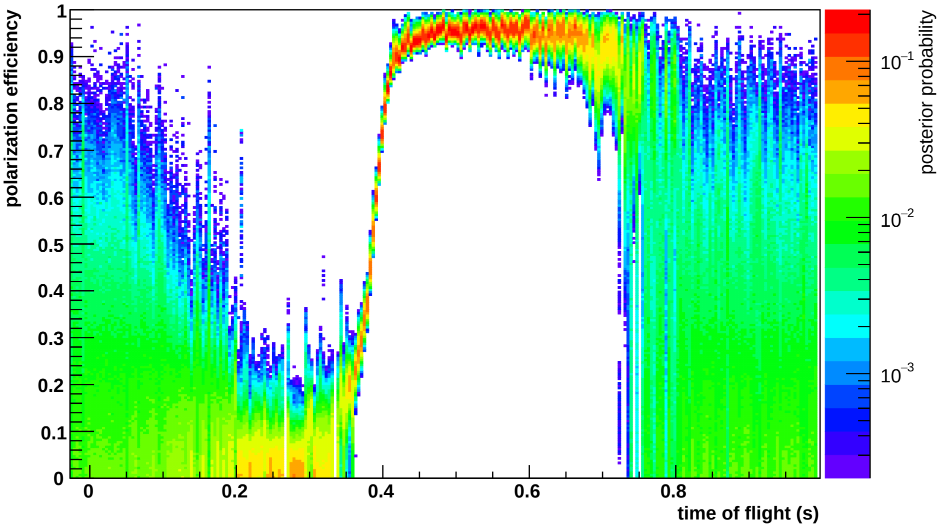

Figure 3.27: Full posterior-probability distributions of the polarizer efficiency in each time-of-flight bin, calculated from spectra in figure 3.25. In the missing bins BAT did not converge to a unique solution.

with the complementary error function Erfc.

To determine the critical velocity and the polarization efficiency below the critical velocity, p_0, I fit this function to the polarization efficiency in a time-of-flight range corresponding to a velocity range of $4.5\,\mathrm{m\,s^{-1}}$ to $12\,\mathrm{m\,s^{-1}}$. I performed a similar fit using a simple constant function $f(t) = f_i$ to determine the efficiencies of both flippers in a time-of-flight range corresponding to a velocity range of $4.5\,\mathrm{m\,s^{-1}}$ to $9\,\mathrm{m\,s^{-1}}$—where the polarization is large enough that the flipper efficiencies can be properly measured.

Again, I performed these fits with the Bayesian Analysis Toolkit. It determined the likelihood from the calculated posterior-probability distributions of the polarizer and flipper efficiencies in each time-of-flight bin (figures 3.27 and 3.28). The resulting velocity-dependent fit functions are shown in figures 3.29 and 3.30.

For the newly produced polarizer foils with an iron film with a thickness of 300 nm I determined a polarization efficiency of 90 % (table 3.4), much higher than in the previous measurements and sufficient for use in PENeLOPE. The flippers performed very well with efficiencies of 98.5 % to 99.5 %.

To run the flippers independently from the Helmholtz coils we moved the flippers into the larger fringe field of the polarizer and increased the frequencies accordingly. This change slightly reduced the efficiency of the flippers to 98 %.

We exchanged the new foils with the foils with an iron film with a thickness of 150 nm used in the previous experiment two years earlier. During this time the foils were simply stored in an anti-static bag with contact to the atmosphere. These older foils performed even better than the new ones, with efficiencies of 95 %, showing that there was no

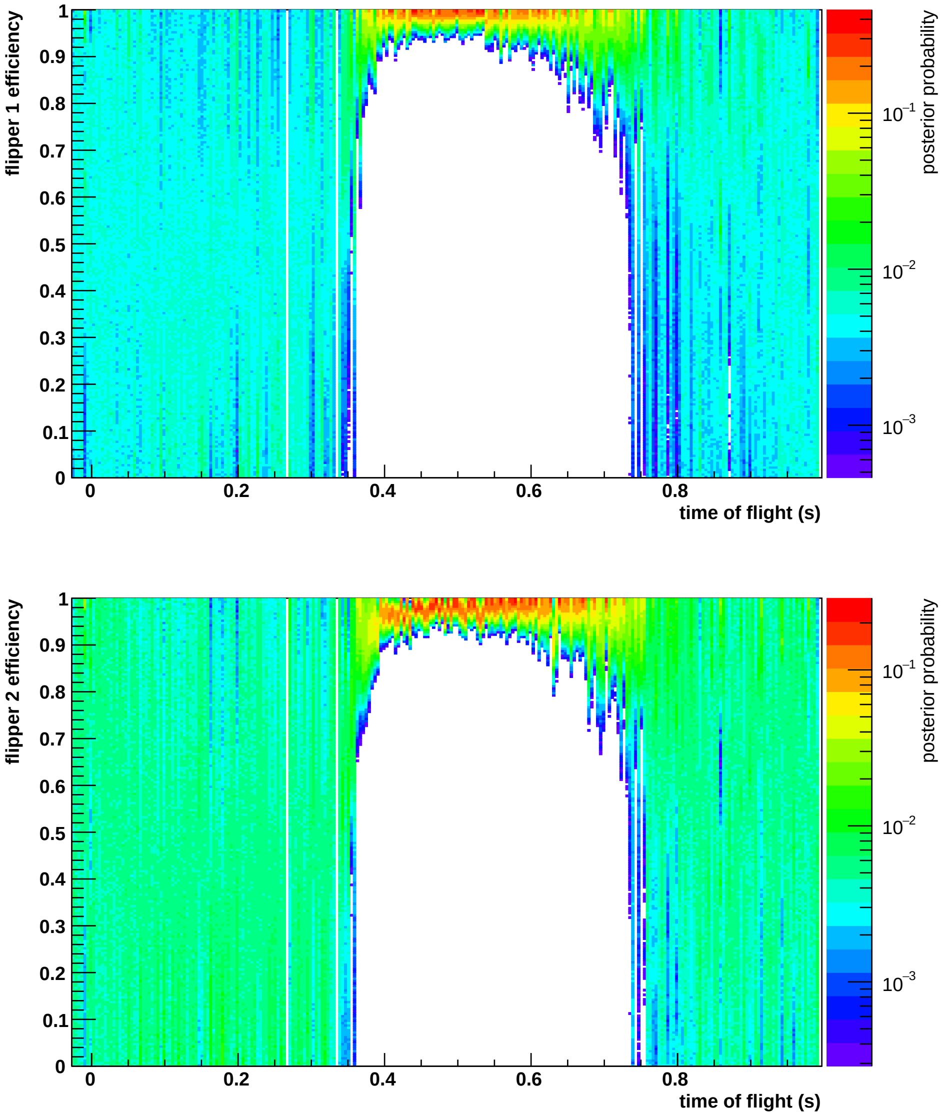

Figure 3.28: Full posterior-probability distributions of efficiencies of flipper one (top) and flipper two (bottom) in each time-of-flight bin, calculated from spectra in figure 3.25. In the missing bins BAT did not converge to a unique solution.

Table 3.4: Results of the Bayesian analysis of measurements with different polarizers, flipper parameters, and time-of-flight configurations. The values correspond to the maximum of the marginalized posterior-probability distributions, the uncertainties to 68 % credible intervals. Varied parameters are indicated in bold font.

Polarizer type	Fe	Fe	Fe	Fe	**FeCo**	Fe	Fe	Fe	Fe	Fe
Polarizer film (nm)	300	300	**150**	150	150	150	150	300	300	150
Polarizer field (mT)	27	27	27	27	27	**14**	**15**	27	27	27
Flipper 1 freq. (kHz)	35	**55**	62	62	62	45	50	35	35	62
Flipper 2 freq. (kHz)	35	**55**	60	60	60	45	50	35	35	60
Flipper amplitude (%)	100	100	100	100	100	100	100	**25**	**12**	100
Coil current (A)	4	4	4	4	4	4	4	4	4	**0**
Flight path (mm)	3205	3205	3205	**2205**	2205	2205	2205	3205	3205	2205
Chopper pulse (ms)	19	19	19	19	19	39	39	39	39	39
p_0 (%)	$89.2^{+0.7}_{-0.1}$	$90.1^{+0.6}_{-0.2}$	$95.0^{+0.3}_{-0.0}$	$94.6^{+0.7}_{-0.0}$	$55.5^{+1.1}_{-0.5}$	$93.8^{+0.6}_{-0.6}$	$90.5^{+1.1}_{-0.3}$	$90.5^{+0.0}_{-1.1}$	$74.0^{+1.2}_{-2.0}$	$96.0^{+0.0}_{-0.8}$
f_1 (%)	$98.5^{+0.4}_{-0.8}$	$98.0^{+0.5}_{-0.3}$	$99.5^{+0.4}_{-0.0}$	$98.0^{+0.8}_{-0.2}$	$92.0^{+3.3}_{-0.4}$	$98.0^{+1.1}_{-0.4}$	$91.0^{+0.7}_{-0.5}$	$98.0^{+0.9}_{-0.9}$	$45.5^{+2.2}_{-0.4}$	$99.5^{+0.4}_{-0.0}$
f_2 (%)	$99.5^{+0.4}_{-0.0}$	$97.5^{+0.8}_{-0.0}$	$97.5^{+0.8}_{-0.1}$	$98.5^{+1.0}_{-0.1}$	$99.0^{+0.1}_{-4.2}$	$99.5^{+0.3}_{-0.7}$	$97.0^{+1.8}_{-0.6}$	$99.5^{+0.3}_{-0.8}$	$73.5^{+3.2}_{-1.9}$	$99.5^{+0.4}_{-0.0}$
v_c ($\mathrm{m\,s^{-1}}$)	$8.36^{+0.03}_{-0.01}$	$8.37^{+0.03}_{-0.02}$	$8.38^{+0.01}_{-0.01}$	$8.43^{+0.02}_{-0.00}$	$7.85^{+0.07}_{-0.08}$	$8.42^{+0.04}_{-0.06}$	$8.33^{+0.04}_{-0.03}$	$8.40^{+0.05}_{-0.01}$	$8.42^{+0.08}_{-0.08}$	$8.34^{+0.03}_{-0.03}$
σ (ms)	$26.7^{+1.6}_{-1.5}$	$27.8^{+1.2}_{-1.2}$	$22.4^{+0.8}_{-1.2}$	$19.3^{+0.4}_{-1.1}$	37^{+4}_{-5}	$23.2^{+2.6}_{-0.8}$	$20.8^{+2.4}_{-1.5}$	$34.1^{+2.8}_{-1.6}$	29^{+8}_{-5}	$17.9^{+1.4}_{-1.2}$

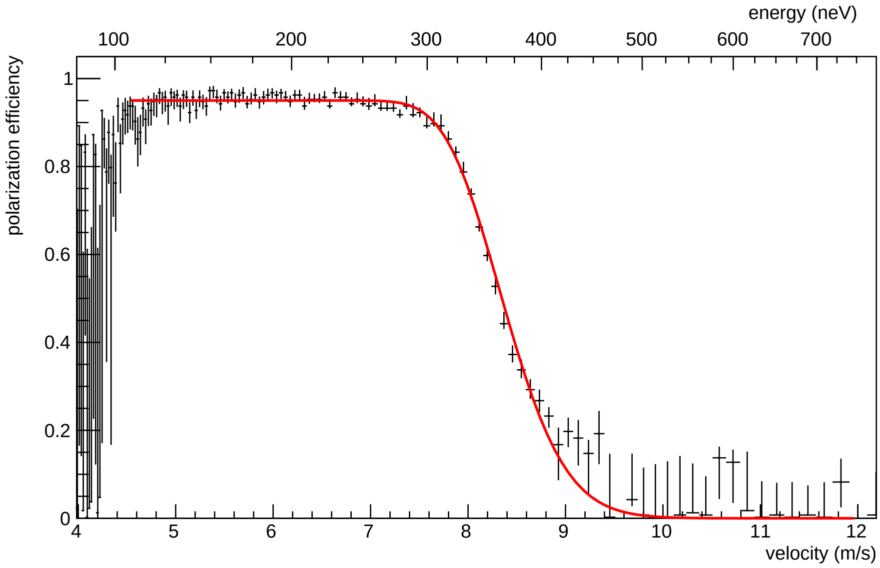

Figure 3.29: Velocity spectrum of polarizer efficiency and fit result obtained from figure 3.27. Error bars correspond to 68 % credible intervals.

degradation.

To replicate the results from the last experiment we removed the eight additional magnets on the polarizers. This required a reduction of flipper frequency and reduced their efficiencies, but the polarizer efficiency remained at 94 %. For a slightly different configuration we removed the six magnets on top and bottom of the Halbach array, which reduced the field to about 15 mT and the polarization to 90 %. This suggests that the threshold required for optimal polarization is barely reached with fewer magnets.

Additionally, we used another set of foils coated with 150 nm of $\mathrm{Fe_{0.5}Co_{0.5}}$. They reached a polarization efficiency of only 55 %.

Reducing the flipper amplitudes to 25 % of the nominal value did not reduce their efficiencies; only at an amplitude of 12 % they lost performance.

Shutting down the Helmholtz coils did not affect the polarization. This proves that UCN are extremely robust against non-adiabatic spin flips and Earth's magnetic field is sufficient to preserve their polarization.

The fit (3.54) also yields the velocity threshold, v_c, above which low-field-seekers can traverse the polarizer potential. This critical velocity was calculated to $8.4\,\mathrm{m\,s^{-1}}$, corresponding to an energy of 370 neV—slightly higher than the 340 neV expected from equation (3.30). The FeCo polarizer has a smaller critical velocity, corresponding to an energy of 320 neV, which is again larger than the expected 280 neV.

The full width of the resolution function, 2σ, is, in most cases, much larger than the chopper opening time. It instead seems to depend on the type of polarizer, suggesting that the broadening of the threshold is caused by transmission properties of the magnetized film. The thinner iron films show the smallest broadening of 40 ms, while it is increased

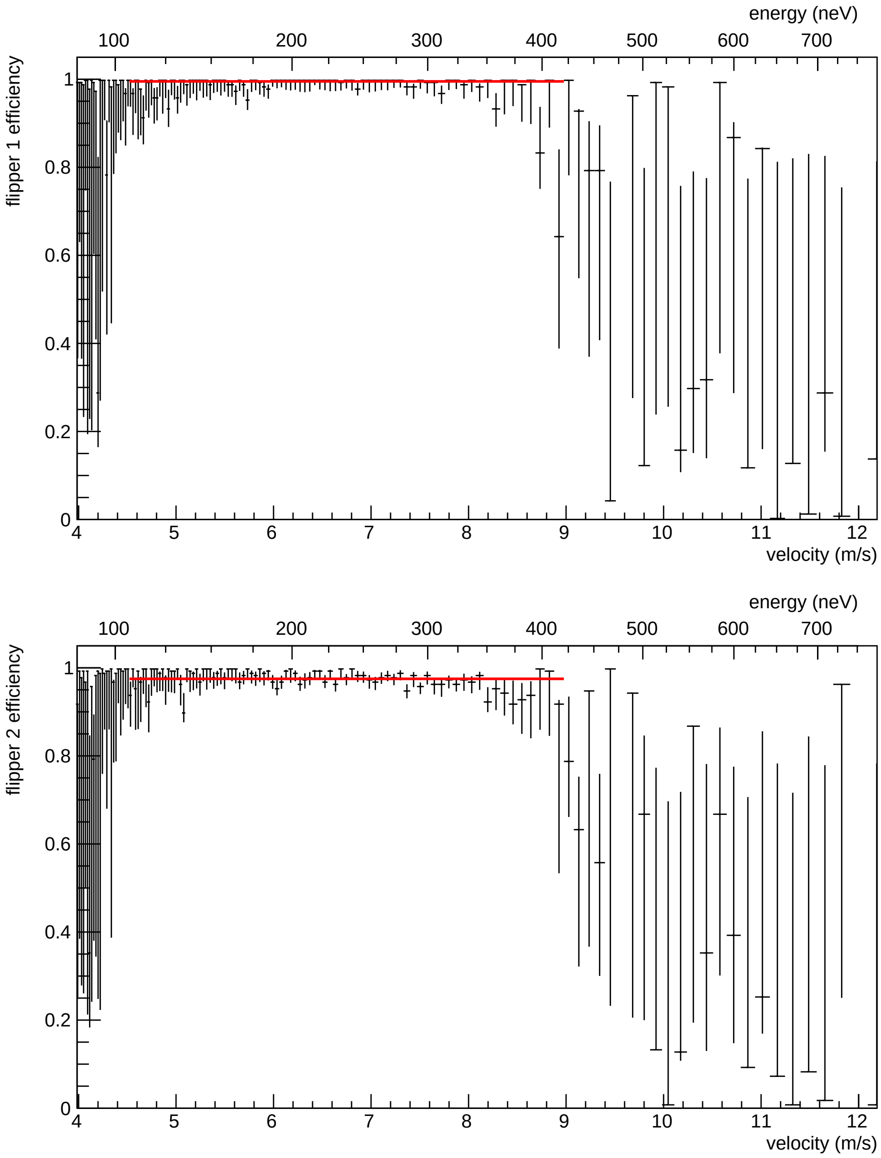

Figure 3.30: Velocity spectra of efficiencies of flipper one (top) and flipper two (bottom) obtained from figure 3.28, and the resulting fit functions. Error bars correspond to 68 % credible intervals.

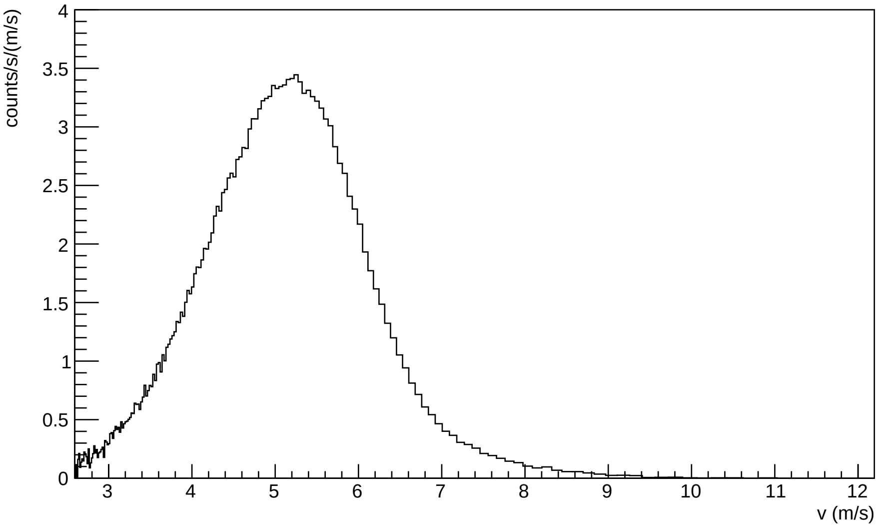

Figure 3.31: Velocity spectrum of UCN transmitted through the spectrum shaper, measured with a chopper pulse of 12 ms. The background has already been subtracted.

to 54 ms by the thicker films, and even to 74 ms by the FeCo films.

To investigate why the polarization was much lower in the first experiment in 2013 we also determined the velocity spectrum of UCN transmitted through the spectrum shaper. The results show that a small amount of UCN with velocities above $7.5\,\mathrm{m\,s^{-1}}$—where the polarizer efficiency starts to drop—is transmitted through the shaper (figure 3.31). This increases the number of low-field-seekers transmitted through the polarizer by 30 % to 50 %, corresponding to a drop in polarization of 2 % to 5 %. The reduced polarizer field of the smaller Halbach array might account for another drop of 5 %.

Multiple reflections between polarizer and spectrum shaper would result in an effective increase in initial beam intensity. If one assumes that high- and low-field-seekers have probabilities r_{hfs} and r_{lfs} of being reflected at both the polarizer and spectrum shaper and hitting the polarizer again, their initial intensities are increased by

$$I_0 = \begin{pmatrix} \frac{1}{1-r_{\mathrm{hfs}}} & 0 \\ 0 & \frac{1}{1-r_{\mathrm{lfs}}} \end{pmatrix} \begin{pmatrix} i_0 \\ i_0 \end{pmatrix}. \tag{3.55}$$

A large probability $r_{\mathrm{lfs}} = 0.5$ would lead to an effective doubling of incoming low-field-seekers. If one assumes that this proportionally increases the transmission of low-field-seekers through the polarizer and that r_{lfs} is negligibly small, this effect could reduce the measured polarization from 90 % to 80 %. This value is close to the optimistic result of the first measurement (table 3.3).

3.4 Potential systematic effects on the neutron-lifetime measurement

During filling and cleaning, several processes could cause fluctuations of the UCN density at the end of the cleaning stage. To minimize the effect of long-term drifts of UCN density on the neutron-lifetime measurement, the experimental cycles should alternate between short and long storage times. Else, a drift could mimic a dependency of the stored UCN density on the storage time, similar to beta decay.

In the worst case of a fluctuation correlated with the storage time, the systematic shift of the measured neutron lifetime is proportional to the fluctuation. A relative fluctuation of 10^{-4} would cause a shift of 0.1 s (see chapter 6.1.3).

3.4.1 Fluctuations in source intensity

Once filling is completed and the storage valve closed, the source valve also closes and the UCN switch moves into a middle position. This allows the UCN remaining in the guides between source and storage valve to enter the UCN detector. This emptying of the guides avoids leakage of UCN through the storage valve into the storage volume. Additionally, the number of detected neutrons can serve as an estimate for the achieved UCN density in the experiment and allows to compensate for fluctuating source intensity (chapter 6).

3.4.2 Varying thermal contraction of the magnet support

Depending on the liquid-helium level in the reservoir, the temperature profile of the magnet support between its connection to the radiation shield and the magnet itself will change. Between 77 K—the temperature of the radiation shield—and 4 K, stainless steel undergoes a contraction of about $0.2\,\mathrm{mm\,m^{-1}}$ [50]. A shift in the temperature profile of 0.5 m due to a falling liquid-helium level could cause a contraction of the magnet support by 0.1 mm, lifting the bottom of the storage volume, z_0, by the same height.

The number of UCN that can reach the storage volume during filling, N, depends on their total-energy spectrum, $N(H)$, in the energy window that can be stored in PENeLOPE from $m_\mathrm{n} g z_0$ to $m_\mathrm{n} g z_0 + 80\,\mathrm{neV}$, weighted by the chance that a UCN in this window reaches a height above z_0 (see section 4.3):

$$N \propto \int\limits_{m_\mathrm{n} g z_0}^{m_\mathrm{n} g z_0 + 80\,\mathrm{neV}} dH N(H) \int\limits_{z_0}^{H/m_\mathrm{n} g} dz \sqrt{H - m_\mathrm{n} g z}. \tag{3.56}$$

Assuming a total-energy spectrum proportional to $\sqrt{H - 106\,\mathrm{neV}}$ and a height $m_\mathrm{n} g z_0 = 120\,\mathrm{neV}$, a change of z_0 by 0.1 mm will cause a relative change in initial UCN density of $7 \cdot 10^{-5}$.

By keeping a constant fill level in the liquid-helium reservoir, this effect could be largely avoided. Constantly trickling liquid helium into the reservoir might be preferable to filling it once per day. This effect could also potentially be compensated by measuring the distance from the bottom of the magnet structure to the vacuum vessel, which can be assumed fixed with respect to the source.

3.4.3 Imprecise timing

The durations of the filling and cleaning stages should stay constant. Any variation would increase or decrease UCN density. The valve actuation and magnet startup times—which determine the start and end of these stages—should be precisely defined and monitored.

During filling, the number of UCN in the storage volume, N, follows an exponentially saturating curve

$$N(t) \propto 1 - \exp\left(-\frac{t}{\tau_\mathrm{f}}\right) \tag{3.57}$$

with a typical time constant, τ_f, of 70 s. If one assumes a filling time of three times this time constant, the relative change of UCN density at the end of the filling stage is

$$\frac{\partial N}{\partial t}(t = 3\tau_\mathrm{f}) = 7 \cdot 10^{-4}\,\mathrm{s}^{-1}. \tag{3.58}$$

To reduce the fluctuation of UCN density at the end of the filling stage below 10^{-4} the actuation times of source valve and storage valve should be accurate to 0.1 s or less.

During cleaning, the number of UCN drops exponentially

$$N(t) \propto \exp\left(-\frac{t}{\tau_\mathrm{s}}\right) \tag{3.59}$$

with a storage lifetime, τ_s, of about 300 s. If one assumes a cleaning time of 200 s, the relative change of UCN density at the end of the cleaning stage is

$$\frac{\partial N}{\partial t}(t = 200\,\mathrm{s}) = 2 \cdot 10^{-3}\,\mathrm{s}^{-1}. \tag{3.60}$$

To reduce the fluctuation of UCN density at the end of the filling stage below 10^{-4} the times of storage-valve actuation and magnet power-up should be accurate to 0.05 s or less.

3.4.4 Adsorption of rest gas

Contamination of trap walls with hydrogen is of particular importance in experiments trapping ultracold neutrons. Inelastic scattering of neutrons on hydrogen impurities was discovered to be the leading cause of larger-than-expected losses in early storage bottles [69, 70]. Several methods to mitigate this effect have been studied: removal of hydrogen with in-situ gas discharges [71] and regular renewal of wall coatings by sputtering metal films [72] or spraying liquid Fomblin oil [73] onto the trap walls.

PENeLOPE's storage bottle will be cooled to a temperature of 4.2 K. Kosvintsev et al. [74] showed that such cooling leads to major improvements in storage time. However, at these temperatures, rest gas in the storage volume—mostly hydrogen—is frozen onto the walls, leading to wall losses increasing over time. Kosvintsev et al. [74] prevented this by freezing heavy water onto the walls. In principle, this approach could also be used for PENeLOPE.

Measurements of hydrogen-adsorption isotherms in cryogenic vacuum systems show that the amount of hydrogen covering the cold surface, S, is only weakly depending on the rest-gas pressure, p, once it drops below the saturated vapor pressure of about 10^{-6} mbar [75]. Their relation can be approximated by a logarithmic dependence

$$S \approx 1.5 \cdot 10^{14}\,\mathrm{cm}^{-2} \cdot \ln\left(\frac{p}{3.0 \cdot 10^{-13}\,\mathrm{mbar}}\right). \tag{3.61}$$

The total hydrogen contamination of typical vacuum surfaces is in the order of $10^{16}\,\mathrm{cm}^{-2}$[41, chapter 5.3]. A fluctuation of 5 % around a vacuum pressure of 10^{-8} mbar will therefore change the total hydrogen concentration at the walls by 0.07 %. If one assumes that upscattering at hydrogen molecules is the dominating loss process at the walls, the storage time of about 300 s will also change by 0.07 %. This will lead to a relative change in UCN density at the end of the cleaning stage of $5 \cdot 10^{-4}$.

4 Stages III and V: Ramping the magnet

This chapter describes design and tests of PENeLOPE's superconducting magnet and the effect of a slowly changing trapping potential on the energy spectrum of stored UCN.

4.1 The superconducting magnet

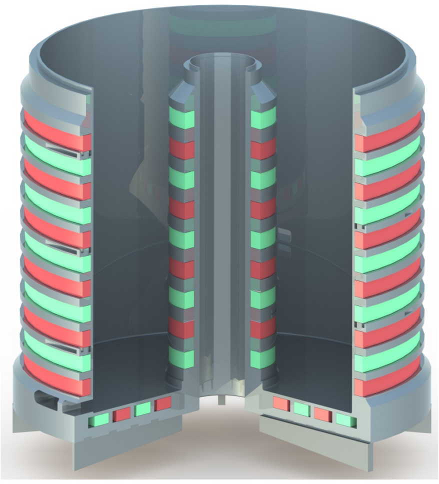

Figure 4.1: Sectional view of PENeLOPE's magnet. The inner diameter of the outer cylinder is 1.0 m.

PENeLOPE's superconducting magnet consists of 24 individual coils in series with a current density of $316\,\mathrm{A\,mm^{-2}}$. Each coil has between 1520 and 1940 windings of *Supercon VSF-SSCI* NbTi wire with a diameter of 0.9 mm, which carries a nominal current of 283.5 A. The wire is wound onto the support structure with a tension of 105 N [76]. The resulting hoop tension prevents the wire package from detaching from the support due to thermal contraction and magnetic forces. After winding, the wire package is impregnated with epoxy resin and the individual coils are welded together (figure 4.1). The magnet is encased in a liquid-helium bath cryostat and cooled to 4.2 K, the boiling point of liquid helium at a pressure of 1 bar.

NbTi becomes superconducting once its temperature falls below its critical temperature of about 9.2 K [77]. It becomes normal-conducting again if it is exposed to a current density larger than a critical current density or a magnetic field larger than a critical

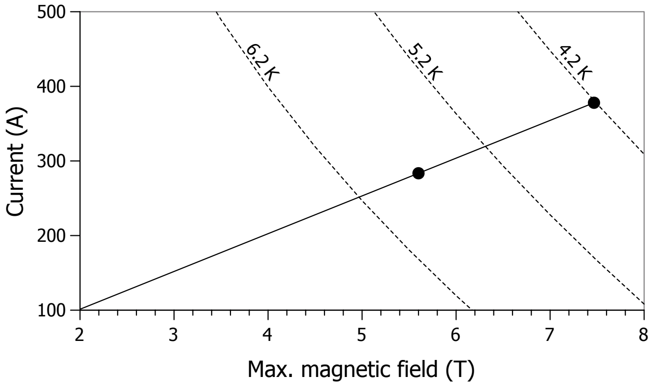

Figure 4.2: Critical current of the Supercon VSF-SSCI superconductor (dashed lines) at different temperatures [77–82]. The solid line represents the load line of PENeLOPE's magnet and the dots represent its nominal and critical current.

magnetic field. Critical temperature, critical current density, and critical magnetic field depend on each other and form a critical surface (figure 4.2). The wire data sheets [78–81] list critical currents and fields at a typical operating temperature of 4.2 K. Following Materne [82], I used a function describing the critical surface, given by Bottura [77], to calculate the critical current at other temperatures.

The magnetic field a superconducting magnet is subjected to is proportional to the current density in the magnet—the superconductor is operated along a linear load line (figure 4.2).

To reduce losses of ultracold neutrons, the current in the magnet is ramped with a rate of $3\,\mathrm{A\,s^{-1}}$ and reaches the nominal current in less than 100 s. This fast ramping and the large inductance of 32.5 H require a high-power four-quadrant power supply capable of a voltage of ±100 V at 283.5 A. Additionally, fast ramping leads to eddy currents, coupling losses, and hysteresis losses that dissipate heat into the wire package [83]. If this heat input increases the temperature of the wire above its critical temperature it becomes normal-conducting. The following resistive heating leads to a rapid chain reaction in which the whole coil becomes normal-conducting, a so-called quench.

4.2 Superconducting-coil tests and training

Due to the high current density, PENeLOPE's magnet is operated at 75 % of the critical load of the NbTi superconductor (figure 4.2). Even coil designs that take into account hoop tension, eddy current heating, coupling losses, and hysteresis losses may undergo quenches while being ramped to such high loads. However, after each quench, the current can be ramped a little higher than before until the nominal current is eventually reached. This training effect is caused by cracks in the epoxy resin that allow the superconducting wire to move slightly, which leads to friction heating and a quench [84]. If this movement settles the wire into a more favorable geometry the current can be increased a little

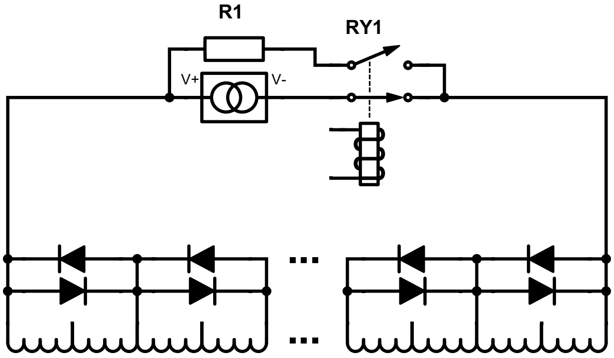

Figure 4.3: Electrical schematic of PENeLOPE's magnet. Each pair of coils is bridged by protection diodes. If a sudden voltage increase over any coil pair is detected the quench protection interlock RY1 inside the power supply is released and the magnet current is dumped into the water-cooled resistor R1.

further as a result.

A quenched coil still has to dissipate the energy stored in its magnetic field. According to Lenz's law a high voltage is induced to sustain the current flow through the coil. To limit the inductive voltage drop the coil can be bridged with quench protection diodes limiting the voltage to the diodes' breakthrough voltage. Additionally, they take over the bulk of the current still flowing through the other, still superconducting, coils to avoid excessive heating of the quenched coil.

During assessment of the mechanical loads on the support structure of the magnet Steinmann [85] noticed that a quench of a single coil could significantly increase, and even reverse, the loads. However, if pairs of coils with opposite current direction always quench together, the loads are greatly reduced. Hence, the protection diodes of PENeLOPE's magnet do not bridge coils individually, but in pairs (figure 4.3). The voltage at the connection of the coils of each pair is therefore not limited by diodes, can reach up to 6.6 kV [76], and has to be designed accordingly.

To evaluate performance and training behavior of parts of PENeLOPE's magnet a coil-test experiment *CoTEx*—a liquid-helium bath cryostat large enough to test all coils of PENeLOPE indivdually or in stacks (figure 4.4)—was built at the Maier-Leibnitz-Laboratorium [82, 86].

4.2.1 Prototype coil

To evaluate the general design of the individual coils, a prototype of the innermost bottom coil was manufactured by Babcock Noell GmbH (figure 4.5). This coil was chosen since its large ratio of outer radius to inner radius was considered most critical [87].

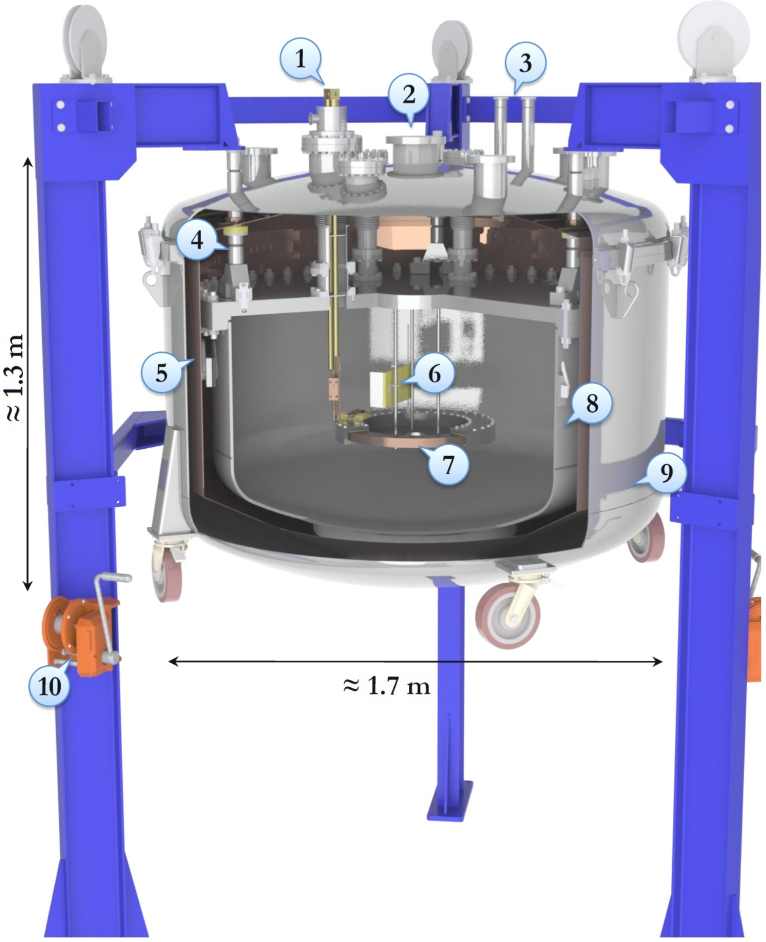

Figure 4.4: Rendering of the CoTEx cryostat with magnet-current feed-through (1), pumping port (2), liquid-nitrogen feed-throughs (3), helium tank suspension (4), radiation shield (5), array of quench-protection diodes (6), prototype coil (7), liquid-helium tank (8), vacuum vessel (9), and lifting crank (10). [86]

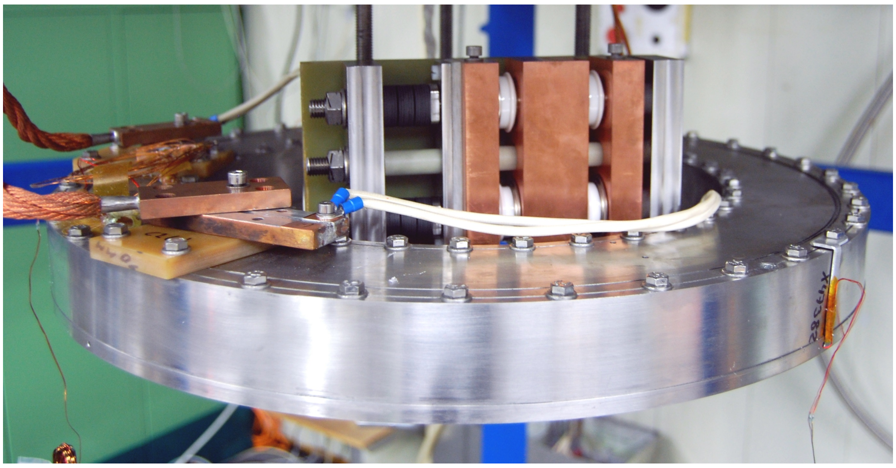

Figure 4.5: Prototype coil in its stainless steel housing with a diameter of 0.50 m. Also shown are the protections diodes with their cooling blocks (center) and the current terminals (left).

Training

The nominal current of this single coil was scaled from 283.5 A to 291.5 A to operate it at the same load as in the complete magnet assembly.

We carried out the training by slowly ramping up the current in the coil with a ramp rate of 0.5 $\mathrm{A\,s^{-1}}$ until it quenched. Voltage taps at the diode terminals and *Cernox* temperature sensors attached to the magnet allowed us to record the voltage drop over the magnet (figure 4.6) and its temperature (figure 4.7). A quench leads to large heating and liquid-helium boil-off and requires several minutes to settle back down. We then repeated this procedure until the nominal current could be reached without a quench (figure 4.8). Afterwards we checked if the nominal current can be reached with the nominal ramp rate of 3 $\mathrm{A\,s^{-1}}$ several times in quick succession and if the coil can carry the nominal current for at least one hour.

Training reproducibility

Materne [82] and Senft [86] already successfully trained the coil to 115 % of its nominal current (figure 4.8). We did additional tests of the prototype coil to check if the training is affected by temperature cycles, heat, or shocks and vibration.

The training was partially reversed during disassembly of the cryostat, several months of storage at room temperature, and re-installation in CoTEx: after the third cool-down the coil required five quenches to reach nominal current again. However, the coil could be trained to up to 350 A, 120 % of its nominal current, and ramped with up to 8.5 $\mathrm{A\,s^{-1}}$, almost three times the nominal rate.

Subsequently, the coil was warmed up to room temperature and cooled down again, after which it required only one quench to reach nominal current again.

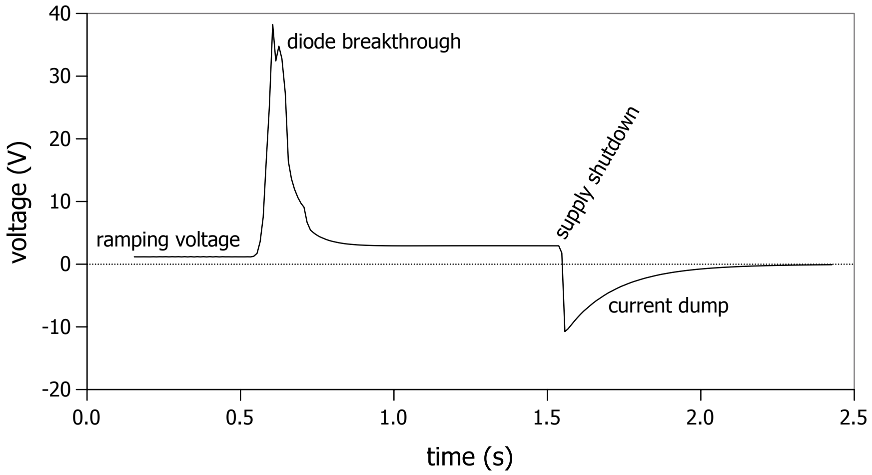

Figure 4.6: Voltage evolution during a typical quench of the prototype coil. The power supply suddenly increases the voltage to stabilize the current through the now resistive coil until the protection diodes break through. Less than one second later the quench detection shuts down the power supply and the energy remaining in the magnet is dissipated in the dump resistor.

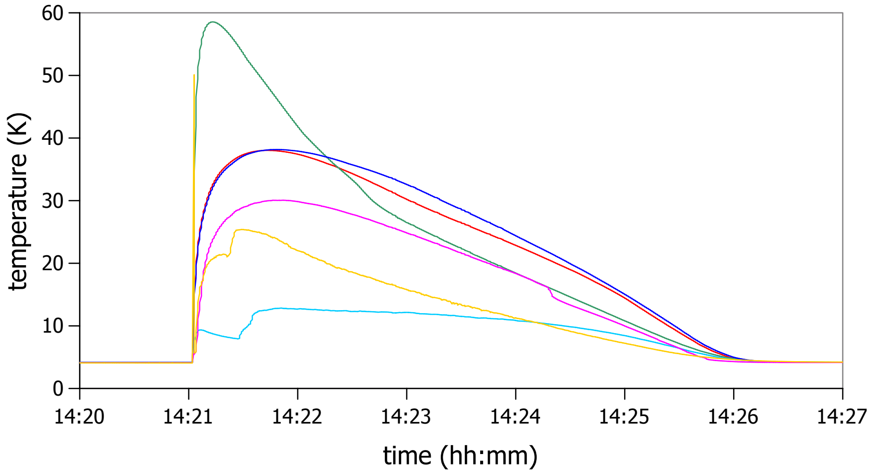

Figure 4.7: Temperature evolution during a typical quench measured by six Cernox sensors attached to the prototype coil. Most likely, the quench happened close to the sensor that shows the highest peak temperature.

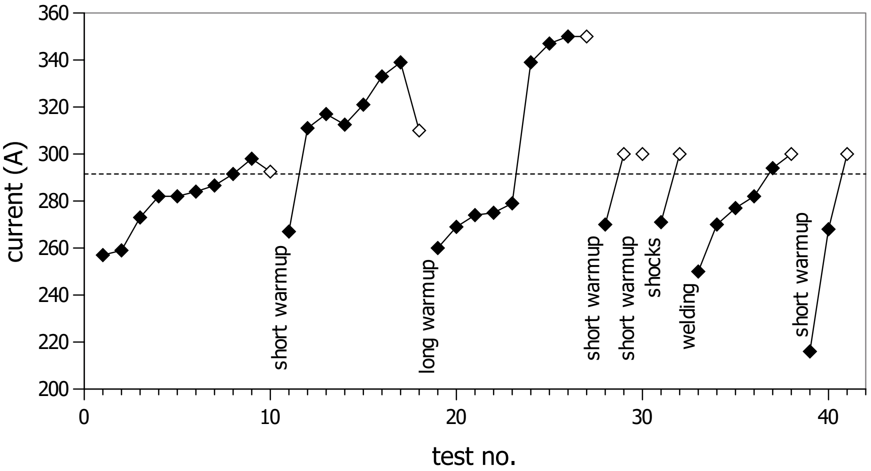

Figure 4.8: Quench currents (filled dots) during several training runs of the prototype coil. Currents that were reached without a quench are indicated by empty dots; broken lines indicate a temperature cycle. Short periods at room temperature required at most two training quenches before the nominal current was reached again. The third training run was preceded by several months at room temperature. A piece of stainless steel was welded onto the coil before the second-to-last run.

After this test we warmed up the coil, dismounted it from the cryostat, and subjected it to shocks and vibrations typical of disassembly and transport. An attached acceleration sensor recorded vibrations with a frequency of 16 kHz and an amplitude of up to $7000\,\mathrm{m\,s^{-2}}$ over 100 µs and shocks of up to $35\,\mathrm{m\,s^{-2}}$ over 40 ms. This treatment also incited only a single quench until the nominal current could be reached again.

After another temperature cycle up to 290 K no quench at all was required.

Finally, a piece of steel was TIG-welded onto the coil's steel housing. This heat input largely reset the previous training and after the second-to-last cool-down five quenches were required to again reach nominal current. The magnets will most likely have to be completely re-trained after welding.

4.2.2 First stack of three outer coils

In 2013, the first three outer coils *OC24+*, *OC17-*, and *OC23+* were delivered (figure 4.9) [88]. Since qualification of the welding procedure was delayed, they were clamped together with a steel bracket. Unfortunately, during high voltage tests the wire entry and exits did not withstand more than 3.5 kV, which is well below the inductive voltages they can experience during a quench. Therefore, the coils were individually bridged with protection diodes.

During training in CoTEx, the quench current steadily increased at first but dropped again in the fifth and sixth quench (figure 4.10, left) [89]. We stopped the training at this

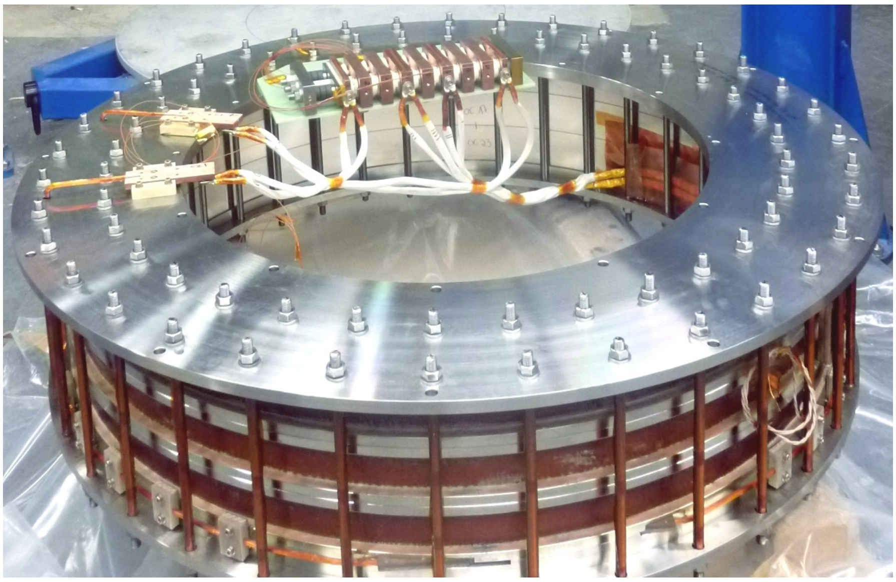

Figure 4.9: Stack of three outer coils—*OC24+*, *OC17-*, and *OC23+*—clamped together by a bracket. Also shown are the array of protection diodes (top center) and the current terminals (left). The whole assembly has a diameter of about 1.4 m.

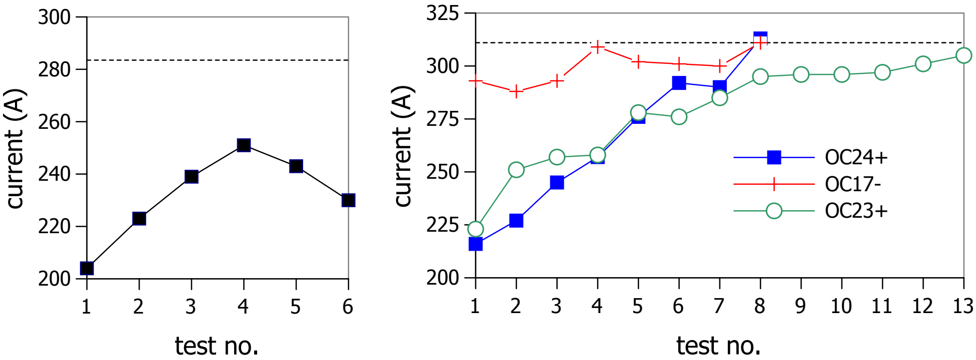

Figure 4.10: Quench currents during training of the clamped stack of three outer coils (left) and of the individual coils (right). The dashed lines indicate the nominal current.

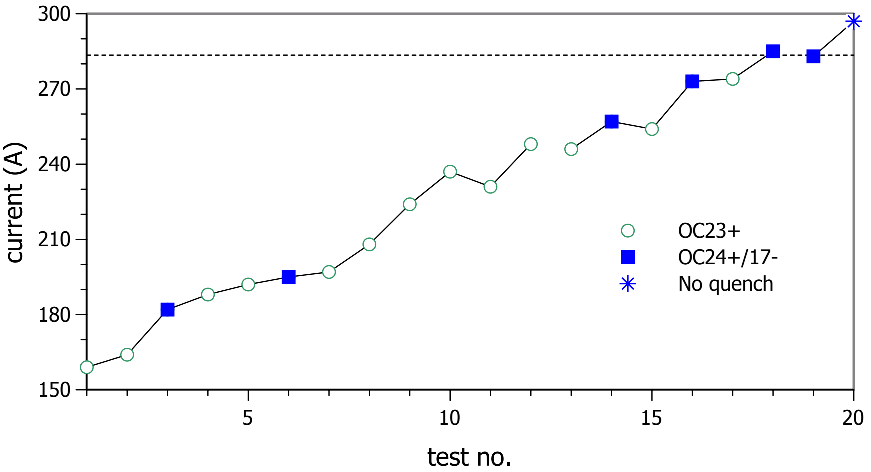

Figure 4.11: Quench currents during training of the welded stack of three outer coils. After twelve quenches the helium reservoir was depleted and the coil warmed up to 250 K. The nominal current was finally reached after 18 quenches. After a temperature cycle to room temperature and another quench, 105 % of the nominal current were reached.

point and decided to test the coils individually to exclude the possibility of a defect in one of the coils. The nominal current of the individual coils was increased to 311 A to operate them at nominal load. The coils behaved quite differently (figure 4.10, right): *OC24+* showed steady increase in quench current until the nominal current was reached after eight quenches; *OC17-*'s quench current initially was much higher and then fluctuated before nominal current was reached; *OC23+* trained much slower than the other two but eventually reached 97 % of the nominal current after 13 quenches.

Since the individual tests showed no defects, the coils were welded together and trained again. As in the welding test with the prototype coil the training was lost during welding. Nevertheless, the quench current increased steadily and 105 % of the nominal current were reached after 19 quenches (figure 4.11). The temperature data allowed us to determine which coil caused each quench.

The first two quenches were caused by *OC23+* and were followed, within ten seconds, by quenches of *OC17-* (figure 4.12). At currents above 180 A either *OC24+* (figure 4.14) or *OC23+* (figure 4.13) quenched simultaneously with *OC17-*. In all three cases the remaining coil stayed superconducting until the magnet was fully discharged by the diodes and dump resistor. The discharge took several minutes, during which the quenched coils returned to their superconducting state.

Above a current of 230 A the remaining coil also quenched within ten seconds of the first quenches (figures 4.15, 4.16). Peak temperatures were significantly increased at these higher currents.

Eventually, at the highest currents above 270 A, all three coils quenched simultaneously (figure 4.17).

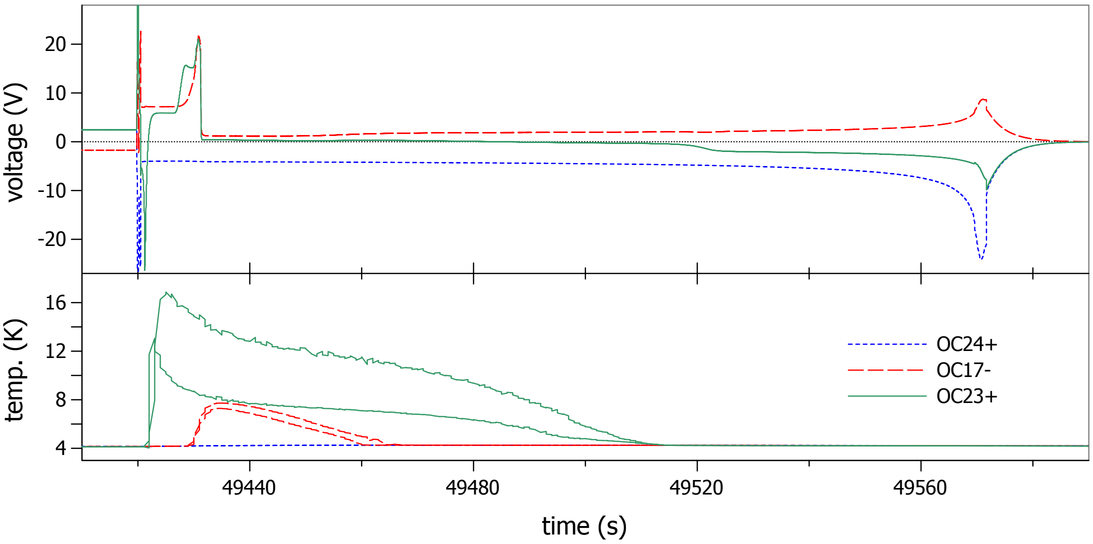

Figure 4.12: Voltage and temperature evolution during a quench of *OC23+* at a current of 164 A. It was shortly followed by a quench of *OC17-* while *OC24+* remained superconducting.

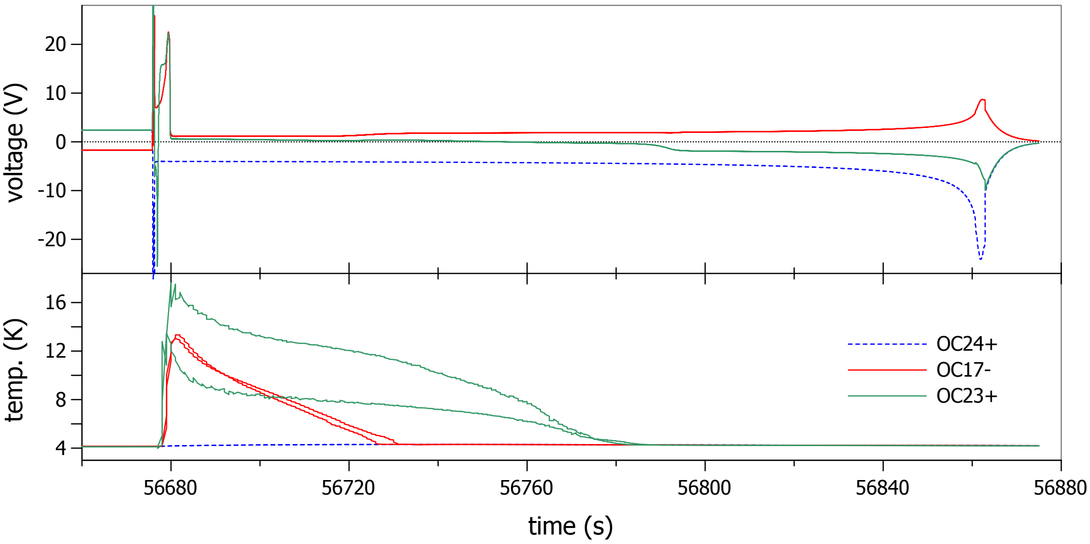

Figure 4.13: Voltage and temperature evolution during an almost simultaneous quench of *OC23+* and *OC17-* at a current of 192 A. *OC24+* remained superconducting.

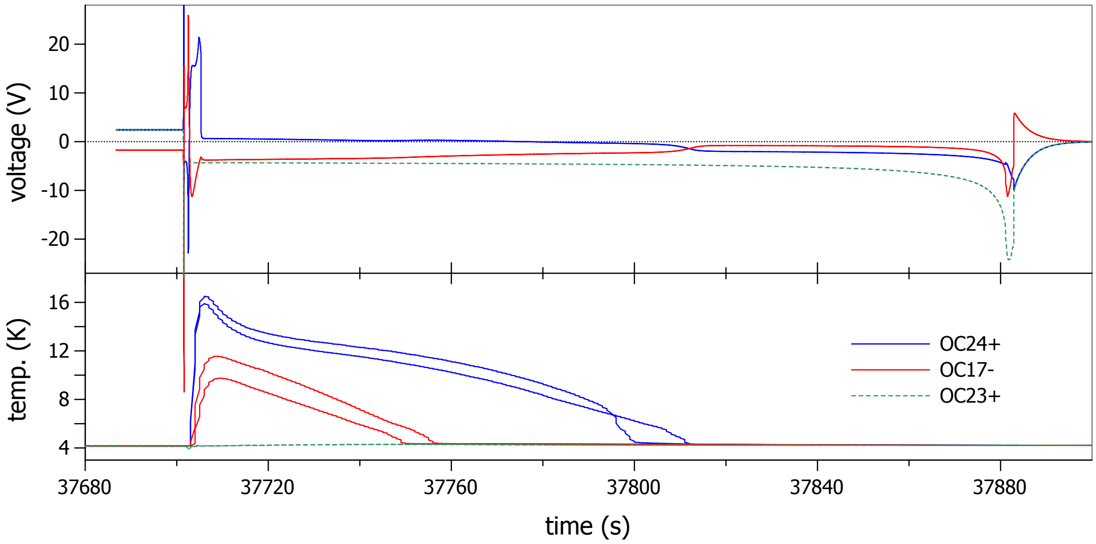

Figure 4.14: Voltage and temperature evolution during a simultaneous quench of *OC24+* and *OC17-* at a current of 195 A. *OC23+* remained superconducting.

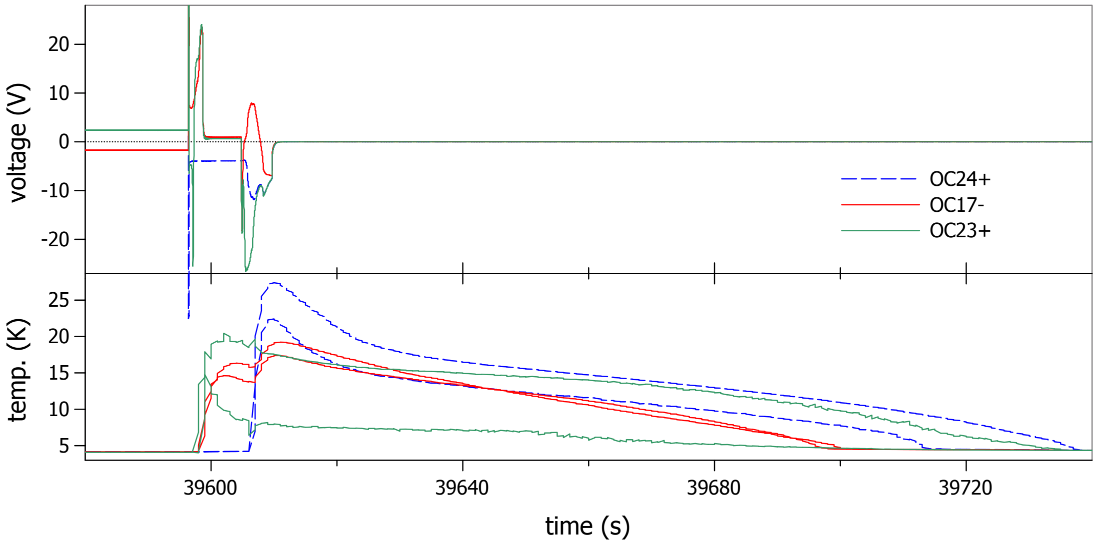

Figure 4.15: Voltage and temperature evolution during an almost simultaneous quench of *OC23+* and *OC17-* at a current of 254 A. *OC24+* quenched about ten seconds later.

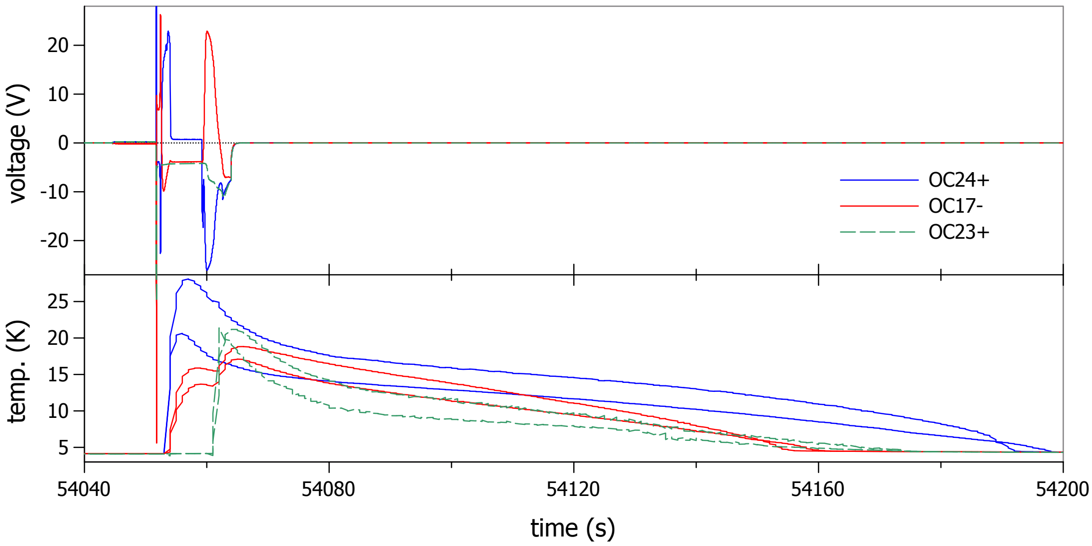

Figure 4.16: Voltage and temperature evolution during a simultaneous quench of *OC24+* and *OC17-* at a current of 257 A. *OC23+* quenched about ten seconds later.

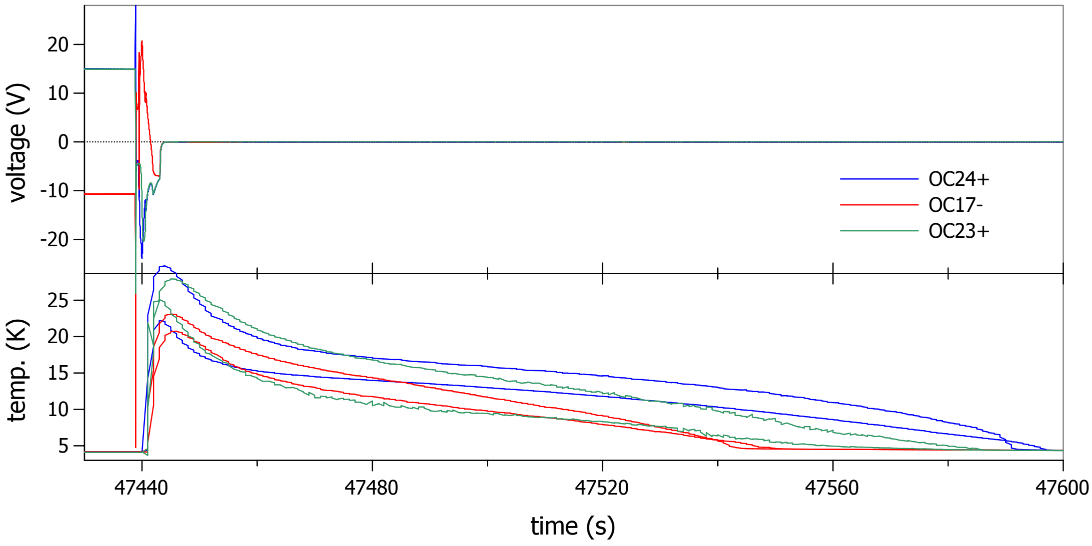

Figure 4.17: Voltage and temperature evolution during an almost simultaneous quench of all three coils at a current of 285 A.

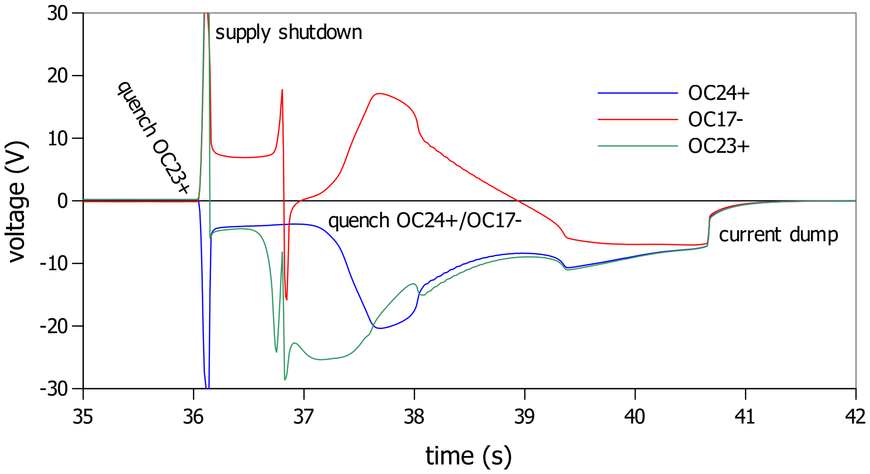

Figure 4.18: Detailed voltage evolution during a quench of *OC23+* at 274 A.

A quench in any coil leads to rapid changes in current, voltage, and magnetic flux. These disturbances are most likely the cause for simultaneous quenches of several coils. The quenches with several seconds delay are most likely caused by the heat produced in quenched coils, which is then slowly conducted to the neighboring, still superconducting, coils.

The voltage data allows a more detailed look into the behavior of the coils during a quench. During ramping, the voltage across *OC24+* and *OC23+* is positive. The voltage across the central coil, *OC17-*, is negative, due to its negative mutual inductance.

During a quench, one of the coils becomes resistive and the power supply sharply increases its voltage to sustain the required current. The increased voltage allows the current to flow through the protection diodes parallel to the quenched coil and increases the voltage drop across it. Despite the power supply's efforts the current drops and the other, still superconducting coils start to discharge and revert their polarity (figure 4.18).

The quench protection detects the rising voltage and quickly shuts down the power supply. Now, all three coils discharge through the anti-parallel diodes and the dump resistor and the polarity of the quenched coil is inverted, too.

The voltage data shows that *OC23+* always quenched first during the simultaneous quenches of *OC23+* and *OC17-*—confirming again that *OC23+* trains much slower than the others. The simultaneous quenches of *OC24+* and *OC17-* could not be separated, even in the voltage data. The complete quenches above 270 A were most likely caused by *OC23+* in one case and by *OC24+* and *OC17-* simultaneously in the other three cases.

Once the power supply is shut down, the voltages across the coils are dictated by their mutual inductances and the complicated temperature- and magnetic-field-dependent diode characteristics, making them difficult to interpret.

After the training, the coil stack was able to carry the nominal current for two hours and could be ramped ten times in quick succession with the nominal rate of 3 A s^{-1} without any quenches.

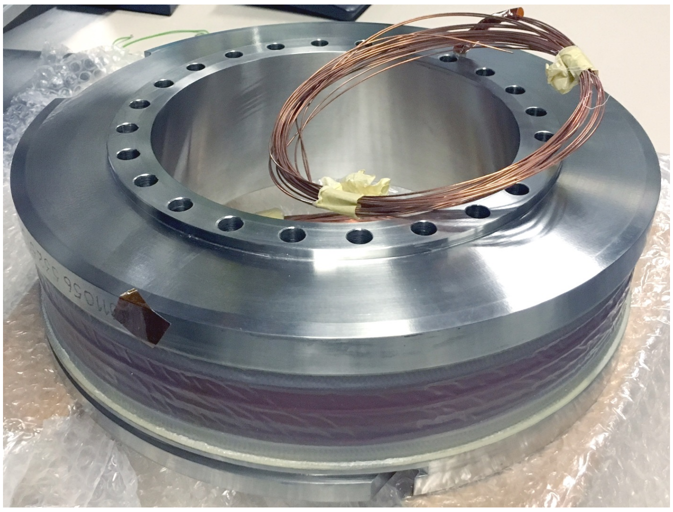

Figure 4.19: Photograph of the inner coil *IC7+*. The outer diameter is 300 mm.

4.2.3 First inner coil

To complete the tests of individual coils, a single inner coil *IC7+* was manufactured (figure 4.19). This time, we lowered the nominal current to 270 A to operate the coil at nominal load. During training, we observed large fluctuations in quench current and the coil was not able to carry 105 % of the nominal current for more than a few minutes (figure 4.20). However, we were able to operate it at nominal current for one hour and ramp it with nominal rate five times in quick succession.

4.2.4 Characterization of protection diodes

To avoid excessive voltages and heating during a quench, the magnet is subdivided and each part is bridged by an array of diodes. While the magnet is superconducting the voltage drop over the magnet is low and the diodes conduct only a very small leakage current. However, once a quench causes a large resistive voltage drop the diodes take over the majority of the magnet current, preventing excessive energy dissipation inside the coil.

The prototype coil was protected by two anti-parallel pairs of *DYNEX DS502ST14* high-power rectifier diodes [90] with a breakthrough voltage of ca. 0.7 V at room temperature. However, their exact characteristics in a superconducting magnet environment, at a temperature of 4.2 K and in a magnetic field of several Tesla, were not known.

During the prototype tests we characterized a single diode clamped between two copper blocks. A *Voltcraft DPS-4005PFC* power supply periodically stepped through forward voltages from 0 V to 8 V and we recorded the forward current and the diode temperature measured by a Cernox sensor attached to the ceramic diode housing. The same was repeated with the prototype coil powered with a current of up to 350 A, which corresponds to a magnetic field of up to 1.8 T at the position of the diode. The orientation of the

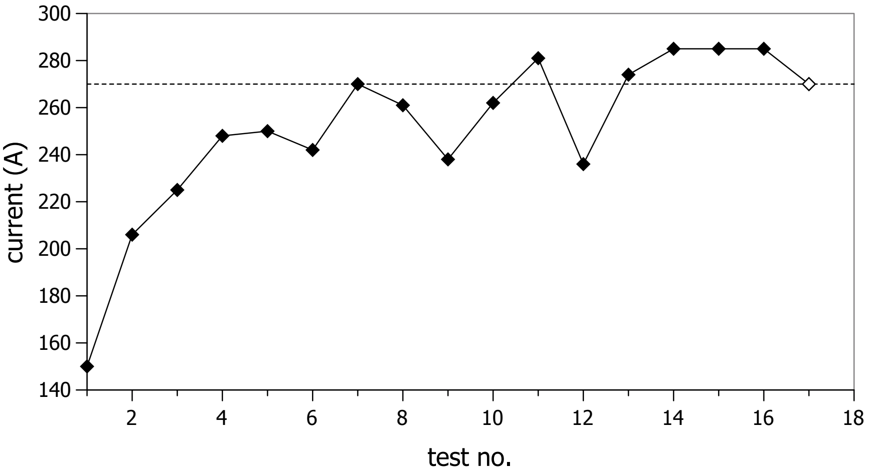

Figure 4.20: Quench currents during training of the inner coil *IC7+*. In the last test (empty dot) the nominal current was reached without a quench.

diode with respect to the magnetic field was rotated in between tests so that the current flow through the diode was either approximately parallel or approximately perpendicular to the magnetic field.

The results show that the breakthrough voltage gradually increases from 0.5 V at 250 K to 1.0 V at 22 K. Here, it begins to rapidly change, reaches 5.3 V at 4.3 K (figure 4.21), and the increase in forward current becomes shallower. This is a well-known effect that has applications in temperature measurements with silicon diodes [91, 92].

When a magnetic field is applied transverse to the current flow through the diode (figure 4.22) the breakthrough voltage increased to up to 16 V at a magnetic field of 1.8 T. The shallower increase in forward current increases the forward voltage at large currents of several ampere to more than 25 V. A field parallel to the current flow had a much smaller effect on the diode characteristic. The increase in breakthrough voltage seen in figure 4.23 is partly caused by a slight misalignment of the diode with the field; a transverse field component amounting to ca. 5 % of the parallel component is still present. Similar effects in magnetic fields have been observed by Aldridge et al. [93].

A voltage $U = L \cdot dI/dt$ is required to ramp up the current I in a coil with inductance L. The breakthrough voltage of the array of protection diodes has to be higher than this ramping voltage to not bypass too much current around the coil. The measured characteristics help to determine the number of diodes required for each individually protected part of the magnet. The increase of forward voltage at low temperatures and in high magnetic fields also explains the larger-than-expected voltage of more than 30 V during a quench (figure 4.6). The subsequent drop in voltage is caused by the break-down of the magnetic field and by heating of the diodes by the large currents flowing through them.

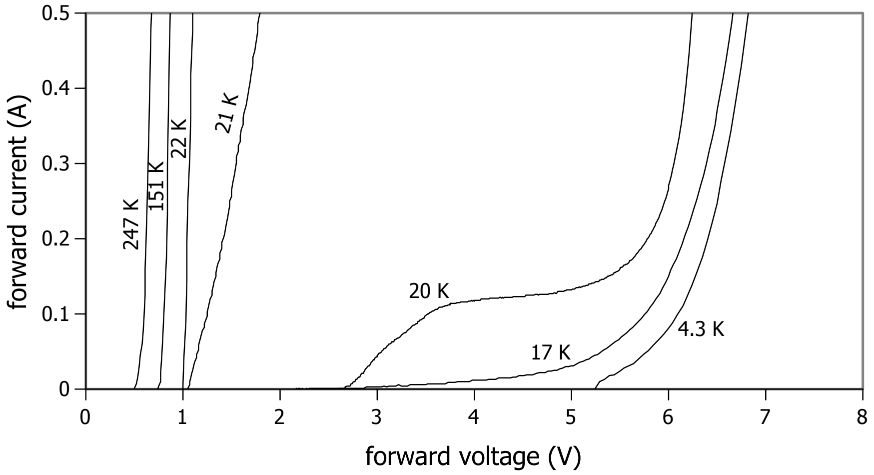

Figure 4.21: Forward current of a DYNEX DS502ST14 high power rectifier diode at different temperatures.

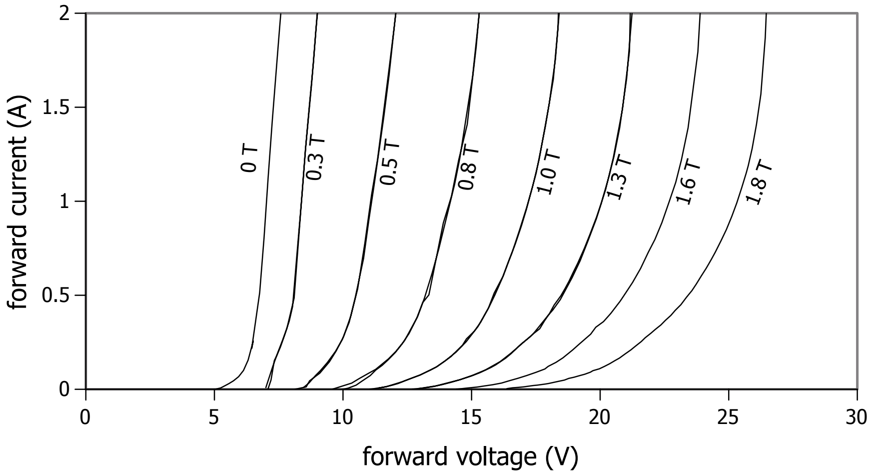

Figure 4.22: Forward current of a DYNEX DS502ST14 high power rectifier diode at 4.2 K and in different magnetic fields transverse to the current flow through the diode.

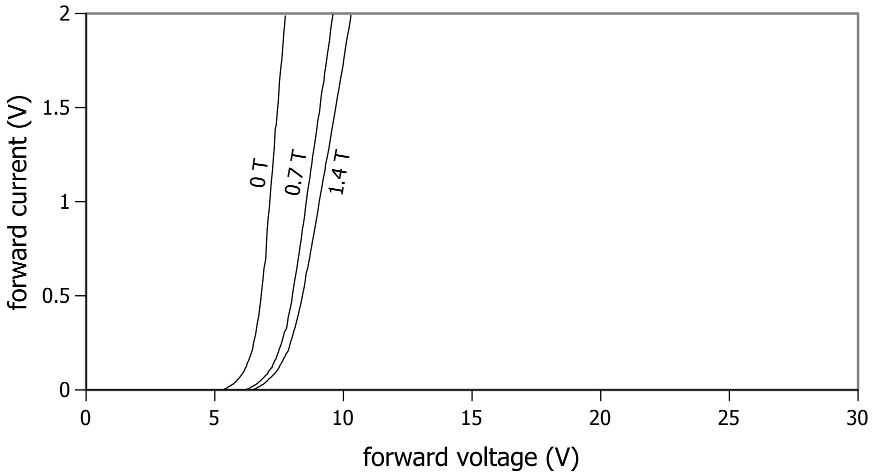

Figure 4.23: Forward current of a DYNEX DS502ST14 high power rectifier diode at 4.2 K and in different magnetic fields approximately parallel to the current flow through the diode.

4.2.5 Experiments with partial cooling

In contrast to the tests in CoTEx, the coils in PENeLOPE's cryostat are not completely immersed in liquid helium (figure 4.24). Instead, they are in contact with the helium bath only on one of four sides and through some narrow cooling channels. The other three sides are attached to the neighboring coils or exposed to the insulating vacua where they are subject to radiative heating from radiation shields cooled by liquid nitrogen.

To approximate this situation in CoTEx, the prototype coil was operated at the highest possible load, continuously ramping it up to 300 A and down again, while the liquid helium level was allowed to drop below the upper edge of the coil housing. To avoid heating of the coil through its normal-conducting current terminals the coil was mounted upside down so that the terminals would be the last part to lose contact with the helium bath.

During this test no quenches were observed until the coil housing completely lost contact with the helium bath when the helium level dropped below its lower edge. At this time the normal-conducting current terminals were still immersed in liquid helium. Right before the quench at 301 A, at the highest load during a ramping cycle, the temperature sensor on the upper side of the coil showed a temperature, T_s, of 5.4 K, which coincides very well with the critical temperature of the superconductor at nominal load (figure 4.2).

CoTEx's liquid helium tank can be considered a closed box where the top—the lid of the liquid-helium tank—is hotter than the bottom—the liquid-helium surface. In such a case, there is no convective heating; only conductive heating through gaseous helium above the surface and radiative heating from the lid have to be considered [94].

Using thermal-conductivity data from Steinmann [83], Lemmon et al. [95], and Mar-

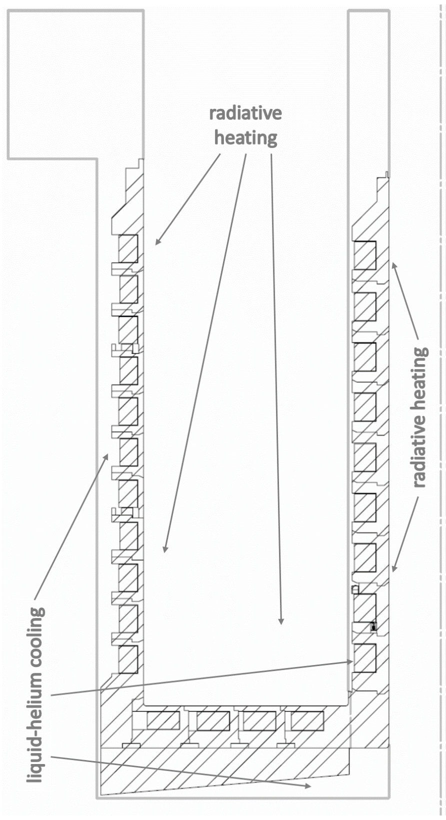

Figure 4.24: Schematic view of PENeLOPE's magnet and its liquid-helium reservoir, indicating liquid-helium cooling and radiative heating.

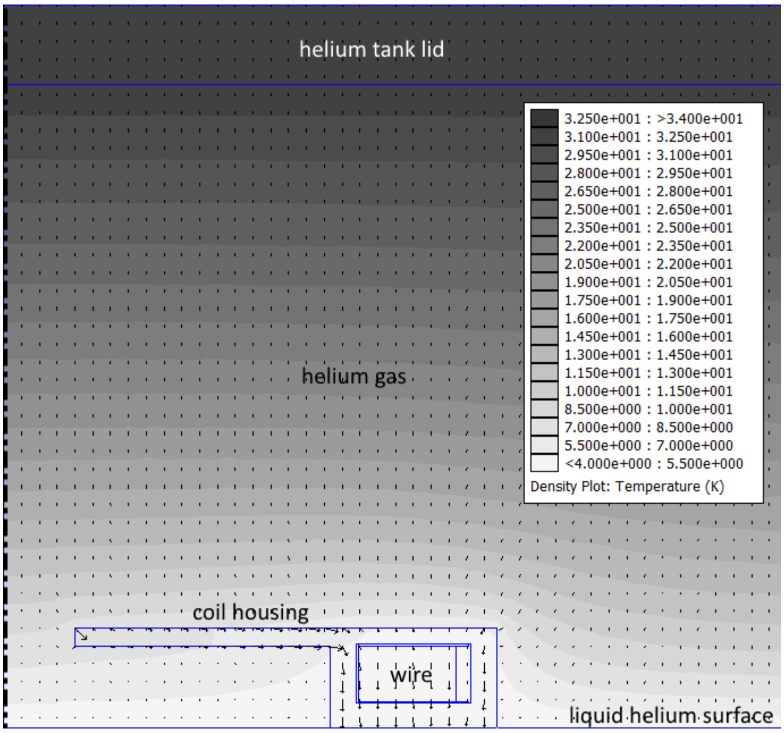

Figure 4.25: Simulated temperature distribution and heat flux by conductive heating in CoTEx's helium tank and the partially cooled coil.

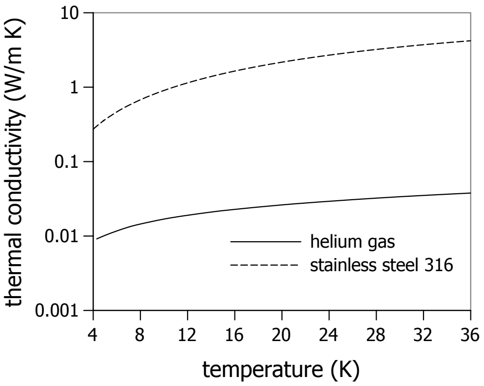

Figure 4.26: Thermal conductivity of helium gas and stainless steel at cryogenic temperatures [95, 96].

quardt et al. [96] (figure 4.26), I modeled the coil as a rotationally symmetric heat-flow problem in FEMM [97]. Following Steinmann [83], I set heat generation due to coupling losses and hysteresis losses in the wire package to $150\,\mathrm{W\,m^{-3}}$ and heat generation due to eddy currents in the stainless steel housing to $4\,\mathrm{W\,m^{-3}}$. I fixed the upper boundary condition to the temperature of the helium tank's lid measured during the test—35 K—and the lower boundary to the liquid-helium temperature of 4.3 K.

The resulting temperature distribution and heat-flux density is shown in figure 4.25. The upper coil edge has a simulated temperature of 5.4 K, very close to the measured value. The total simulated heat flux into the coil is 0.5 W. This is in the same order as the maximum radiative heat transfer,

$$Q_r = A\sigma(T_\mathrm{N}^4 - T_s^4) = 0.28\,\mathrm{W}, \tag{4.1}$$

from a liquid-nitrogen-cooled radiation shield with a temperature, T_N, of 77 K, to the coil's surface area, A, of $0.14\,\mathrm{m}^2$ with a temperature, T_s, of 5 K, according to the Stefan-Boltzmann law. In PENeLOPE, almost all surfaces exposed to radiative heating are covered with multi-layer insulation foil, which typically reduces radiative heat transfer by a factor of 20 to 40 [98].

This result shows that the coils can operate at similar, or even higher, heat loads than those expected in PENeLOPE—even if they have only partial contact with liquid helium.

4.2.6 A slow-control system for the coil-test experiment CoTEx

The purpose of a slow-control system is to record and control all slowly varying parameters of an experiment like temperatures, pressures, coolant flow rates, and coolant levels. This is in contrast to fast data-acquisition (DAQ) systems that record fast events with high data rates, e.g. from particle detectors.

Such a slow control already existed for CoTEx, based on several separate devices read out by a PC via RS-232 and USB connections using *National Instruments LabVIEW*. However, due to the wide range of different devices this system had stability issues and only rudimentary recording functionality, storing the sensor data in text files.

The CompactRIO platform

Using the *National Instruments CompactRIO* platform, we built a more integrated system. The CompactRIO platform uses an industrial real-time processor with a Linux real-time operating system in a chassis with up to eight module slots. It can be equipped with a wide range of modules to measure voltages, currents, and temperatures, and to control relays. The modules are read out by a *Xilinx* Field Programmable Gate Array (FPGA), which can be manually programmed for high-speed signal acquisition and processing. The CompactRIO platform can be expanded into a distributed system with additional module chassis via Ethernet or EtherCAT connections. This modularity and scalability also makes it potentially usable as a slow-control system for PENeLOPE. [99]

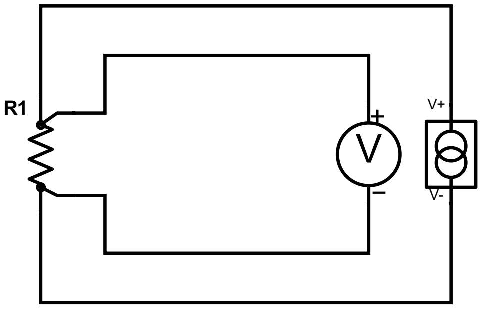

Figure 4.27: Four-wire measurement to precisely determine the electrical resistance R1 of a resistance thermometer.

Sensors and devices

Temperature Temperature measurements are vital to ensure that the cryostat and coils are cooled properly and the temperature evolution in the coils during a quench provides information which coil actually quenched. Throughout CoTEx, resistance temperature detectors (RTDs) are used and read out by four-wire measurements (figure 4.27). A precise constant-current source sends a small excitation current through the resistance thermometer and the resulting voltage drop is measured by two additional leads directly attached to the resistor terminals. This eliminates the voltage drop across the potentially long current leads and allows very precise measurements of the resistance.

For higher temperatures—mostly on the radiation shield cooled by liquid nitrogen—*PT100* sensors with a standardized resistance-temperature curve, typically accurate to temperatures down to 70 K, are used [100]. CompactRIO modules for this type of sensor are readily available and use an excitation current of 1 mA.

For even lower temperatures on the liquid-helium tank or on the coil itself we use Cernox sensors [101]. These do not follow a standard curve but are individually calibrated to temperatures down to 4 K by the manufacturer, making them much more expensive. Due to their large resistance and low specific heat at low temperatures an excitation current of 1 mA would lead to significant self heating and would distort the temperature measurement. Instead they are read out by Lake Shore LS218 temperature monitors using a pulsed excitation current of only 1 µA [102]. These are read out via a serial RS-232 connection by a CompactRIO RS-232 module.

Pressure Low vacuum pressures are required to isolate the liquid-helium tank from its surroundings. In CoTEx, this pressure is read out by two *Oerlikon Leybold Penningvac PTR90* or *Ionivac ITR90* full-range sensors [103, 104]. These can switch between different types of measurement for different pressure ranges and are controlled by a *Leybold CENTER THREE*, which is read out via an RS-232 interface [105].

Helium-gas pressures are measured by *WIKA* membrane pressure sensors [106]. They are supplied with a voltage of 24 V and adjust their internal resistance such that a

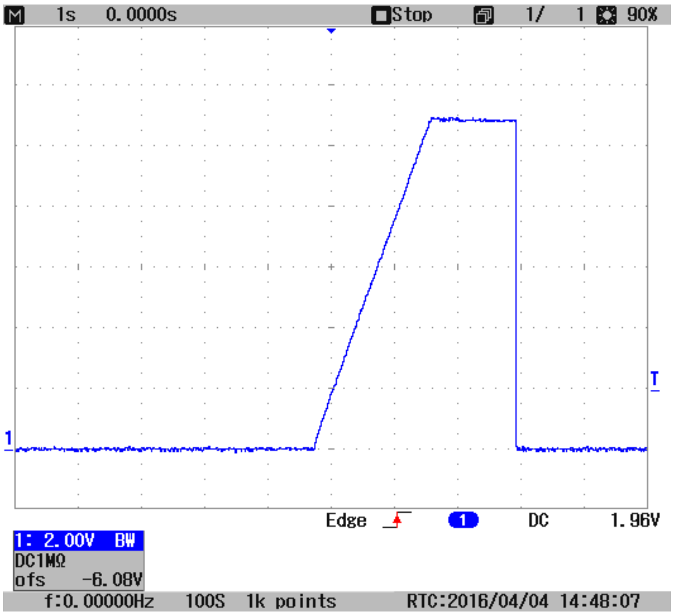

Figure 4.28: Voltage signal of a liquid-helium-level measurement with a superconducting-filament sensor. The voltage reaches a plateau at about 11 V, corresponding to a fill level of about 47 % along the sensor with a length of 61 cm.

current of 4 mA to 20 mA—proportional to the pressure—is flowing from the voltage source through the sensor to ground. The current is measured by a CompactRIO current-measurement module.

Liquid-helium level To efficiently cool the coils during testing they should be completely immersed in liquid helium. This is ensured by liquid-helium-level sensors using a superconducting filament provided by American Magnetics Inc. [107]. The part of the filament immersed in liquid helium becomes superconducting and the total resistance, determined by a four-wire measurement, drops when the helium level rises. A large excitation current, I_{exc}, of 75 mA is used. This large current heats the upper part of the filament and ensures that it stays normal-conducting.

Due to this high excitation current and correspondingly high voltage, a specialized *American Magnetics Model 135* readout device is used [108]. Since it does not have a standard interface the voltage drop over the filament is directly measured by a CompactRIO voltage module and the signal is analyzed by the CompactRIO's FPGA.

To reduce heat dissipation and helium evaporation the excitation current is applied once every minute for about 3 s. During this time the voltage drop over the filament quickly increases while the top part of the filament is heated and becomes normal-conducting, until the voltage reaches a plateau (figure 4.28). This voltage level U is proportional to the resistance of the part of the filament above the liquid-helium level. The manufacturer specifies a resistance, R, of 4.5 $\Omega\,\text{cm}^{-1}$. The liquid-helium level along

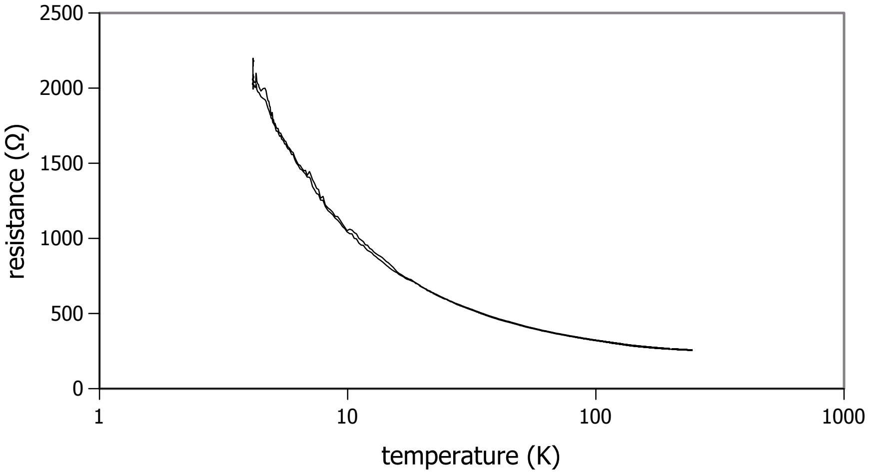

Figure 4.29: Resistance of two carbon foil resistors measured while CoTEx was warming up.

the length of the sensor, L, is then given by $L - U/\left(I_{\mathrm{exc}}R\right)$.

Liquid helium has a specific latent heat of $2.6\,\mathrm{kJ\,l^{-1}}$ [109]. The heat dissipation during a measurement is in the order of 1 W over three seconds and evaporates about 1 ml of liquid helium, a negligible amount.

Kolhep [110] tested a different approach with carbon-film resistors. Their electrical resistance has a large temperature dependence (figure 4.29). Once they are in contact with liquid helium, the heat dissipated in the resistor is removed much quicker, leading to a drop in internal temperature and an increase in resistance. This gives binary information if the helium level has reached the precisely known position of the resistor or not.

However, the small increase in resistance due to the increased dissipation is difficult to detect amidst changes due to temperature fluctuations in gaseous helium. This requires a precise resistance measurement and the observed changes have to be carefully correlated with temperature measurements of the resistor's environment (figure 4.30). Sensitivity might be improved by tuning the excitation current of the resistor and by using a properly designed measurement circuit, as described by Crisp and Rungis [111].

Control In addition to the described passive monitoring by the slow-control system, we added active control of vacuum shutters, vacuum pumps, the magnet power supply, liquid-nitrogen flow, and heaters. Vacuum shutters and pumps are controlled via a CompactRIO relay module and a 24 V voltage source. The magnet power supply is controlled via Ethernet. The flow controller, which controls the flow of liquid nitrogen through the radiation shield is controlled via RS-232. Heaters on the helium tank, used to reduce the time required to warm up the cryostat, are powered by a power supply that is controlled by a CompactRIO voltage-output module.

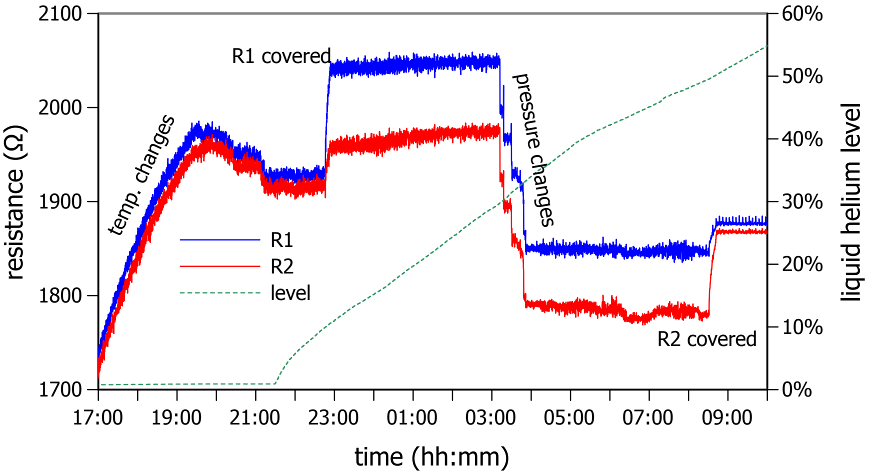

Figure 4.30: Resistance of two carbon foil resistors, R1 and R2, while CoTEx was filled with liquid helium. The helium level was measured with a superconducting-filament sensor.

Quench protection

In addition to the slow-control system, CoTEx—and later PENeLOPE—require an active quench-protection system. It monitors the voltages across each set of protection diodes and quickly shuts down the magnet power supply if a quench is detected. Otherwise the power supply would continue to increase the voltage to keep the current stable and put more power into the now resistive coils. Previously, the voltages were recorded with a USB oscilloscope attached to the control PC. A complicated LabVIEW algorithm detected the quickly rising voltage during a quench and switched a separate USB relay to open an interlock in the magnet power supply to quickly shut it down [86]. This complicated system failed to detect a quench at least once during the initial testing of the prototype coil. The power supply excessively heated the coils and diodes and quickly evaporated a large amount of liquid helium, which blew out a burst disk and led to a loss of a large amount of helium.

The CompactRIO's FPGA offers a reliable way to sample and monitor the magnet voltages at high rate and very quickly switch a relay to open the power-supply interlock. Thanks to the now well-known diode characteristics the quench-detection algorithm could be simplified—shutting down the power supply once one of the voltages crossed a threshold showed to be sufficient.

To detect these voltage spikes, differential voltages between each set of bridged coils have to be measured. Additionally, the zero-voltage level of the four-quadrant magnet power supply is offset from ground by 75 V. Therefore, *NI9229* voltage modules with isolation amplifiers—capable of measuring differential voltages of up to ±60 V—are used. The CompactRIO's FPGA samples these voltages with 100 kHz, averages over 1024 samples to reduce noise, and switches the relay controlling the power-supply interlock, if a

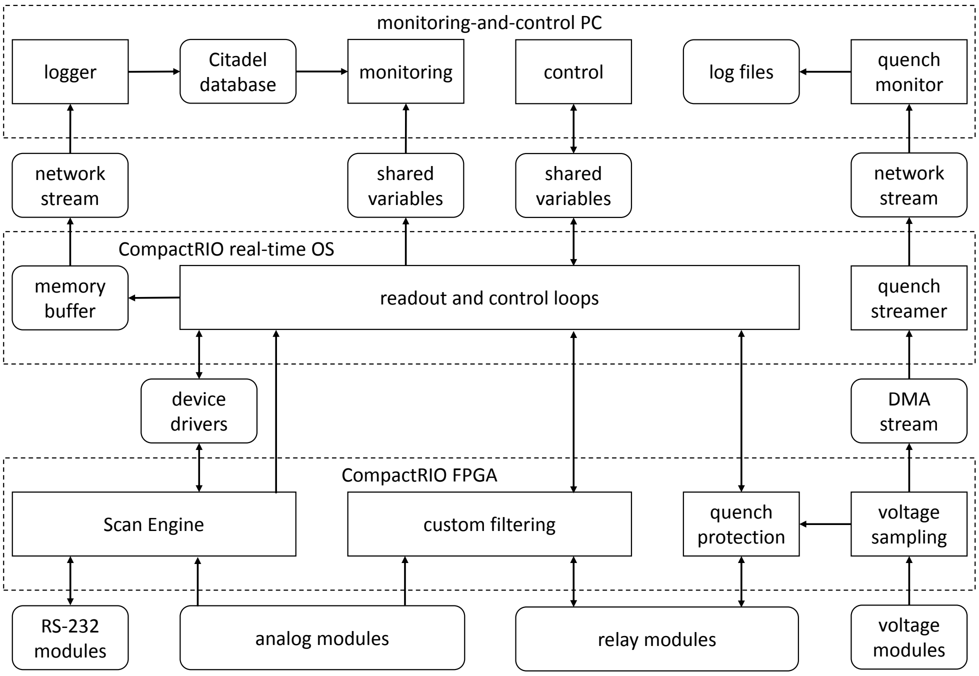

Figure 4.31: Software scheme of CoTEx's slow-control system based on CompactRIO and LabVIEW.

configurable voltage threshold is exceeded (figure 4.3).

Software scheme

The software to monitor and control the system is written in LabVIEW and deployed to three different devices: the CompactRIO's FPGA, the CompactRIO's real-time operating system, and the monitoring-and-control PC (figure 4.31).

The FPGA reads out the connected modules and delivers the data to the real-time operating system via the so-called Scan Engine. Additionally, it can be programmed manually with a small amount of low-level functions for high-speed sampling and filtering of analog and digital channels.

The real-time operating system can read the data from the FPGA with low sampling rate and store small amounts of data in RAM or flash memory. Several means of network communication with the monitoring-and-control PC—e.g. network streams to transmit large amounts of data and network-shared variables that only contain the latest sampled value of a channel—are available [99]. A large number of device drivers for the real-time operating system is available to read out devices via RS-232 or Ethernet.

Most of the channels are read out twice per second in individual readout loops, the data is paired with the current time stamp, and stored in a buffer queue in RAM. This buffer allows for short interruptions in network connectivity and data logging without loss of data.

The monitoring-and-control PC runs three different programs:

- a logger that connects to the CompactRIO via a network stream, reads the buffered data, and stores it in a Citadel database provided by LabVIEW's *Datalogging and Supervisory Control* package;
- a monitoring program that displays current sensor values from network-shared variables and past data from the Citadel database; and
- a control program used to display and set control parameters in the CompactRIO software via network-shared variables.

Data from the high-rate voltage sampling by the quench-protection program is streamed directly from the FPGA, translated into a network stream by the real-time operating system, and received and logged on the monitoring and control PC with a separate quench-monitor program.

4.3 Thermodynamics of ultracold neutrons in an external potential

Despite the fast ramping rate of the magnet the time scale is sufficiently long that ultracold neutrons partially stay in thermodynamic equilibrium with the external potential, $U(\mathbf{x})$,[1] created by the magnetic field, $B(\mathbf{x})$, and gravity, g_0:

$$\begin{aligned} U(\mathbf{x}) &= \pm\mu_\mathrm{n} B(\mathbf{x}) + m_\mathrm{n} g_0 z \\ &= \pm 60.3\,\mathrm{neV\,T^{-1}} \cdot B(\mathbf{x}) + 103\,\mathrm{neV\,m^{-1}} \cdot z. \end{aligned} \tag{4.2}$$

UCN do not exchange energy with each other or the walls, so the ensemble of microstates available to a UCN with total energy H can be considered a micro-canonical ensemble. The number of microstates, the phase-space volume $\Omega(H)$, is proportional to the integral over the whole spatial and momentum space where the UCN's kinetic and potential energy equal its total energy:

$$\Omega(H) \propto \int \mathrm{d}^3\mathbf{x} \int \mathrm{d}^3\mathbf{p}\, \delta\left(H - \frac{\mathbf{p}^2}{2m_\mathrm{n}} - U(\mathbf{x})\right). \tag{4.3}$$

The integrand only depends on the squared momentum, $\mathbf{p}^2$, and the integral over momentum space can be replaced by an integral over kinetic energy, $E = \mathbf{p}^2/2m_\mathrm{n}$:

$$\mathrm{d}^3\mathbf{p} = 4\pi\mathbf{p}^2\,\mathrm{d}|\mathbf{p}| = 4\pi m_\mathrm{n}\sqrt{2m_\mathrm{n}E}\,\mathrm{d}E. \tag{4.4}$$

This transformation yields

$$\Omega(H) \propto \int \mathrm{d}^3\mathbf{x} \int \mathrm{d}E\,\sqrt{E}\delta\left(H - E - U(\mathbf{x})\right). \tag{4.5}$$

---

[1] $\mathbf{x} = (x\ y\ z)^\mathrm{T}$

Kinetic energy is always positive, which excludes any phase-space volume where $U > H$ from the integral. Carrying out the energy integral then gives

$$\Omega(H) \propto \int\limits_{U(\mathbf{x})<H} \mathrm{d}^3\mathbf{x}\,\sqrt{H - U(\mathbf{x})}. \tag{4.6}$$

Since every microstate is populated with equal probability, the UCN density $\rho(\mathbf{x}, H)$ is proportional to the number of microstates at point $\mathbf{x}$:

$$\rho(\mathbf{x}, H) \propto \sqrt{H - U(\mathbf{x})}. \tag{4.7}$$

From equation (4.6) one can also calculate the Boltzmann entropy

$$S_\mathrm{B}(H) = k_\mathrm{B} \ln \Omega(H) + C, \tag{4.8}$$

where k_B is the Boltzmann constant and C is the logarithm of a proportionality constant.

In the case of a purely gravitational potential $U(\mathbf{x}) = m_\mathrm{n} g z$ in a storage bottle with a constant horizontal cross section, A, and a floor at z_0 one arrives at

$$\begin{aligned}\Omega(H) &\propto \iint\limits_{A} \mathrm{d}x\,\mathrm{d}y \int\limits_{z_0}^{H/m_\mathrm{n}g} \mathrm{d}z\,\sqrt{H - m_\mathrm{n} g z} \\ &= \frac{2A}{3 m_\mathrm{n} g} \left(H - m_\mathrm{n} g z_0\right)^{3/2}\end{aligned} \tag{4.9}$$

and

$$\rho(\mathbf{x}, H) \propto \sqrt{H - m_\mathrm{n} g z_0}, \tag{4.10}$$

the same result as worked out by Golub et al. [41, chapter 4.3].

Figure 4.32 shows the phase-space volume available to UCN in PENeLOPE's storage volume, determined from a magnetic-field map. If one assumes that ramping of the magnet is a quasi-static process, the total energy of a UCN is shifted such that its entropy and its phase-space volume stay constant. This corresponds to a horizontal shift in figure 4.32, from the dashed line to one of the solid lines. The resulting total-energy gain is shown in figure 4.33. Simulation results show that the energy gain is broadened and mostly smaller than predicted, indicating that the ramping of the magnet is not a completely adiabatic, quasi-static process. The phase space of high-field-seekers gets much more compressed which leads to considerably larger broadening of the energy spectrum.

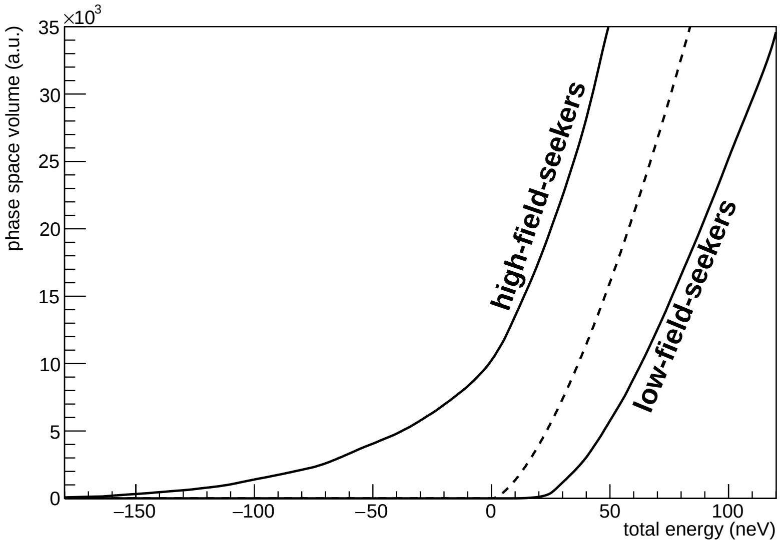

Figure 4.32: Phase-space volume, $\Omega(H)$, available to UCN in PENeLOPE's storage volume before (dashed line) and after (solid lines) ramping of the magnet. The dashed line follows the predicted $H^{3/2}$ dependence.

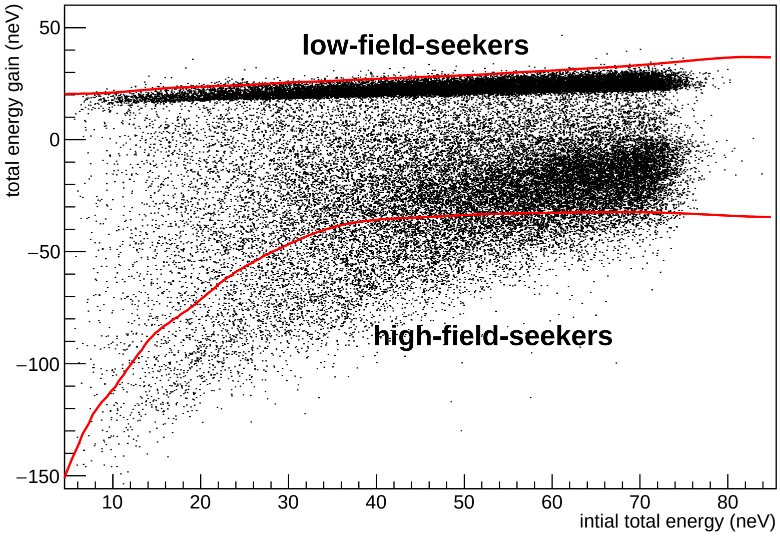

Figure 4.33: Simulated total-energy gain of low- and high-field-seekers in PENeLOPE's storage volume during ramping of the magnet. The red lines indicate the theoretical predictions.

5 Stage IV: Magnetic storage

As soon as PENeLOPE's magnet is ramped to the nominal current the magnetic storage phase begins. At this point, the only loss of neutrons from the storage volume should be due to beta decay.

Any additional loss channels with neutron loss rates τ_i^{-1} will reduce the measured neutron lifetime, τ, compared to the beta-decay lifetime, τ_n:

$$\tau^{-1} = \tau_\mathrm{n}^{-1} + \sum_i \tau_i^{-1}. \tag{5.1}$$

Potential additional loss channels are

- absorption or up-scattering of UCN during interaction with rest gas,
- depolarization of magnetically stored low-field-seekers,
- losses during reflection of marginally trapped low-field-seekers on walls,
- heating of magnetically stored low-field-seekers,
- losses during reflection of high-field-seekers on walls, and
- depolarization during reflection of high-field-seekers on walls.

To achieve an accuracy, $\tau_\mathrm{n} - \tau$, of less than 0.1 s the sum of all additional loss rates has to be smaller than $10^{-7}\,\mathrm{s}^{-1}$.

This chapter estimates the loss rates of these potential loss channels, describes an absorber-actuation mechanism to eliminate distortion of the lifetime measurement due to high-field-seekers, and describes the general proton-detector design.

5.1 Estimation of neutron-loss rates

I used my simulation tool PENTrack to simulate ultracold neutrons during filling, cleaning, ramping, and storage to estimate their loss rates due to these effects. PENTrack performs a high-precision 5th-order Runge-Kutta integration [112] of the equation of motion [1] of a particle with mass m, charge q, and magnetic moment μ in gravitational acceleration $\mathbf{g}$, magnetic field $\mathbf{B}(\mathbf{x})$, and electric field $\mathbf{E}(\mathbf{x})$ [45]:

$$\ddot{\mathbf{x}} = \frac{1}{\gamma m}\left(1 - \frac{1}{c^2}\dot{\mathbf{x}} \otimes \dot{\mathbf{x}}\right)\left[m\mathbf{g} + q\left(\mathbf{E} + \dot{\mathbf{x}} \times \mathbf{B}\right) + P\mu\nabla\left|\mathbf{B}\right|\right]. \tag{5.2}$$

---

[1] $\dot{\mathbf{x}} = d\mathbf{x}/dt$, $\ddot{\mathbf{x}} = d^2\mathbf{x}/dt^2$, $\dot{\mathbf{x}} \otimes \dot{\mathbf{x}}$ is the outer product of the velocity vectors, and γ is the relativistic Lorentz factor

The equation is valid for both non-relativistic and relativistic spin-$\frac{1}{2}$ particles and takes into account Lorentz force and interaction of the magnetic moment with magnetic-field gradients. For the latter, it assumes that the spin of the particle is always (anti-)parallel to the magnetic field, i.e. $P = \pm 1$, which is the case if the condition

$$\frac{2\mu}{\hbar}|\mathbf{B}| \gg \frac{|\dot{\mathbf{B}}|}{|\mathbf{B}|} \tag{5.3}$$

is fulfilled.

5.1.1 Interaction with rest gas

Interactions of stored UCN with rest gas cannot be completely eliminated, but a low vacuum pressure below $5 \cdot 10^{-8}$ mbar reduces the additional loss rate to an acceptable level of $4 \cdot 10^{-8}\,\mathrm{s}^{-1}$ [51].

5.1.2 Depolarization in magnetic field minima

The rotationally symmetric topology of PENeLOPE's superconducting magnet creates a magnetic field in radial and axial directions, without an azimuthal component. Due to the alternating current directions the fields of the individual solenoids cancel each other in some regions of the storage volume. In these regions the condition (5.3) is not fulfilled, the magnetic moment cannot properly align to the magnetic field, and the polarization can be flipped. This effect was already considered in the initial design of the magnet topology and a large electric current flowing through the central axis of the magnet was foreseen [113]. If this central current is chosen large enough it produces an azimuthal field that fills the low-field regions and suppresses depolarization. A current of 10 000 A reduces the depolarization rate to $2 \cdot 10^{-10}\,\mathrm{s}^{-1}$ [51]. However, at least 12 500 A are required, so asymmetries in the superconducting coils cannot cancel the azimuthal field [45].

5.1.3 Marginally trapped neutrons

Marginally trapped neutrons with energies above the trapping potential of 115 neV can overcome the magnetic barrier and hit the walls. Absorption or up-scattering during such an event leads to losses in addition to beta decay.

To estimate this additional loss rate I simulated marginally trapped neutrons with different energies and infinite beta-decay lifetimes while assuming that the trap walls are made of stainless steel with an optical potential of $(183 + 0.0852\mathrm{i})$ neV. The number of marginally trapped neutrons with energies between 115 neV and 150 neV drops exponentially and can be described with a single loss-rate parameter between $10^{-6}\,\mathrm{s}^{-1}$ and $10^{-4}\,\mathrm{s}^{-1}$. Marginally trapped neutrons with energies above 170 neV are split into two populations and are best described as a sum of two exponential functions with two loss-rate parameters. One population is absorbed by the proton detector or can penetrate the magnetic barrier in the feeder and leave the storage volume (dashed line in figure

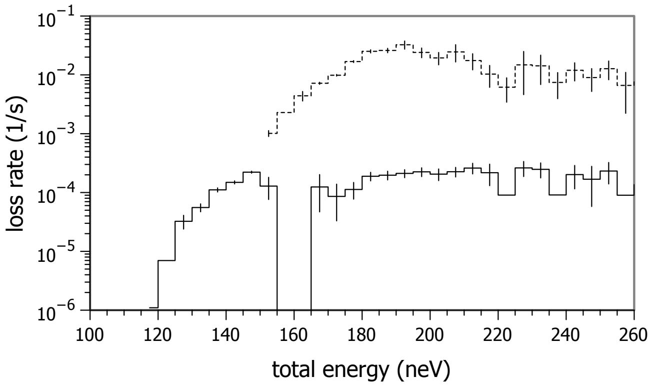

Figure 5.1: Simulated additional loss rate of marginally trapped neutrons in the storage volume. Above 170 neV UCN are split into two populations with different loss rates (see section 5.1.3).

5.1). The other is trapped in quasi-stable orbits in the storage volume (solid line in figure 5.1). The former has a high loss rate of $10^{-2}\,\mathrm{s}^{-1}$ while the latter has a much smaller loss rate of $10^{-2}\,\mathrm{s}^{-1}$. Between 150 neV and 170 neV, the two populations cannot be properly separated and are best described by a single exponential with larger loss rate.

The population of marginally trapped neutrons filled into the trap is reduced to an acceptable number during the previously described cleaning stage (section 3.2). However, some processes—heating of magnetically trapped low-field-seekers and depolarization of high-field-seekers—could increase their number again once the magnet is powered up.

5.1.4 Heating

Fast variations of the magnetic field can heat magnetically stored low-field-seekers and increase their energy above the trapping potential of 115 neV. This effect already played a minor role during ramping (section 4.3). During magnetic storage, the stability of the magnet power supply is crucial. Ripple on its current causes oscillations of the magnetic field and could lead to heating. To study this effect I simulated low-field-seekers stored in a magnetic field with a certain ripple amplitude and frequency for 1000 s. Due to the vibrations of the magnetic field the energies of the neutrons are randomly shifted and the difference between their initial and final energies is broadened over time into a Gaussian distribution (figure 5.2).

The broadening—the standard deviation of this distribution—has a maximum at a ripple frequency of 15 Hz and is linearly dependent on the ripple amplitude (figure 5.3). At very low amplitudes the simulated broadening is dominated by inaccuracies in numerical integration of the UCN trajectory and deviates from the linear dependence.

The datasheet of the *Danfysik System 8500* magnet power supply that will be used to power the superconducting magnet of PENeLOPE specifies a short-term regulation accuracy of less than 5 ppm within 3 ms and a random variation in output voltage of less than 30 mV at frequencies of 1 Hz or more [114]. A voltage of 30 mV, applied to

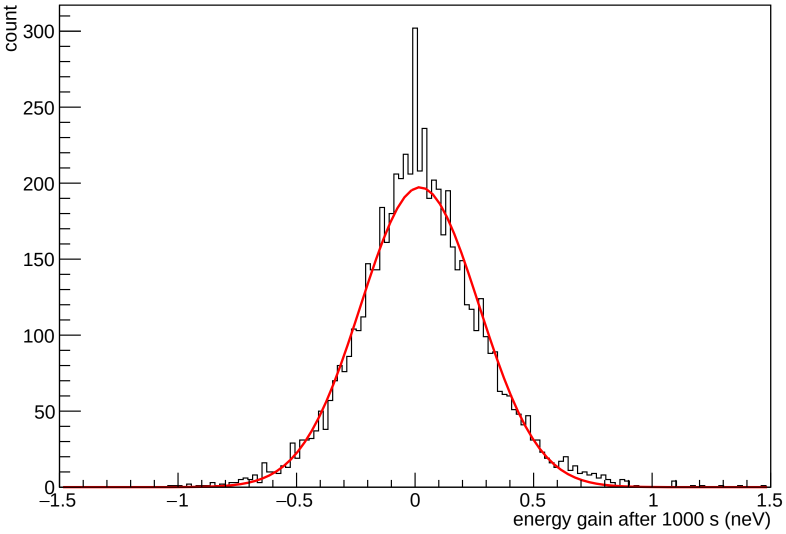

Figure 5.2: Distribution of simulated energy shifts during magnetic storage of low-field-seekers in a magnetic field with a ripple amplitude of 100 ppm and a ripple frequency of 15 Hz. The red line is a fit of a Gaussian distribution.

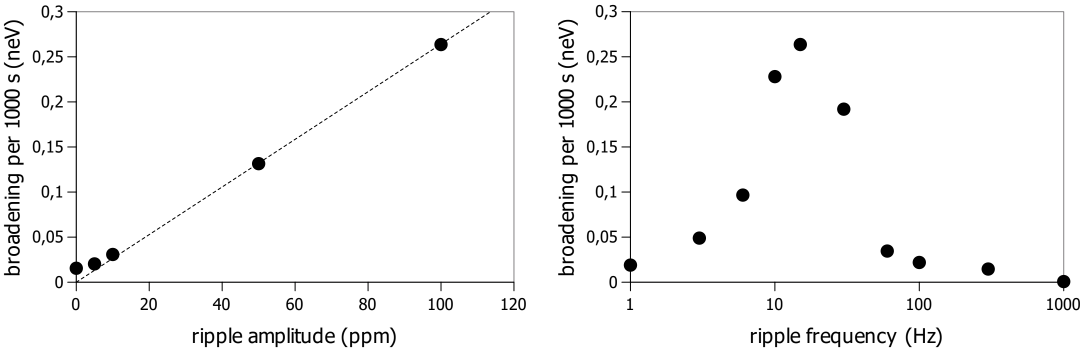

Figure 5.3: Energy broadening during magnetic storage of low-field-seekers in a magnetic field with a ripple frequency of 15 Hz (left) and with a ripple amplitude of 100 ppm (right).

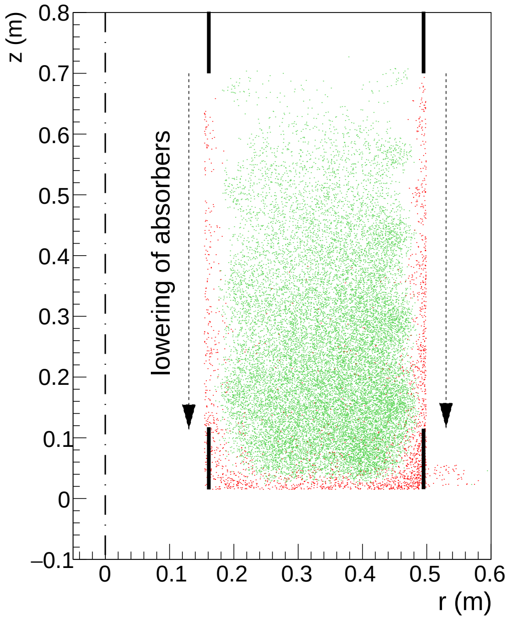

Figure 5.4: Simulated spatial distribution of low-field-seekers (green) and high-field-seekers (red) in the storage volume after ramping. One possibility to remove high-field-seekers is to lower the absorber rings when the magnet is powered.

the magnet with an inductance of 30 H over 1 s, corresponds to a current change in the magnet of 1 mA—about 3.5 ppm of the nominal magnet current. In the simulations, a similar ripple of 10 ppm led to a broadening of less than 0.05 neV over 1000 s. Even during extremely long storage times of 10 000 s, the broadening would stay at an acceptable level of less than 0.5 neV.

For the central current, the requirements are much more relaxed, since it produces a much smaller field. Meichelböck [115] determined that a ripple amplitude of 1 % leads to an acceptable broadening of about 0.2 neV over 1000 s.

5.1.5 High-field-seekers

Any high-field-seekers remaining in the storage volume after ramping accumulate in the high magnetic field at the walls of the storage volume (figure 5.4). The loss rate of high-field-seekers is higher than $10^{-2}\,\mathrm{s}^{-1}$ (figure 5.5), but still small enough to influence measurements with short storage times.

Depolarization at the walls during filling

High-field-seekers can, in part, be removed by pre-polarization, as described in section 3.3. However, subsequent depolarization during reflection of low-field-seekers on guides

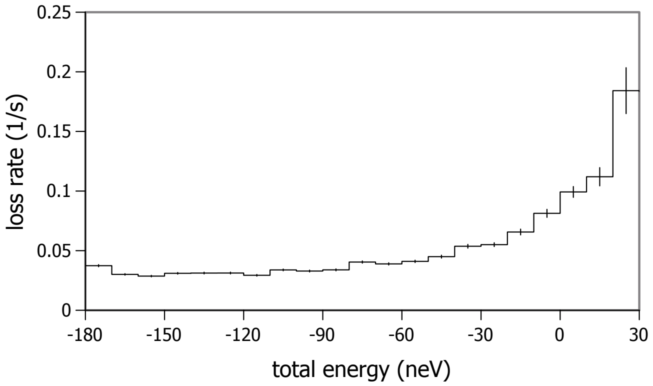

Figure 5.5: Simulated loss rate of high-field-seekers from the storage volume. I assumed an optical potential of (183 + 0.0852i) neV for the storage volume walls.

and storage walls will increase their number again.

Typical UCN-guide materials have depolarization probabilities of 10^{-5} per wall bounce [116–118]. After 200 s of filling and 200 s of cleaning, UCN in the storage volume will have undergone between 1000 and 3000 reflections (figure 5.6). Hence, on average, 2 % of low-field-seekers will have been converted to high-field-seekers and vice versa, and the initial polarization

$$p_\mathrm{i} = \frac{N_\mathrm{lfs} - N_\mathrm{hfs}}{N_\mathrm{lfs} + N_\mathrm{hfs}} \tag{5.4}$$

will be reduced to

$$p_\mathrm{f} = \frac{0.98 N_\mathrm{lfs} + 0.02 N_\mathrm{hfs} - 0.98 N_\mathrm{hfs} - 0.02 N_\mathrm{lfs}}{N_\mathrm{lfs} + N_\mathrm{hfs}} = 0.96 p_\mathrm{i}. \tag{5.5}$$

Depolarization at the walls during ramping

Figure 5.7 shows simulated ratios of the numbers of UCN with increased loss rate—high-field-seekers and marginally trapped low-field-seekers—to the number of magnetically trapped low-field-seekers during ramping and magnetic storage.

Marginally trapped neutrons are removed during the cleaning stage. Only a small ratio of marginally trapped low-field-seekers of 10^{-4} (figure 5.7, *marginally trapped lfs*) is pushed beyond the trapping potential of 115 neV by the increasing magnetic field (figure 5.8).

I assumed initially unpolarized UCN, giving an initial ratio of high-field-seekers to trapped low-field-seekers of 1 (figure 5.7, *high-field-seekers*). This ratio slowly drops once the magnet is powered and can be very efficiently reduced by a factor of 100 to 1000 by lowering an absorber into the volume occupied by high-field-seekers (see section 5.2).

Additional high-field-seekers are produced by depolarization of low-field-seekers during wall bounces. Their ratio initially increases to 10^{-3} but is also quickly decreased by the lowered absorber (figure 5.7, *depolarized lfs*).

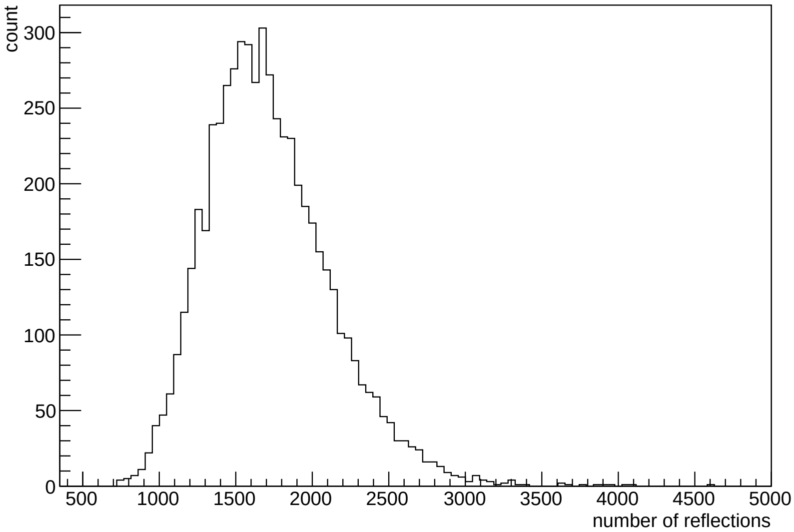

Figure 5.6: Simulated number of reflections that UCN in the storage volume have undergone after 200 s of filling and 200 s of cleaning.

High-field-seekers are accelerated towards the walls of the storage volume and undergo lots of reflections in a high magnetic field. Should they be depolarized during such a reflection they gain a lot of potential energy, which would convert the high-field-seekers into marginally trapped low-field-seekers (figure 5.7, *depolarized hfs*).

The simulations in figure 5.7 show that the ratio of the number of these depolarized high-field-seekers to the number of trapped low-field-seekers can reach 10^{-3} and is not affected by the absorbers. This ratio has to be reduced by at least one order of magnitude by pre-polarization, corresponding to a polarization, p_f, of at least 85 % after cleaning and a pre-polarization, p_i, of at least 90 %.

Wall coating with low depolarization probability

The previous simulations assumed a depolarization probability of 10^{-5} per wall bounce. For stainless steel, preliminary results indicate a much higher depolarization—potentially up to 10^{-3} per bounce [119, 120]. Such a large value would destroy any pre-polarization, produce a large number of marginally trapped UCN—up to 10 % of the number of trapped low-field-seekers—and cause a large shift of the measured neutron lifetime of up to several seconds (section 6.1.3).

Coating the storage walls made of stainless steel with materials with low depolarization probability—like nickel-molybdenum alloys or diamond-like carbon—could reduce those effects. However, the coil formers, which make up large parts of the walls of the storage volume, are individually manufactured and then welded together. This welding would destroy any previous surface treatments and any coating would have to be performed

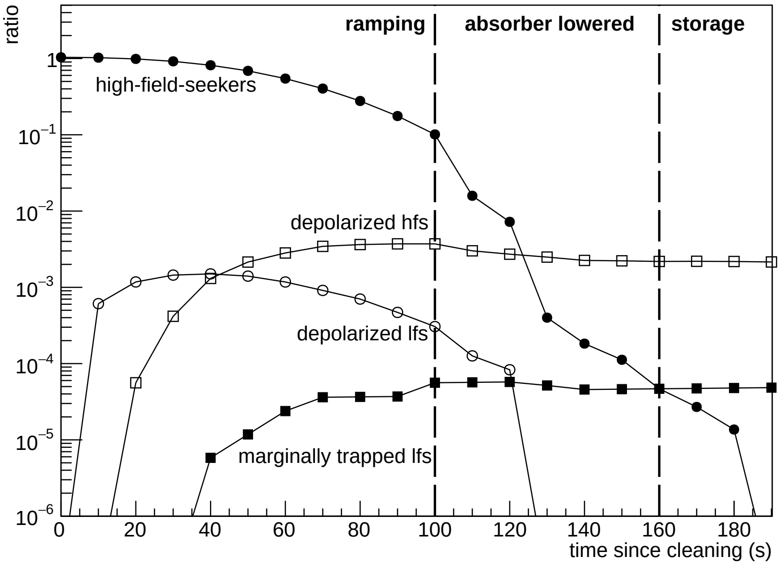

Figure 5.7: Simulated ratio of the numbers of high-field-seekers (circles) and marginally trapped low-field-seekers (squares) to the number of magnetically trapped low-field-seekers during ramping of the magnet and magnetic storage. High-field-seekers and marginally trapped neutrons are initially present in the trap (filled markers) but can also be produced by depolarization (empty markers). A depolarization probability of 10^{-5} per wall bounce and no pre-polarization were assumed.

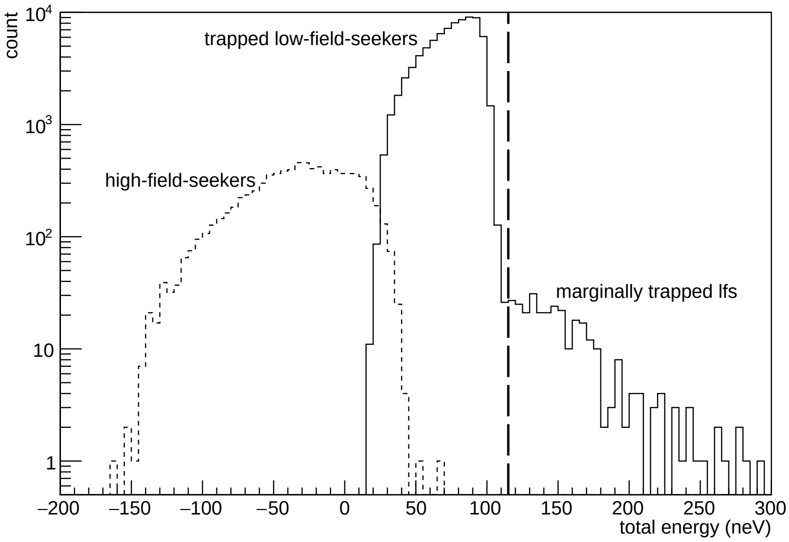

Figure 5.8: Simulated total-energy spectrum of low-field-seekers (solid line) and high-field-seekers (dashed line) in the storage volume right after ramping. The vertical separator indicates the maximum trapping potential for low-field-seekers. A depolarization probability of 10^{-5} per wall bounce and no pre-polarization were assumed.

once the full magnet is assembled.

A promising coating material is nickel phosphorus. Tang et al. [118] recently showed that a NiP film with a thickness of 50 µm directly coated onto stainless steel can reduce the depolarization probability to less than $6.2 \cdot 10^{-6}$ per bounce. The magnetic properties of NiP are dependent on phosphorus concentration. At an atomic concentration above 14 % the Curie temperature of this alloy drops below room temperature, which makes this low depolarization possible. At atomic concentrations above 17 % only weak ferromagnetic behavior is observed, even at a temperature of 4.2 K [121]—possibly making a NiP coating useful for PENeLOPE.

The coating is deposited by immersing the surface in a NiP solution at a temperature of 60 °C for several hours. This moderate temperature poses no danger to the superconductor and epoxy filler and makes coating of the fully assembled magnet possible.

5.2 In-situ polarization with a moving neutron absorber

During ramping, high-field-seekers are spatially separated from the stored low-field-seekers and can be removed by moving an absorber into the space occupied by the high-field-seekers (figure 5.4). If the two rings of neutron-absorbing material on the inner and outer walls of the storage volume—which remove marginally trapped UCN during the cleaning stage—are moved down and up again they serve this purpose. Simulations showed that such moving absorbers can reduce the number of high-field-seekers in the storage volume by a factor of 100 to 1000 within 60 s (figure 5.7).

Such a moving absorber has to fulfill a set of challenging requirements.

- To keep the number of stored UCN constant on the 10^{-4} level, the absorber position during cleaning has to be repeatable within 0.01 mm between each experiment cycle.
- During movement, the absorber must never reach into the volume where low-field-seekers are stored and always stay within the contours shown in figure 5.9. Thermal contraction of both the absorbers and the walls of the storage volume have to be taken into account.
- It should move down from a height of about 0.8 m, stay lowered for at least 20 s, and move up again to a height of about 1 m, all within 60 s.
- The absorber and actuation mechanism have to be compatible with a 10^{-8} mbar-vacuum environment.
- The absorber has to be non-magnetic and has to have low electric conductivity to avoid eddy currents.

5.2.1 Absorber actuation

The two absorbers will be hanging from the experimental lid of PENeLOPE, each with three supporting rods. The rods are fed through the lid into membrane bellows and

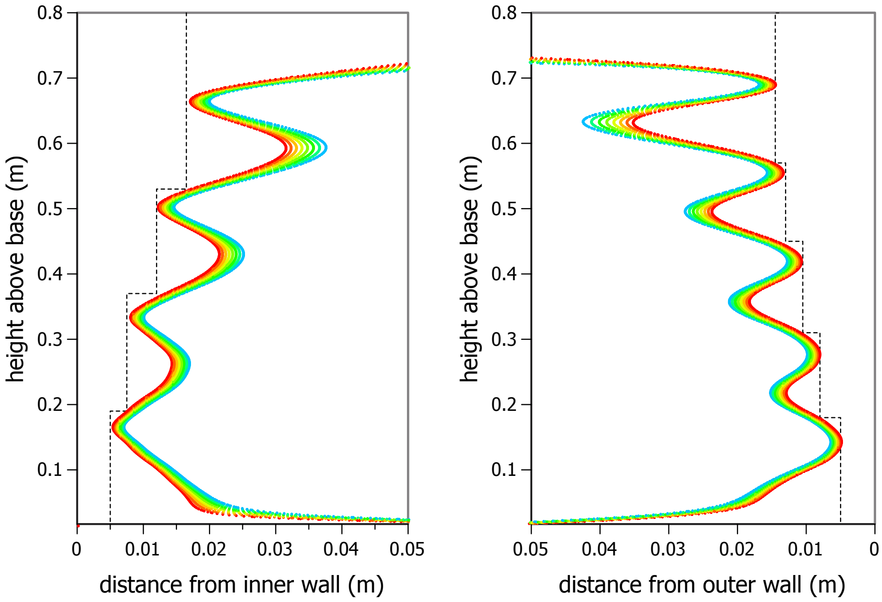

Figure 5.9: Distance of the equipotential lines of the storage potential, between 110 neV (blue) and 118 neV (red), from the inner and outer walls. The dashed lines indicate the clearance the absorber is allowed to move into.

connected to the upper bellow flanges. These flanges can be moved up and down by six *Bosch Rexroth MKK* linear actuators [122], compressing or stretching the membrane bellow in the process.

The membrane bellows can be stretched between a length of 304.6 mm and 1305.4 mm [123] and the linear actuators have a travel range of 1100 mm, giving the absorber rings a vertical movement range of 1000 mm. The bellow flanges are sealed with CF gaskets, making them ultra-high-vacuum compatible. As long as they are supported by a central rod with a diameter of 36 mm to 38 mm, they can also withstand the maximum internal pressures of up to 6 bar in case of a failure of the vacuum vessel [124].

Absorber control

The linear actuators are controlled by six *Bosch Rexroth IndraDrive CS* inverters [125]. A wide range of parameters—e.g. position limits, speed limits, acceleration limits, transmission intervals, and control modes—can be configured via the *IndraDrive* software [126]. The actuator movement can be controlled over several real-time communication protocols, e.g. SERCOS III or EtherCAT.

The National Instruments CompactRIO system, which was considered as a slow-control system for PENeLOPE, has only rudimentary EtherCAT support for a simple position-controlled operation mode. In this mode the actuator follows periodically transmitted target positions and the complete positioning profile for the absorber movement had to be programmed into the CompactRIO system using LabVIEW.

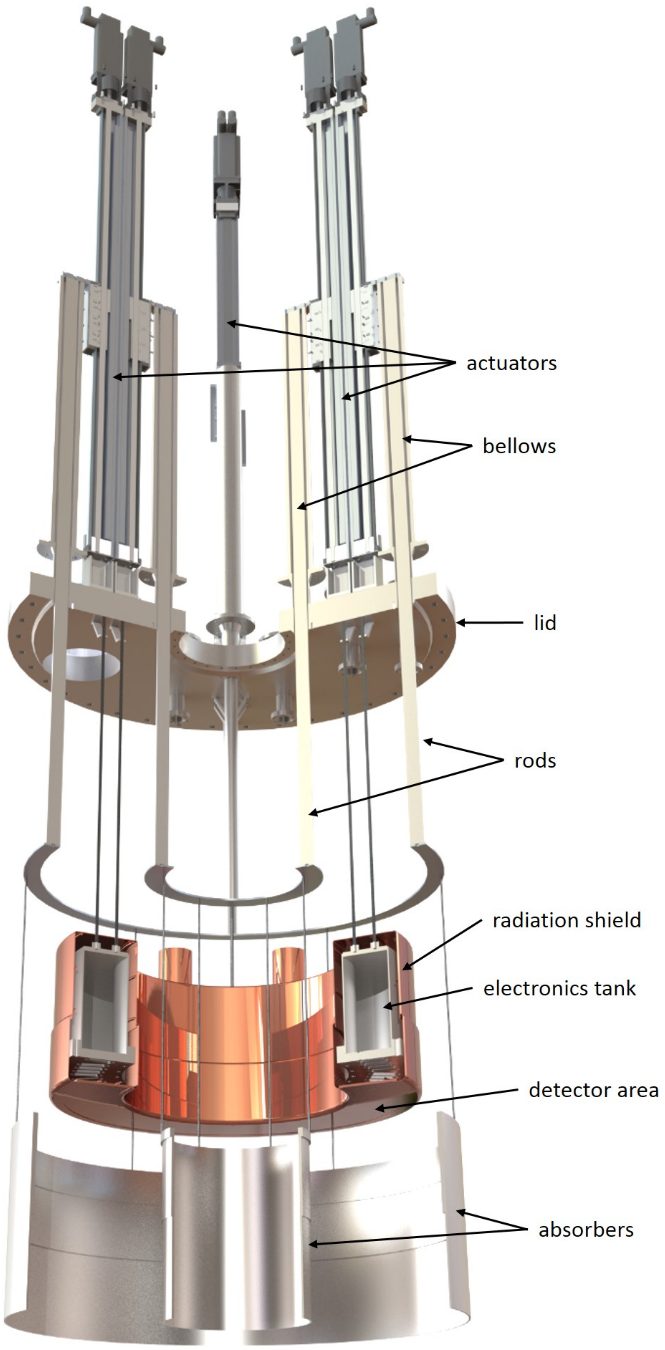

Figure 5.10: Rendering of the lid of PENeLOPE's storage volume with the absorber-actuation mechanism (top), tank for the proton-detector electronics (center), and absorber rings (bottom). The absorber rings are lowered halfway into the storage volume.

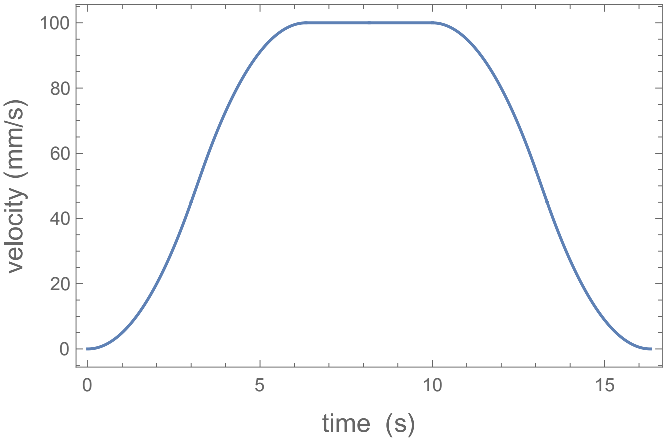

Figure 5.11: Velocity profile of an actuator movement with a jerk of 10 mm s^{-3}, a target acceleration of 30 mm s^{-2}, and a target velocity of 100 mm s^{-1}. The total traveled distance is 1000 mm.

The movement between a starting and end position is calculated from a given target speed, acceleration, and jerk[2]. Starting from standstill, the acceleration is increased with a constant jerk until the target acceleration is reached. The actuator further accelerates with this constant acceleration until it has almost reached the target speed, at which point the acceleration is again reduced smoothly to zero with a constant negative jerk. The movement continues with the target speed until half of the distance between start and end position has been traversed. Then the whole process happens in reverse and the actuator comes to a stop precisely at the target position (figure 5.11).

Position reproducibility tests

We did several tests with a single linear actuator to test its position reproducibility. We fixed a *MICRO-EPSILON mainSENSOR MDS-45* inductive distance sensor [127] to the actuator's support structure and attached the sensor's magnetic counterpart to the bottom end of the bellow's support rod. The rod was then repeatedly moved up to a random position and moved down again to a fixed target position. The actual end position was precisely measured with the distance sensor, which produces a voltage proportional to the distance between sensor and magnetic counterpart. This voltage was averaged over 10 s giving a very precise position measurement. This process was repeated about two thousand times and the resulting end-position distribution had a standard deviation of 3.6 µm, well within the required 10 µm accuracy (figure 5.12).

Additionally, Schuldt [64] studied the positioning accuracy after anomalous operation of the actuator—like power loss or external forces while the actuator was not powered. The linear actuators apply a brake when not powered, preventing it from moving, and keeping the difference of positions before and after those tests below 10 µm.

---

[2] Jerk is the time derivative of acceleration.

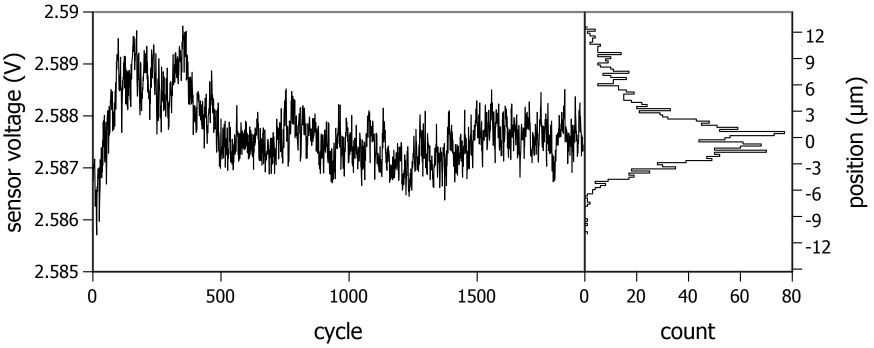

Figure 5.12: Relative end positions of the absorber actuator (left) and their distribution (right) during two thousand movements up to a random position and back down to the target position.

A major uncertainty in absorber position is thermal contraction of the linear actuator and the support rods. In PENeLOPE, the rods will be subject to a gradient from the top at room temperature to the walls of the storage volume at 4.2 K. Depending on their temperature profile they might contract by up to several millimeters. Since the rods move up and down between cold walls, the rods' temperature profiles might slowly change over time. The walls themselves also might change their temperature profile when liquid-helium levels change. To achieve the required precision in absorber positioning the temperature profile of at least one rod should be monitored to correct for varying thermal contraction.

5.2.2 Absorber construction

With the full set of six actuators and six membrane bellows later used in PENeLOPE, we built a test bench that can be used to test different absorber constructions (figure 5.13). The actuators can be individually or synchronously moved over the full range of 1 m with a LabVIEW program. An outer and inner cylinder of aluminium sheets rolled to the approximate radius of the storage volume resemble its walls.

We built a first prototype of the outer absorber using three 0.5 mm-thin aluminium sheets, rolled into a curvature with a radius of 500 mm and each spanning a little less than a third of the circumference of the outer walls of the storage volume [64]. They are connected with three low-profile, spring-loaded pins each (figure 5.14). These ensure that the sheets are pressed onto the wall, even during thermal contraction. The sheets are 400 mm high, which leaves up to 10 mm of radial clearance at the top (figure 5.9) for attachment points and a potential stiffening ring.

We constructed the inner absorber from two aluminium sheets with the same height, rolled to a radius of 160 mm and pulled together by springs (figure 5.14).

Neutron-absorbing material, e.g. polyethylene or titanium, can be glued or deposited onto the surface of the absorbers.

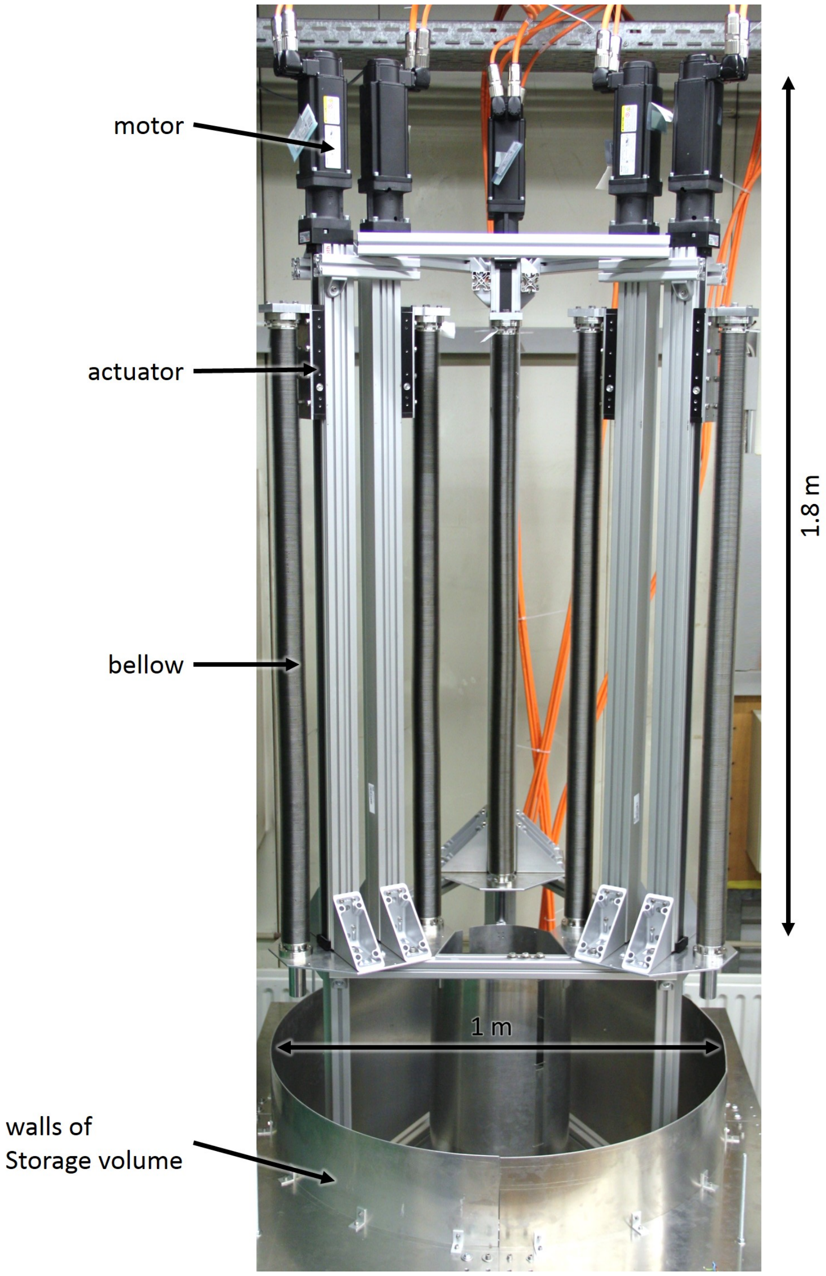

Figure 5.13: Absorber test bench with all six actuators and an approximate model of PENeLOPE's storage volume built from rolled aluminium sheets.

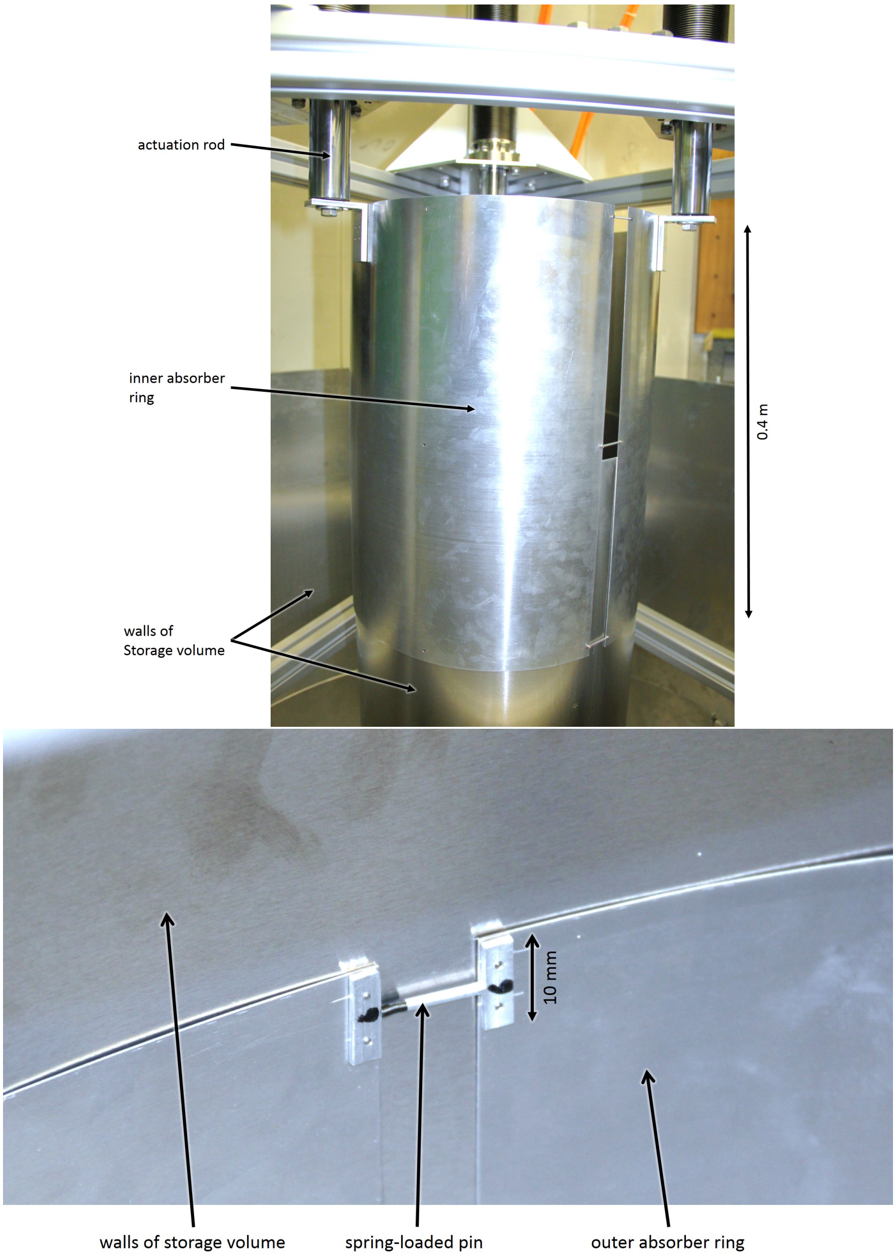

Figure 5.14: Prototype of the inner absorber (top) and one of the spring-loaded pins between segments of the outer absorber (bottom).

The construction described above is quite fragile. The spring-loaded pins are easily bent or broken. The radius of the rolled sheets cannot be precisely controlled, leaving gaps of several millimeters between sheets and walls, and the springs do not exert sufficient pressure to force the sheets into the correct shape. This might be improved by more careful rolling and possibly a precisely machined stiffening ring at the upper edge of the absorber. However, the construction can adapt quite well to slight changes in circumference due to thermal contraction or imprecise cutting of the aluminium sheets.

A single, massive ring might also be considered. However, its thermal contraction would have to be precisely controlled to prevent it from jamming or reaching into the storage volume.

An open question that has not been addressed yet are eddy currents induced during movement of the absorber. They could lead to sizable forces on the fragile ring. Manufacturing the absorber itself from material with low electrical conductivity might be necessary. Titanium, a neutron-absorbing material, might be a viable candidate.

5.2.3 Other uses for a moving platform

A moving platform as described could not only move up and down an absorber but could also be useful for other purposes.

Systematic studies During the initial filling and cleaning phase the absorber stays at a fixed height to remove UCN above a certain energy threshold. The moving absorber allows to adjust this threshold for every filling and cleaning stage individually. This could be used to vary the number of marginally trapped neutrons and estimate their effect on the lifetime measurement.

A different construction—an absorber that moves down in the center of the storage volume instead of close to the walls—could remove stored low-field-seekers instead of high-field-seekers. Such a measurement could help to determine the number and loss rate of high-field-seekers in the trap.

Magnetic-field mapping The winding scheme of the superconducting coils and mistakes during manufacturing introduced several irregularities into the coils—thickening at the wire entries and exits [45], incorrectly arranged windings, and even missing windings.

These changes were all deemed uncritical in the simulation model. However, precise mapping of the magnetic field might be needed to confirm this. The absorber actuators could be used to precisely move a platform carrying an array of magnetic-field sensors through the storage volume.

Wall coating Many neutron-reflecting and lowly depolarizing wall coatings—e.g. diamond-like carbon and nickel-molybdenum—are produced with chemical vapor deposition. To coat large substrates, a sputtering head has to be moved across the surface of the substrate.

With sputtering heads mounted onto the actuators, the storage volume walls could be coated in a similar fashion.

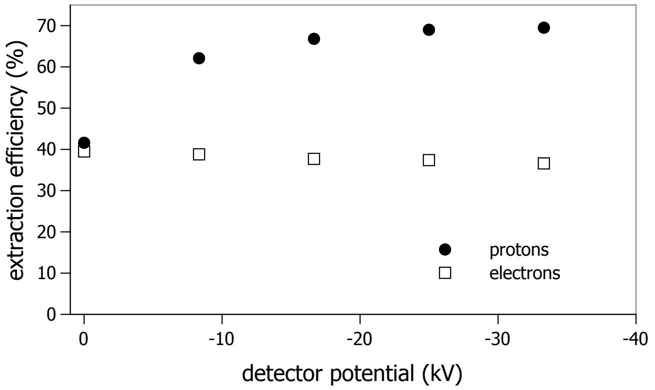

Figure 5.15: Simulated efficiency of proton and electron extraction from magnetically trapped low-field-seekers with a total-energy spectrum shown in figure 5.8.

Moving UCN detector Göltl et al. [128] and Salvat et al. [34] developed compact detectors that can be inserted into storage bottles for UCN. A similar detector could be attached to the absorber actuators and determine the spatial distribution of UCN in PENeLOPE's storage volume.

5.3 Counting protons

Thanks to PENeLOPE's combination of magnetic and gravitational trapping, the top of the trap does not have to be closed by additional magnet coils. Instead, a detector for neutron-decay products—protons and electrons—can be placed above the storage volume.

Charged particles gyrate along magnetic-field lines and can be reflected by magnetic-field gradients due to the so-called magnetic-mirror effect. Although the decay particles are emitted almost isotropically by the decaying neutrons, these effects can be used to guide them to the top of the trap. The large magnetic-field gradients at the walls reflect most protons and electrons emitted downwards. By adding more windings to every other outer coil of the superconducting magnet, we achieved a vertical alignment of field lines in the storage volume (figure 1.7), which guide the particles towards the detector. About 40 % of protons and electrons from beta decays of stored low-field-seekers can be extracted onto the detector this way.

A large fraction of the particles not able to reach the detector are reflected by the slightly increasing magnetic field towards the detector. To increase the number of particles that can overcome this magnetic mirror, we can apply a post-acceleration voltage to the detector. The beta-decay electrons, with energies up to 782 keV, would require several hundred kilovolts to appreciably improve extraction efficiency. However, the extraction efficiency of beta-decay protons, with energies less than 0.75 keV, can be increased to over 70 % with a more feasible acceleration potential of $-25\,\mathrm{kV}$ (figure 5.15). Additionally, the resulting energy boost makes the detection of protons easier.

A detector for these protons should

- efficiently detect protons with energies of 25 keV,
- operate at a temperature of 77 K to reduce radiative heat transfer to the superconducting magnet,
- operate in a strong magnetic field of up to 0.5 T,
- be compatible with a very low vacuum pressure of less than 10^{-8} mbar, and
- cover a large area of $0.23\,\mathrm{m}^2$.

Several detectors were considered [82, 129–133] until Tietze [134] showed that Large-Area Avalanche Photo Diodes (APDs) can fulfill these challenging requirements and detect protons with 5 keV at a temperature of 77 K with large signal-to-noise ratio.

5.3.1 Detector concept

Due to the small size of APDs—9 mm × 18 mm—we will need up to 1400 of them to cover the detector area [135]. To measure their signals, two electrical connections each—2800 in total—have to be fed through PENeLOPE's vacuum vessel to the front-end electronics. Since the APDs are placed on a high electric potential, the vacuum feed-throughs would have to be insulated against high voltage. To avoid the large number of high-voltage-insulated feed-throughs, we chose to develop custom front-end electronics that can themselves be set on a high electric potential inside the cryostat and transfer all detector data via a single, electrically insulating optical fiber [136, 137]. This design also has the advantage of keeping the cables carrying small electrical signals between APDs and front-end electronics very short, reducing susceptibility to noise. To avoid the complications of operating the electronics at low temperatures and in high vacuum we are designing the electronics compact enough to fit into a pressurized, electrically insulated, and thermally insulated tank (figure 5.16).

Since the tank itself will be placed on the same electrical potential as the APDs, it will require only low-voltage feed-throughs to connect APDs to the front-end electronics. However, the tank should have sufficient clearance from the walls of the storage volume to avoid electrical discharges between the tank surface and the walls or the absorber.

To reduce heat transfer to the cold magnet the tank will be housed in a radiation shield cooled by liquid nitrogen. This will lead to large radiative heat loss from the tank to the shield—about $450\,\mathrm{W\,m^{-2}}$. The low-power electronics, consuming less than 100 W, are not able to compensate this heat loss and the tank would cool down. To avoid condensation of moisture, heating should be foreseen—e.g. by circulating air or water through the tank. Electrical heaters are less suitable, as they would have to be set on a high electrical potential, too, and would require special power supplies with insulating transformers rated for high voltages.

The radiation shield has to be assembled from several parts. The upper shield is attached to the lid and and the electronics tank is slid into the upper shield. The

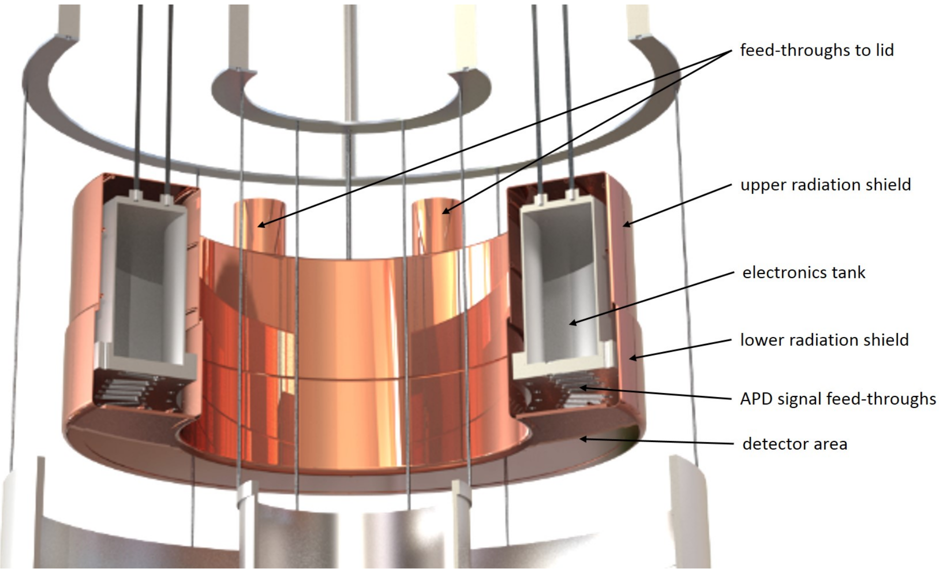

Figure 5.16: Rendering of the tank housing the proton-detector electronics, with feed-throughs and radiation shield.

detector area with APDs is attached to the electronics tank and the liquid-nitrogen cooling channels of upper shield and detector area are connected. The shields should have a smooth, polished surface and should be manufactured without seams—e.g. by deep-drawing—to avoid electrical discharges. Since the liquid-nitrogen cooling channels also have to be attached on the inside of the shield, the upper shield does not cover the whole height of the electronics tank to still allow us to connect the cooling channels of upper shield and detector area. Finally, the gap between upper shield and detector area is closed by two annular pieces, which are passively cooled via heat conduction.

The vacuum seals of the tank have to be high-vacuum compatible but should not require massive flanges so clearance to the walls of the storage volume is not reduced. An indium seal—as already used on the helium tank of CoTEx—might be suitable, as it requires a very low sealing force of $500\,\mathrm{N\,cm^{-1}}$ and can provide leak rates below $2 \cdot 10^{-10}\,\mathrm{mbar\,l\,s^{-1}}$ [138].

All these challenges—high-voltage clearance, heat transfer, and heat loss—can be mitigated by reducing the size of the tank. Hence, miniaturizing the detector electronics should be one of the main goals of their design.

5.3.2 Optimized Avalanche Photo Diode arrangement

To maximize the detection efficiency of extracted protons I simulated protons from decays of stored low-field-seekers with the detector area positioned 0.85 m above the bottom coils. The current design of the radiation shield limits the positions of APDs to a radial range of 0.27 m to 0.39 m. The protons mostly hit the lower half of this range and the APDs should be concentrated towards the inner radius (figure 5.17).

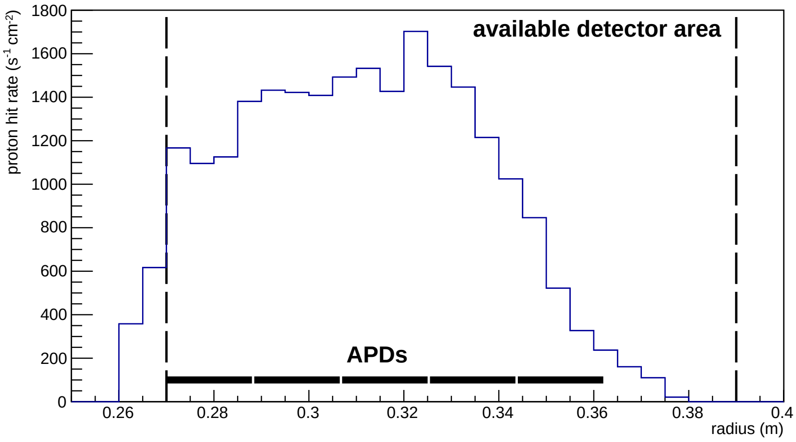

Figure 5.17: Simulated radial distribution of protons—extracted from magnetically trapped low-field-seekers—hitting the detector area and potential arrangement of APDs.

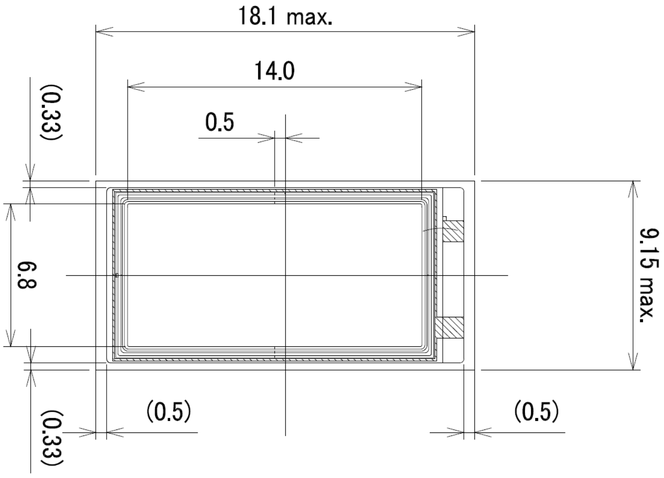

Figure 5.18: Outline of a Hamamatsu type-S11048 silicon APD. Dimensions are given in millimeters. [135]

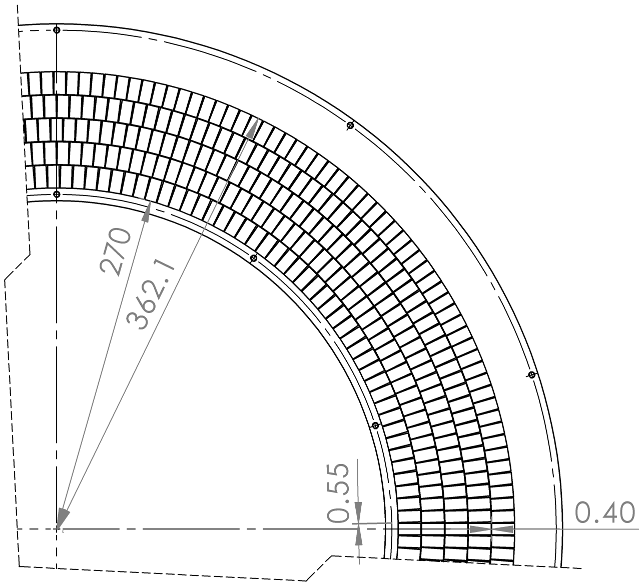

Figure 5.19: Segment of the detector area with possible arrangement of APDs.

The APDs are housed in ceramic frames with a size of 9.15 mm by 18.1 mm. Good coverage is achieved with five circular APD arrangements (figure 5.19) with 175, 190, 200, 210, and 225 APDs—a total of 1000 APDs. The active area of an APD is 6.8 mm by 14 mm—57.5 % of its total size (figure 5.18). With the full set of 1000 APDs, we can cover about 41 % of the total detector area with active surfaces and detect 47 % of extracted protons.

At the moment, only 400 APDs are available. With this subset we can fill the second- and third-innermost circle, cover 17 % of the total detector area with active surfaces, and detect 23 % of extracted protons.

5.3.3 Potential systematic effects on the neutron-lifetime measurement

Varying spatial distribution of neutrons

The probability to extract a beta-decay proton from the storage volume is highly position-dependent (figure 5.20). If the spatial distribution of UCN in the storage volume varies over time, the extraction efficiency would vary, too, causing a systematic effect on the neutron-lifetime measurement. This effect is especially important in magnetic traps that are filled with neutrons without an initial cleaning stage, e.g. UCNτ [34]. UCN entering the magnetic trap initially fill only a small part of the available phase space and their trajectories are randomized very slowly, leading to slowly changing spatial distribution. Additionally, marginally trapped neutrons can end up in quasi-stable orbits and reach absorbers only after long storage times.

In PENeLOPE, diffuse reflections of UCN during the filling and cleaning stages very rapidly randomize the trajectories of the UCN and the absorbers can remove marginally trapped neutrons very quickly. Hence, these effects should not play a role in PENeLOPE.

The proton-extraction efficiency from high-field-seekers is reduced to 10 % because they are accumulated at the walls. This should reduce the effect of their increased loss rate on the neutron-lifetime measurement obtained from the proton detector.

Varying mean free path of protons

The mean free path of protons in PENeLOPE's storage volume depends on the pressure of the rest gas—predominantly hydrogen. A varying vacuum pressure also varies the probability that a proton is absorbed by a rest-gas atom and influences the neutron-lifetime measurement.

According to Bröcker [139] and Tabata and Shirai [140], we can estimate an upper limit for the total cross section, σ_H, of protons with energies between 0.1 keV and 20 keV interacting with hydrogen, of $1 \cdot 10^{-15}\,\mathrm{cm}^2$. The free-path length, l, in a gas with pressure p and temperature T is given by

$$l = \frac{k_\mathrm{B} T}{p \sigma_\mathrm{H}} \tag{5.6}$$

and the probability of a proton interacting with the rest gas along a path with length d is $1 - \exp(-d/l)$. Protons reaching the detector have trajectories with different lengths (figure 5.21). To calculate the total reduction in the proton rate on the detector, one has to integrate the interaction probability weighted with the path-length distribution P_l:

$$P_\mathrm{tot} = \int \left[1 - \exp\left(-\frac{d}{l}\right)\right] P_\mathrm{l} \mathrm{d}l. \tag{5.7}$$

The relative variation of the proton rate on the detector due to a small variation of vacuum pressure, Δp, is then given by the derivative of P_tot with respect to the pressure. To achieve the aspired precision, the proton rate has to be kept stable on a relative level of

$$\Delta p \frac{\partial P_\mathrm{tot}}{\partial p} < 10^{-4}. \tag{5.8}$$

Given the path-length distribution in figure 5.21, assuming cold rest gas with a temperature of 4.2 K, and assuming the worst case that every proton that interacts cannot be detected anymore, the vacuum pressure of 10^{-8} mbar has to be kept stable on a level of $0.05 \cdot 10^{-8}$ mbar. This is just in reach of typical vacuum-pressure sensors, specified with a repeatability of 5 % at a pressure of 10^{-8} mbar [104].

Varying detection efficiency

Any change of detection efficiency over time could have a systematic effect on the neutron-lifetime measurement. Detection efficiency could be changed by

- increase of proton absorption in a dead layer on the APD, e.g. adsorbed rest gas;
- changes in gain and dark current in the APDs; and

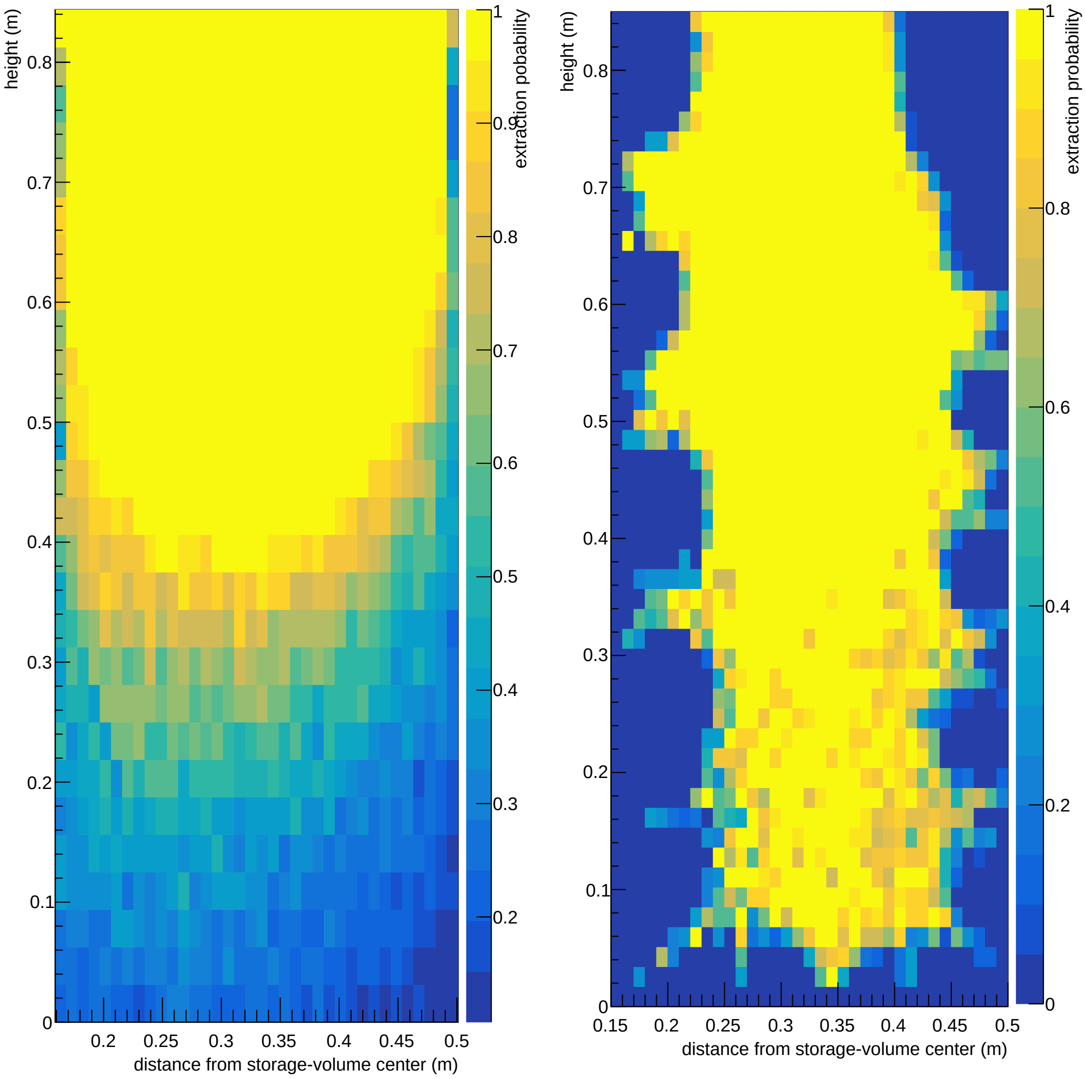

Figure 5.20: Simulated probability to extract a beta-decay proton from the storage volume during filling or cleaning (left) and magnetic storage (right).

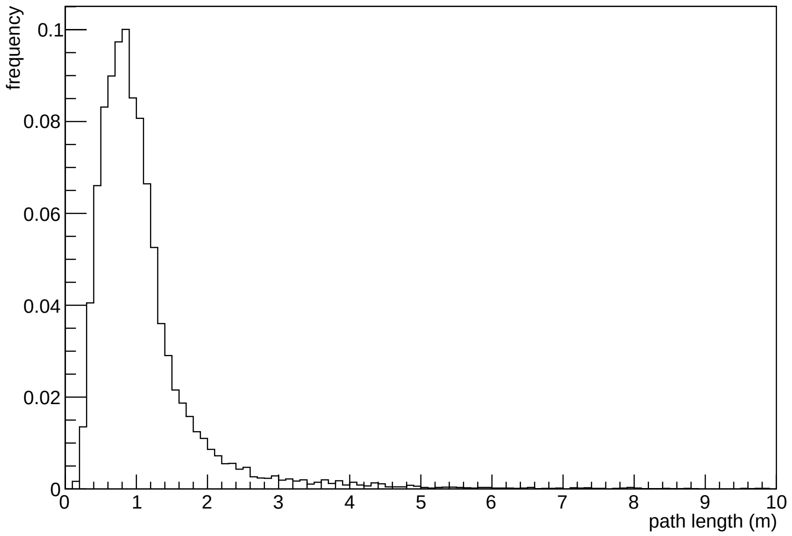

Figure 5.21: Simulated path lengths of protons reaching the detector.

- changes in electronic amplification and noise.

These effects can be monitored by mounting a calibration LED below the proton detector, which regularly emits a light pulse. Any changes in detected pulse height can indicate changes in detection efficiency. However, variation in LED brightness itself have to be ruled out

Noise levels can be monitored by recording the APD signal at random times using a random trigger. Special attention has to be paid to achieve a truly random trigger period that is not interrupted or delayed by other trigger events, ideally using a hardware random-number generator.

Detector dead time

Most particle detectors cannot resolve events that happen in rapid succession within a dead time, τ_d. If the detected events are considered a Poisson process with an average rate, λ, the probability of two events happening within the dead time is

$$P(\Delta t < \tau_\mathrm{d}) = 1 - \exp(-\lambda\tau_\mathrm{d}) \tag{5.9}$$

and the rate measured by the detector, λ', is reduced by this probability [141, chap. 5.7]:

$$\lambda' = \exp(-\lambda\tau_\mathrm{d})\lambda. \tag{5.10}$$

The result is a rate-dependent detection efficiency. During magnetic storage, the event rate—given by the number of initially stored UCN multiplied by the probability to extract and detect a proton, $\epsilon_\mathrm{p}N_0$, and the background rate, b_p—is falling over time:

$$\lambda = \frac{\epsilon_\mathrm{p}N_0}{\tau_\mathrm{n}} \exp\left(-\frac{t}{\tau_\mathrm{n}}\right) + b_\mathrm{p}. \tag{5.11}$$

The result is an increasing detection efficiency over time, which—if not corrected—would cause an increase in measured neutron lifetime.

In PENeLOPE, we expect an initial proton rate of about $4000\,\mathrm{s}^{-1}$ in all 400 channels. During development of the front-end electronics Steffen [136] estimated a dead time of 10 µs for an individual channel. The effective dead time is the dead time of one channel divided by the number of channels, i.e. $\tau_\mathrm{d} = 25\,\mathrm{ns}$. With these values one can estimate the maximum rate-reduction factor as

$$1 - \exp\left(-\lambda\tau_\mathrm{d}\right) = 10^{-4}, \tag{5.12}$$

which could result in a potentially significant effect on the neutron-lifetime measurement (section 6.1.3).

Clock drift

A drift in the proton-detector clock could shorten or prolong the measured neutron lifetime. The clock should be tightly synchronized with a reference clock with an offset and stability of less than 10^{-4}—a value routinely achieved by temperature-compensated quartz oscillators.

6 Stage VI: Counting neutrons

A UCN detector mounted below PENeLOPE (figure 6.1) counts the neutrons entering it during the whole experimental cycle (figure 6.2). When the source valve is opened for filling, leakage through the UCN switch quickly increases to a constant rate of UCN entering the detector. After filling, the storage and source valves close, the UCN switch moves in a middle position, UCN remaining in the guide are dumped into the detector, and the rate goes down again very quickly. After ramping, the UCN switch moves into a position that guides UCN from PENeLOPE's storage volume into the detector, the storage valve opens again, and a small number of UCN trapped in the feeder can enter the detector. Once the UCN have been magnetically stored for a certain time the magnet is powered down, trapped low-field-seekers can leave the trap and are counted in the detector.

If we repeat this experimental cycle for different storage times we can determine the neutron lifetime from the respective numbers of surviving neutrons (figure 6.3, left).

Additionally, for each storage cycle, we can directly determine the exponential decay of neutron-decay rate from the proton rate observed by the proton detector (figure 6.3, right).

Using a suitable analysis scheme we can combine these two measurements of neutron lifetime and improve the accuracy and precision compared to the individual measurements.

6.1 Bayesian analysis scheme for PENeLOPE

To estimate the achievable precision and the influence of systematic effects, I worked out a Bayesian analysis scheme for PENeLOPE. Bayes' theorem states that the posterior probability, P_{post}, of parameters $\vec{x}$—given measured data D—is proportional to the likelihood, $\mathcal{L}$, of measuring the data—if the parameter set $\vec{x}$ were the correct one—multiplied by the prior probability of the parameters, P_{prior}:

$$P_{\mathrm{post}}\left(\vec{x}|D\right) \propto \mathcal{L}\left(D|\vec{x}\right) P_{\mathrm{prior}}\left(\vec{x}\right). \tag{6.1}$$

Depending on the number of parameters, these distributions can become very difficult to handle analytically; instead I used the Bayesian Analysis Toolkit (BAT) [68] to calculate the posterior-probability distributions. BAT performs a Markov-chain importance sampling of the product of prior-probability and likelihood distributions over the whole parameter range and provides an estimate of the posterior-probability distributions of all parameters.

For PENeLOPE, the likelihood to measure a number of neutrons, N_{n}, after a certain magnetic storage time, T, depends on the neutron lifetime, τ_{n}, the number of initially

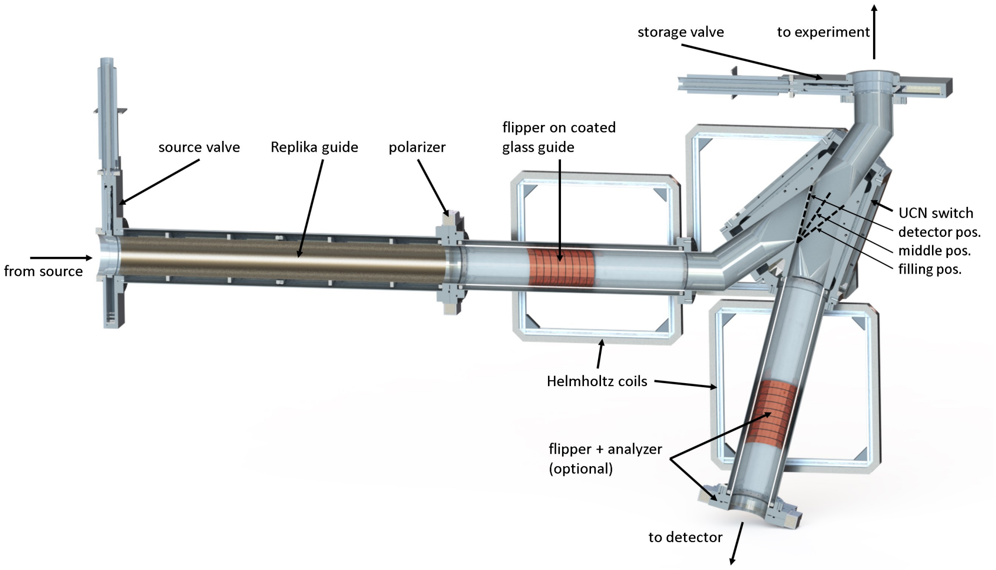

Figure 6.1: Cut through UCN guides, valves, and polarizers below PENeLOPE's cryostat.

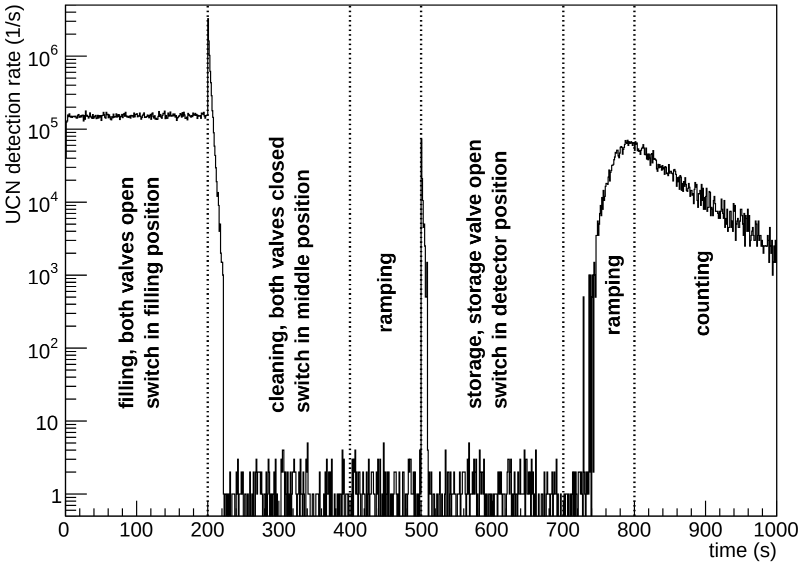

Figure 6.2: Simulated rate of neutrons detected in the UCN detector during a complete experimental cycle with a magnetic storage time of 200 s. The rate is scaled to the expected UCN source intensity. Random noise with an average rate of one count per second was added afterwards.

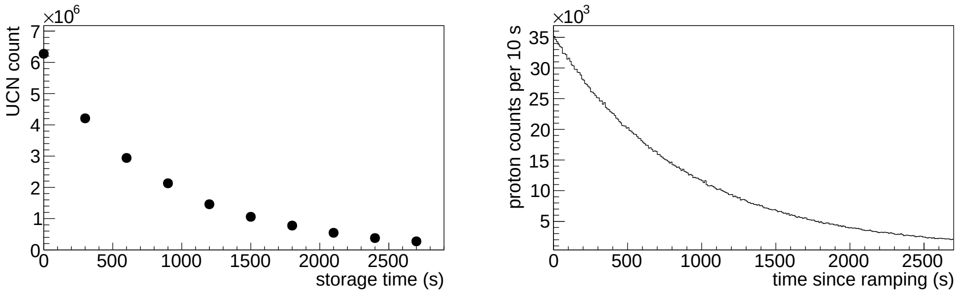

Figure 6.3: Number of detected neutrons after several experimental cycles with different storage times (left) and rate of detected protons during a single magnetic storage phase (right).

stored neutrons multiplied with the probability to extract the remaining neutrons from the storage volume and detect them in the UCN detector, $\epsilon_\mathrm{n} N_0$, and the neutron detector background rate, b_n, during the measurement time, T_n:

$$\mathcal{L}_\mathrm{n}\left(N_\mathrm{n} | \tau_\mathrm{n}, \epsilon_\mathrm{n} N_0, b_\mathrm{n}\right) = P_\mathrm{Poisson}\left[N_\mathrm{n} | \epsilon_\mathrm{n} N_0 \exp\left(-\frac{T}{\tau_\mathrm{n}}\right) + b_\mathrm{n} T_\mathrm{n}\right]. \tag{6.2}$$

The likelihood to detect a number of protons, $N_{\mathrm{p},i}$, in a time interval, $t_{i+1} - t_i$, during magnetic storage depends on the apparent proton rate, λ'—given by equations (5.10) and (5.11) with the proton detector dead time, τ_d— the neutron lifetime, the number of initially stored neutrons multiplied with the probability to extract and detect protons, $\epsilon_\mathrm{p} N_0$, and the proton detector background rate, b_p:

$$\begin{aligned} \mathcal{L}_{\mathrm{p},i}\left(N_{\mathrm{p},i} | \tau_\mathrm{n}, \epsilon_\mathrm{p} N_0, b_\mathrm{p}\right) &= P_\mathrm{Poisson}\left(N_{\mathrm{p},i} | \int_{t_i}^{t_{i+1}} \lambda' \mathrm{d}t\right) \\ = P_\mathrm{Poisson}\left[N_{\mathrm{p},i} | \int_{t_i}^{t_{i+1}} \left(\frac{\epsilon_\mathrm{p} N_0}{\tau_\mathrm{n}} e^{-\frac{t}{\tau_\mathrm{n}}} + b_\mathrm{p}\right) \right. & \left. \exp\left(-\tau_\mathrm{d}\left(\frac{\epsilon_\mathrm{p} N_0}{\tau_\mathrm{n}} e^{-\frac{t}{\tau_\mathrm{n}}} + b_\mathrm{p}\right)\right) \mathrm{d}t\right] \end{aligned} \tag{6.3}$$

The total likelihood of measuring one exponentially decaying proton-rate curve during a single measurement cycle is the product of the likelihoods in each time bin of this curve:

$$\mathcal{L}_\mathrm{p} = \prod_i \mathcal{L}_{\mathrm{p},i}. \tag{6.4}$$

As described in chapter 3.4, after filling we can dump the UCN remaining in the guides between source valve and storage valve into the UCN detector to estimate the initial number of stored neutrons. The likelihood to detect a number, N_m, of these dumped neutrons should then directly depend on the number of UCN filled into the storage volume multiplied with a constant factor, $\epsilon_\mathrm{m} N_0$, and the neutron detector background rate during the measurement time T_m:

$$\mathcal{L}_\mathrm{m}\left(N_\mathrm{m} | N_0, \epsilon_\mathrm{m}, b_\mathrm{n}\right) = P_\mathrm{Poisson}\left(N_\mathrm{m} | \epsilon_\mathrm{m} N_0 + b_\mathrm{n} T_\mathrm{m}\right). \tag{6.5}$$

Background rates can be similarly estimated by background measurements performed after each cycle. The likelihood of measuring a number of background counts, B_n and B_p, with the neutron and proton detectors during a background measurement time, T_b, is

$$\mathcal{L}_\mathrm{bn}\left(B_\mathrm{n}|b_\mathrm{n}\right) = P_\mathrm{Poisson}\left(B_\mathrm{n}|b_\mathrm{n}T_\mathrm{b}\right) \tag{6.6}$$

$$\mathcal{L}_\mathrm{bp}\left(B_\mathrm{p}|b_\mathrm{p}\right) = P_\mathrm{Poisson}\left(B_\mathrm{p}|b_\mathrm{p}T_\mathrm{b}\right). \tag{6.7}$$

The total likelihood for a set of measurement cycles—each with storage time T_j, number of initially stored UCN $N_{0,j}$, and background rates $b_{\mathrm{n},j}$, $b_{\mathrm{p},j}$—is the product of the likelihoods of each single cycle. To study effects on precision and accuracy more detailed we can do three separate analyses. One analysis using only neutrons—where the initial number is estimated from the dumped-neutron count and the lifetime from the number of remaining neutrons—with a total likelihood

$$\mathcal{L}_\mathrm{n-only} = \prod_j \mathcal{L}_\mathrm{n}\mathcal{L}_\mathrm{m}\mathcal{L}_\mathrm{bn}. \tag{6.8}$$

One analysis using only protons with a total likelihood

$$\mathcal{L}_\mathrm{p-only} = \prod_j \mathcal{L}_\mathrm{p}\mathcal{L}_\mathrm{bp}. \tag{6.9}$$

And a combined analysis—where the number of initially stored UCN is estimated from the proton rate without the need for the estimation from the dumped-neutron count—with a total likelihood

$$\mathcal{L} = \prod_j \mathcal{L}_\mathrm{n}\mathcal{L}_\mathrm{p}\mathcal{L}_\mathrm{bn}\mathcal{L}_\mathrm{bp}. \tag{6.10}$$

For the neutron lifetime I assumed a flat prior-probability distribution from 860 s to 900 s. For the initial number of stored neutrons I assumed a broad, flat prior from 10^5 to 10^8. For the background rates I assumed flat priors between zero and double the values in table 6.1.

The analysis could be further improved by using narrower prior-probability distributions. Olive [22] gives a distribution determined from the most precise neutron-lifetime measurements so far, which could be used as a prior for the neutron lifetime. The distributions of background rates could be more precisely determined in long-term measurements.

6.1.1 Parameter estimation

With simulations in PENTrack I was able to estimate the parameters (table 6.1). Scaling the intensity of the simulated UCN source to the expected intensity of $6 \cdot 10^5\,\mathrm{cm}^{-2}\,\mathrm{s}^{-1}$ [18]—and accounting for some losses along the UCN guides from the source to the experiment—yields a number of initially stored low-field-seekers of $2 \cdot 10^7$. The number of UCN that is dumped into the detector within 20 s after filling is about a third of the number of those initially trapped neutrons.

Table 6.1: Estimated parameters for the Bayesian analysis of PENeLOPE.

Parameter	Value
τ_n (s)	880
N_0	$2 \cdot 10^7$
ϵ_n	0.3
b_n (s^{-1})	1
ϵ_p	0.15
b_p (s^{-1})	40
ϵ_m	0.3
T_n (s)	300
T_m (s)	20
T_b (s)	200
τ_d (ns)	0

I already estimated the extraction efficiency of protons to 70 %, of which 23 % can be detected (section 5.3). Thanks to the high signal-to-noise ratio of the APDs noise can be very well suppressed. I assumed a rate of $0.1\,\mathrm{s}^{-1}$ per channel.

In an ideal case, up to 85 % of UCN remaining in the storage volume after magnetic storage can reach the UCN detector. However, accounting for losses during transmission through at least one aluminium foil in front of the detector, I assumed that only 30 % can be detected in the UCN detector within 300 s. UCN detectors have very low background rates—I assumed $1\,\mathrm{s}^{-1}$. The background rates are estimated during a 200 s-long background measurement after each storage cycle.

With these parameters I created an artificial dataset of neutron counts, N_n and N_m, proton counts, $N_{\mathrm{p},i}$, and background counts, B_n and B_p, for thirty experimental cycles—ten with a storage time of 900 s, ten with a storage time of 1800 s, and ten with a storage time of 2700 s. These thirty cycles correspond to a continuous operation over approximately twenty-four hours.

6.1.2 Precision

Running the Bayesian analysis with the described likelihoods and prior distributions on such a dataset gives a Gaussian posterior-probability distribution for the neutron lifetime. The standard deviation of this distribution is the statistical precision of the measurement. A dataset created with the parameters in table 6.1 gives a precision for the neutron lifetime of 0.25 s for the neutrons-only measurement, 0.21 s for the protons-only measurement, and 0.17 s for the combined measurement (figure 6.4).

To rule out any skew in the analysis itself we can look at the deviation of the mean of the posterior-probability distribution from the real lifetime value divided by the width of the posterior-probability distribution. The distribution of this pull in many measurements should have a mean of zero and a width of one. Pull distributions from analyses of one thousand datasets are shown in figure 6.5. The neutrons-only, protons-only, and

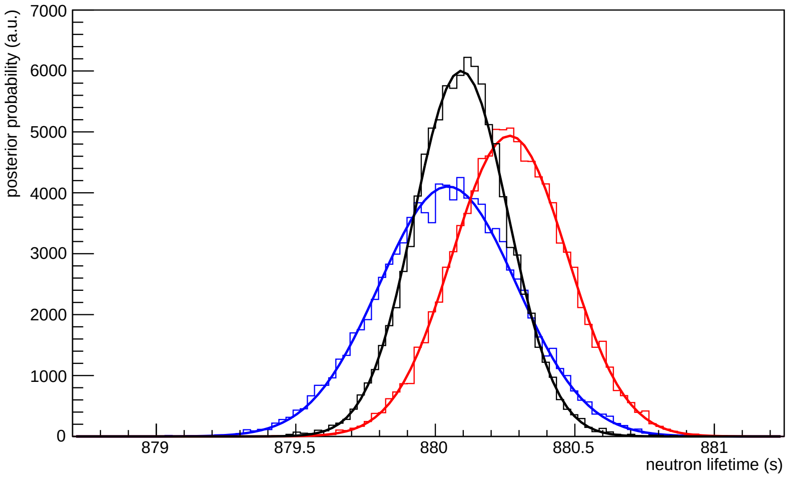

Figure 6.4: Posterior-probability distributions of neutron lifetime obtained from an artificial dataset with parameters from table 6.1 and Bayesian analyses using the neutrons-only model (blue), the protons-only model (red), and the combined model (black). Each probability distribution is fit with a Gaussian distribution; its standard deviation is the statistical precision.

combined analyses have mean pulls of 0.06 ± 0.04, 0.048 ± 0.025, and 0.041 ± 0.022 with widths of 1.05 ± 0.03, 0.98 ± 0.02, and 1.03 ± 0.02—with no significant deviations from the expected values.

To estimate how sensitive the precision is to changes of the individual parameters I created several datasets while varying one parameter at a time and ran the Bayesian analysis on each of the datasets.

Naturally, one can see a strong dependence of the statistical precision on the number of initially stored low-field-seekers, N_0 (figure 6.6). The precision of the neutrons-only measurement nicely follow the expected $1/\sqrt{N_0}$-dependence. The protons-only measurement, however, has a faster improvement of precision and eventually becomes more precise than the neutrons-only measurement.

This is explained by the lower signal-to-noise dependence of the neutrons-only measurement. Its precision is only significantly influenced by neutron-detector noise once it becomes one hundred times larger than expected (figure 6.7). The protons-only measurement, however, can still be improved by reduced noise (figure 6.8) or increased signal-to-noise ratio.

The statistical precision is also influenced by the detector efficiencies. A reduction in extraction and detection efficiency of neutrons directly impacts the precision of the neutrons-only measurement (figure 6.9). However, the proton measurement is not affected and can maintain the precision of the combined measurement.

The protons-only measurement is similarly affected by a reduction of proton extraction and detection efficiency (figure 6.10). In the combined measurement, a precise proton

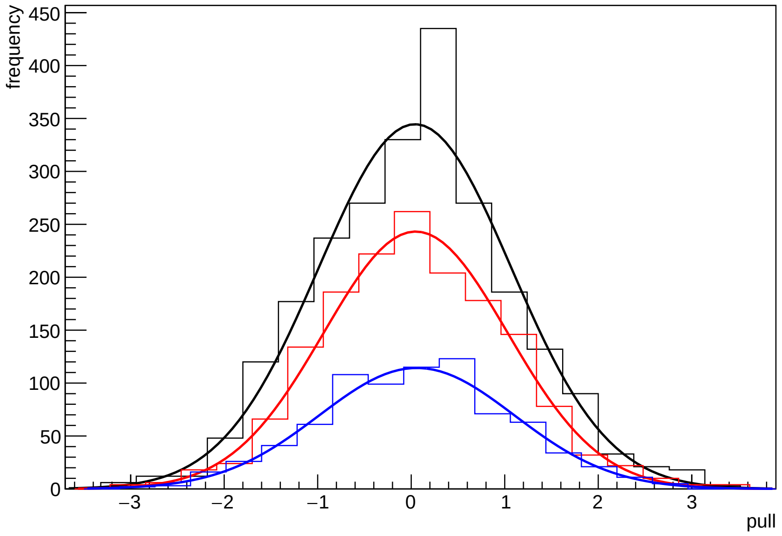

Figure 6.5: Pull distribution from analysis results of one thousand datasets. The combined results (black) and protons-only results (red) are scaled up in comparison to the neutrons-only results (blue) to be able to distinguish the three distributions.

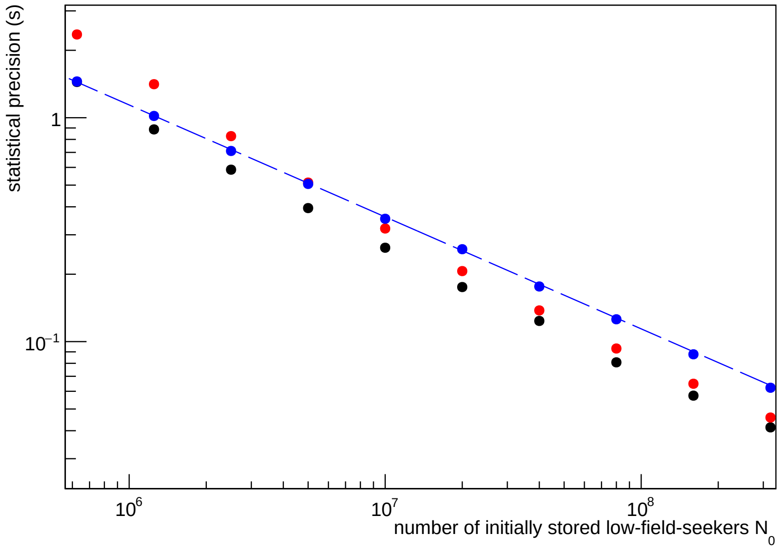

Figure 6.6: Statistical precision—obtained from the neutrons-only model (blue), protons-only model (red), and combined model (black)—depending on the number of initially stored low-field-seekers, N_0. The neutrons-only precision follows the expected $1/\sqrt{N_0}$-dependence (dashed line).

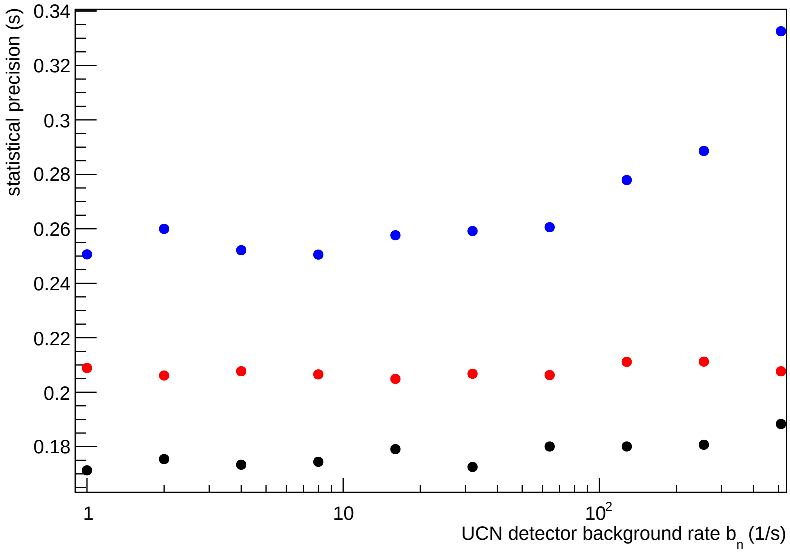

Figure 6.7: Statistical precision—obtained from the neutrons-only model (blue), protons-only model (red), and combined model (black)—depending on the background rate of the UCN detector, b_{n}.

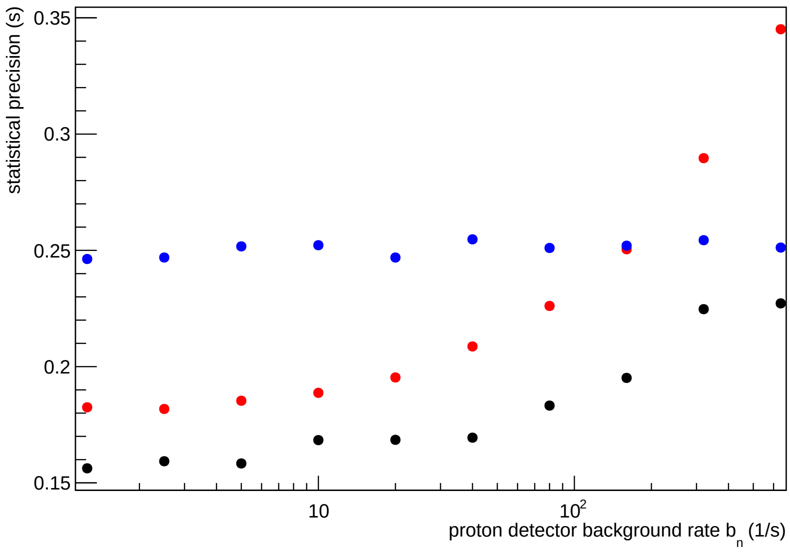

Figure 6.8: Statistical precision—obtained from the neutrons-only model (blue), protons-only model (red), and combined model (black)—depending on the background rate of the proton detector, b_{p}.

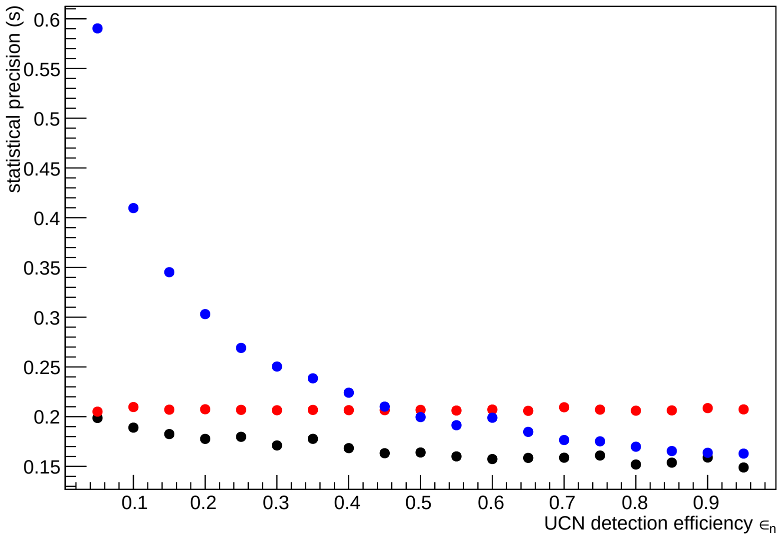

Figure 6.9: Statistical precision—obtained from the neutrons-only model (blue), protons-only model (red), and combined model (black)—depending on the UCN extraction and detection efficiency, ϵ_{n}.

measurement is required to estimate the number of initially stored low-field-seekers. Consequently, the combined measurement precision can be reduced by low proton-detection efficiency.

Additionally, the precision of the neutrons-only measurement is affected if $\epsilon_{\mathrm{m}} < \epsilon_{\mathrm{n}}$ (figure 6.11). The combined measurement is not affected, since the estimation of neutron density is done by the proton measurement and ϵ_{m} does not factor into the combined measurement.

Finding the optimum combination of storage times and number of runs with each storage time is quite difficult. For a first estimation I created data sets with only two different storage times. I chose the number of runs with the longer storage time as double the number of runs with the shorter storage time and calculated the total number of runs such that the total measurement time is about twenty-four hours. I assumed that the total time for a run is 1000 s longer than the storage time itself.

For the neutrons-only measurement, a combination of a very short measurement time with a longer one—around 2500 s—yields the best statistical precision within twenty-four hours (figure 6.12). The protons-only measurement, however, favors a measurement with only one long storage time around 2500 s, which would make an proper neutrons-only measurement impossible (figure 6.13). Therefore, the combined measurement yields the best precision for a combination of a short storage time of several hundred seconds and a longer storage time of about 2500 s to 3000 s (figure 6.14).

The best precision for storage times of 800 s and 2500 s is achieved with ten runs with the shorter storage time (figure 6.15) and twenty runs with the longer storage time

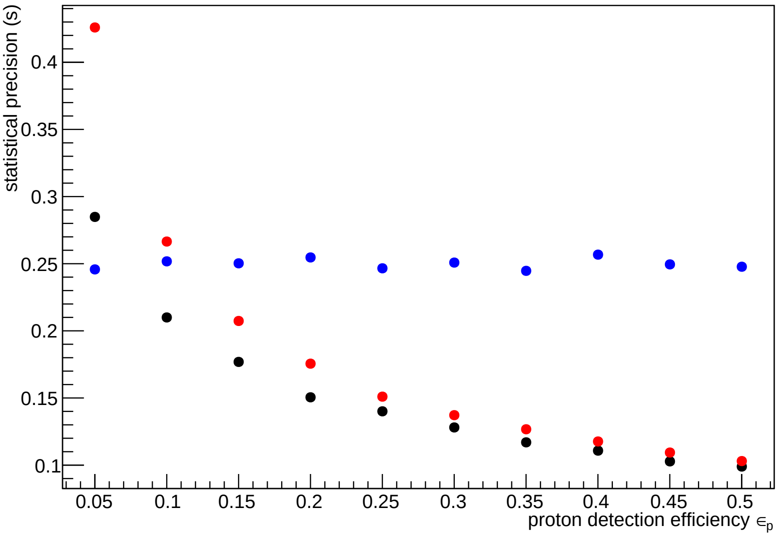

Figure 6.10: Statistical precision—obtained from the neutrons-only model (blue), protons-only model (red), and combined model (black)—depending on the proton-extraction and -detection efficiency, ϵ_{p}.

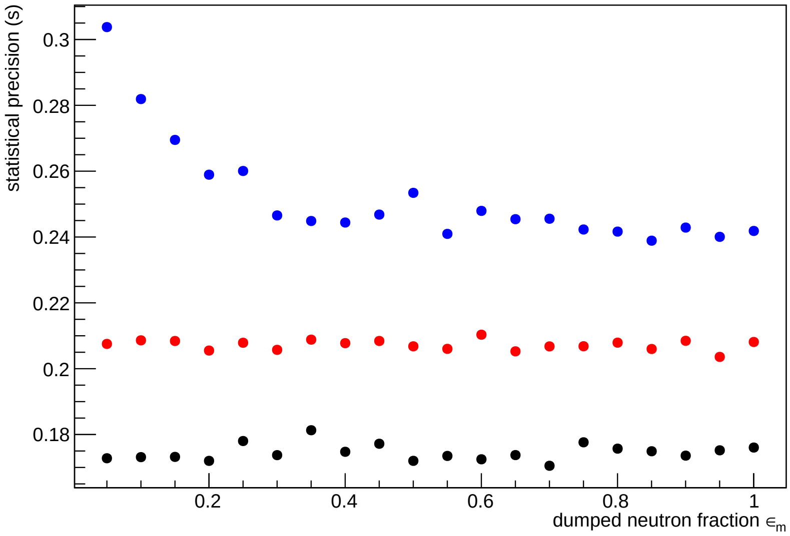

Figure 6.11: Statistical precision—obtained from the neutrons-only model (blue), protons-only model (red), and combined model (black)—depending on the ratio of the number of dumped neutrons at the beginning of cleaning to the number of initially trapped low-field-seekers, ϵ_{m}.

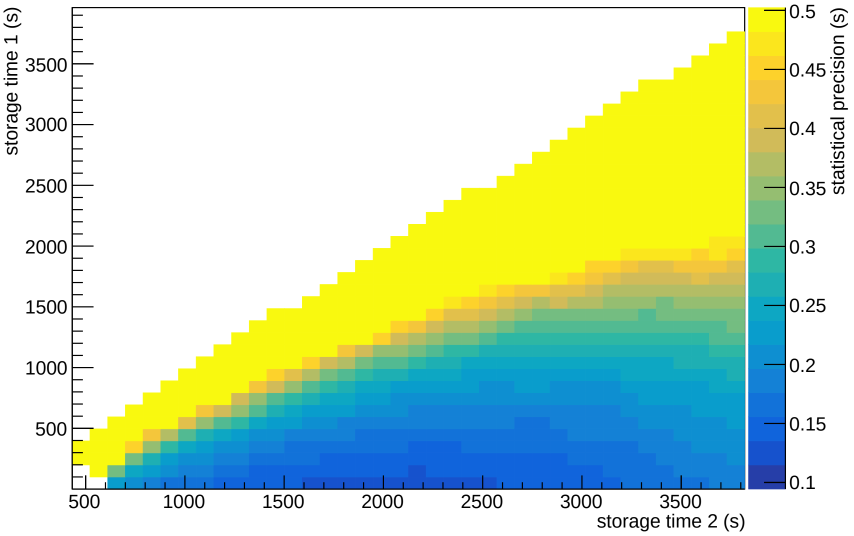

Figure 6.12: Statistical precision—obtained from the neutrons-only model—depending on the combination of two different storage times.

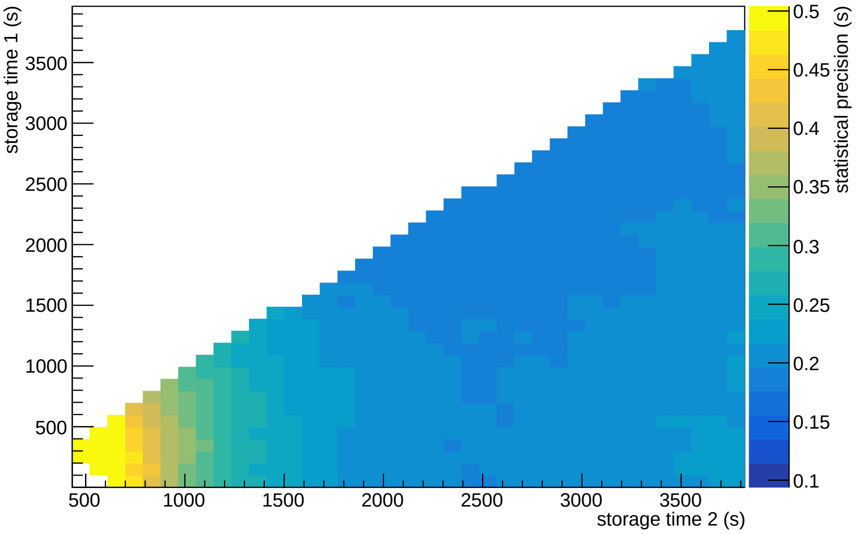

Figure 6.13: Statistical precision—obtained from the protons-only model—depending on the combination of two different storage times.

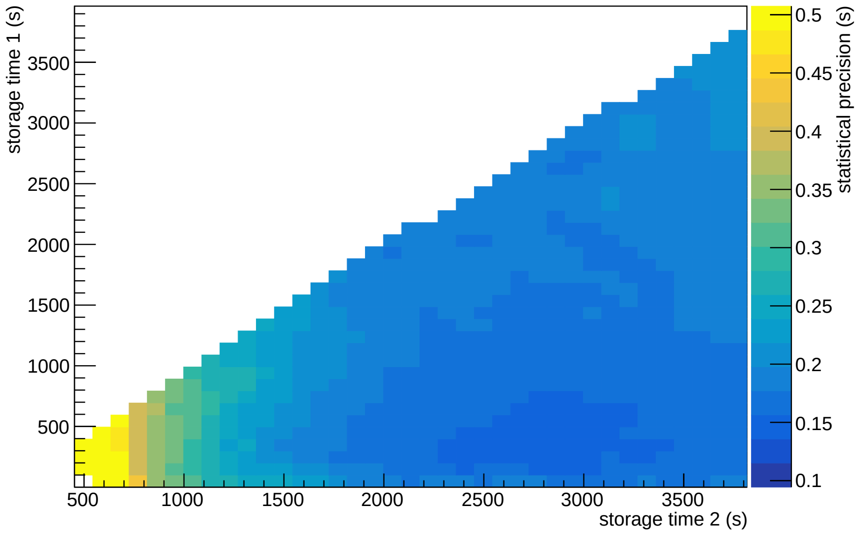

Figure 6.14: Statistical precision—obtained from the combined model—depending on the combination of two different storage times.

to fill up the total time of twenty-four hours. The neutrons-only measurement has a clear optimum combination, while the protons-only measurement favors as few short measurements as possible. Generally, the longer storage time should be used more often than the shorter storage time to offset the reduced neutron statistics gathered after long storage times and improve the protons-only precision.

6.1.3 Accuracy

To study different systematic effects, I prepared "perfect" datasets without any statistical Poisson fluctuations. The neutron, proton, and background counts were instead directly calculated from the average rates. An analysis of such a dataset yields a posterior-probability distribution perfectly centered on the real value. I then added systematic contributions to these datasets to see if they cause any shift of the central value of the posterior-probability distribution.

A fluctuation of source intensity—and initially stored low-field-seekers—does not have any effect (figure 6.16), since it can be very well estimated—in the neutrons-only measurement from the dumped neutron count and in both other measurements from the proton rate.

Fluctuations of the number of stored UCN during cleaning or ramping of the magnet are not detected in the neutron dump and can cause a random shift in the neutrons-only measurement. To estimate the shift in the worst case of a fluctuation correlated with storage time, I created datasets where the number of stored UCN is reduced in the runs with the shortest storage times and increased in the runs with the longest storage times.

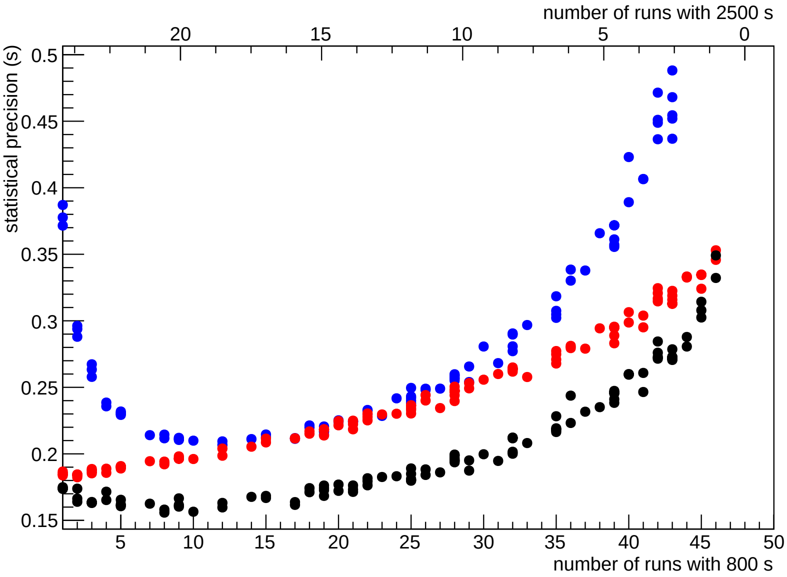

Figure 6.15: Statistical precision—obtained from the neutrons-only model (blue), protons-only model (red), and combined model (black)—with different combinations of cycles with storage times of 800 s and 2500 s. The total run time was fixed to approximately 24 h.

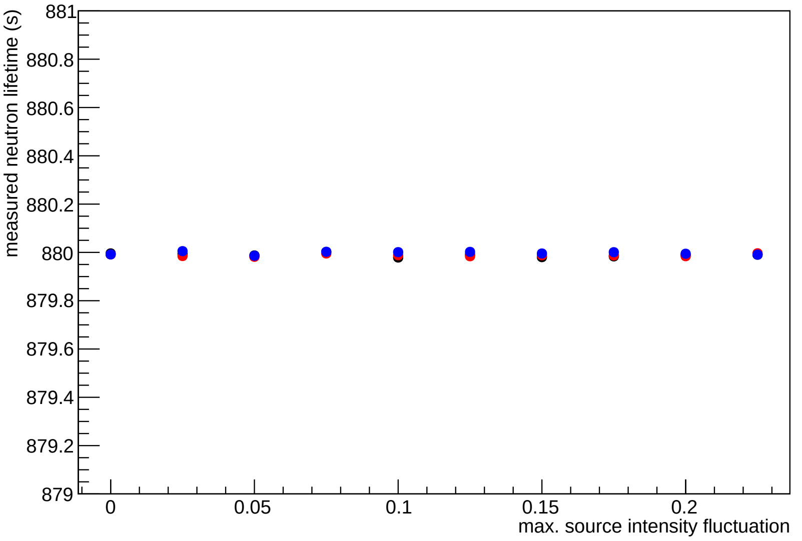

Figure 6.16: Systematic shift of measured neutron lifetime due to fluctuations in UCN-source intensity.

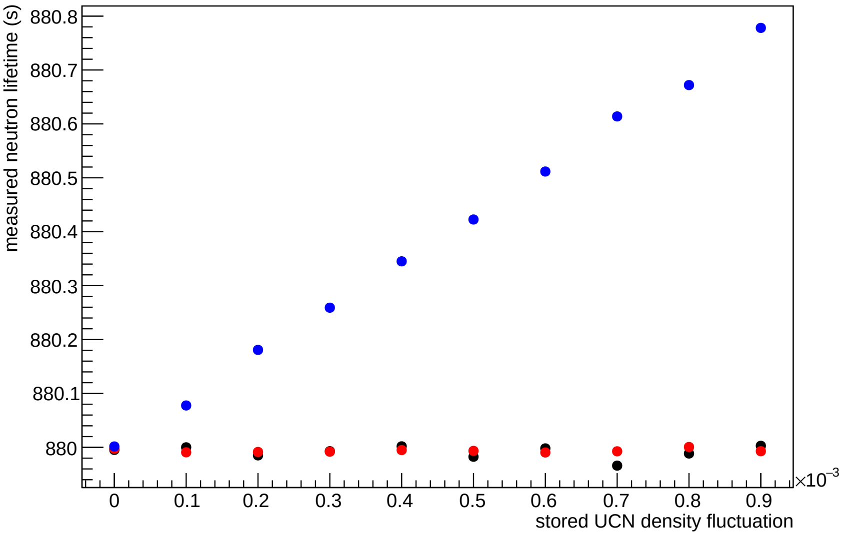

Figure 6.17: Systematic shift of measured neutron lifetime due to fluctuations in stored UCN density during cleaning or ramping of the magnet.

To reduce the shift of the neutrons-only measurement to below 0.1 s, the fluctuations have to be smaller than 10^{-4} (figure 6.17). Both other measurements again estimate the actual number of initially stored low-field-seekers from the proton rate and are not affected. Systematic effects due to rest gas adsorption, imprecise timing (section 3.4), and imprecise absorber positioning (section 5.2) would only impact the neutrons-only measurement and can be completely eliminated in a protons-only or combined measurement.

Additionally, background measurements after each cycle can eliminate any effects due to fluctuations of neutron and proton detector background rate between storage cycles (figures 6.18, 6.19).

To estimate the effect of a proton detector dead time, I reduced the proton rate in the created dataset according to equation (5.10) while the analysis assumed that there is no dead time, i.e. $\lambda' = \lambda$. A shift to longer measured lifetimes can clearly be seen with effective dead times larger than 10 ns (figure 6.20) and the analysis indeed should take into account this effect.

A similar effect can be expected in the neutron detector. Shorter storage times cause larger rates in the detector and a greater reduction in apparent rate. For a CASCADE detector, Klein and Schmidt [66] specify a neutron rate capability of 330 kHz at a dead time of 10 % for a single channel. The rates seen during neutron counting are close to this limit (figure 6.2). Depending on the number of detector channels this effect could become much larger than that in the proton detector, which sees much lower rates. A precise characterization of the used UCN detector will be necessary to compensate the resulting shift in measured neutron lifetime.

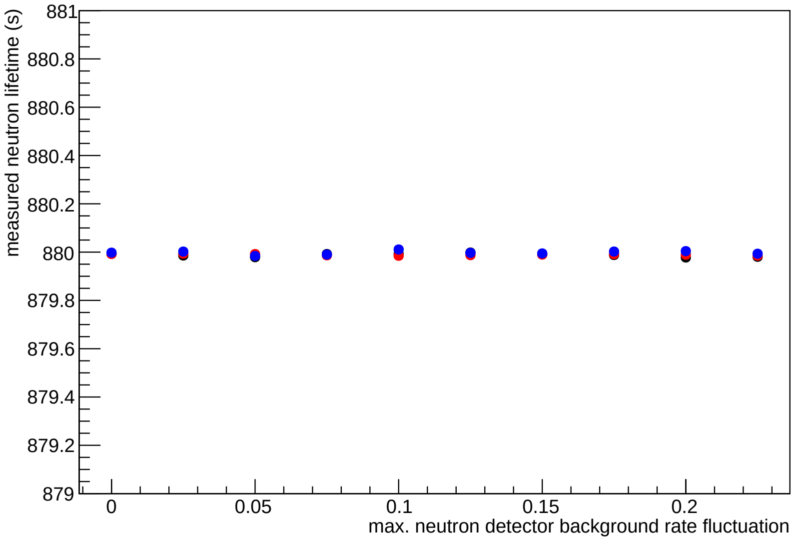

Figure 6.18: Systematic shift of measured neutron lifetime due to fluctuations in background rate of the neutron detector, b_{n}.

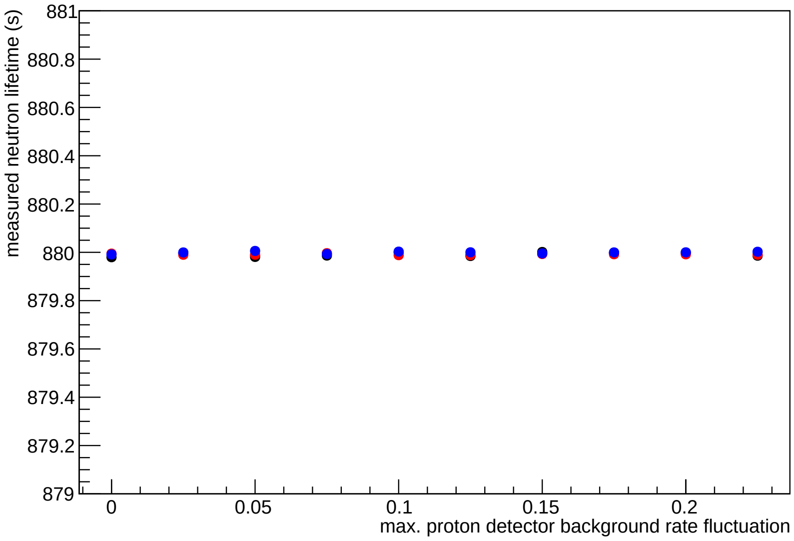

Figure 6.19: Systematic shift of measured neutron lifetime due to fluctuations in proton detector background rate, b_{p}.

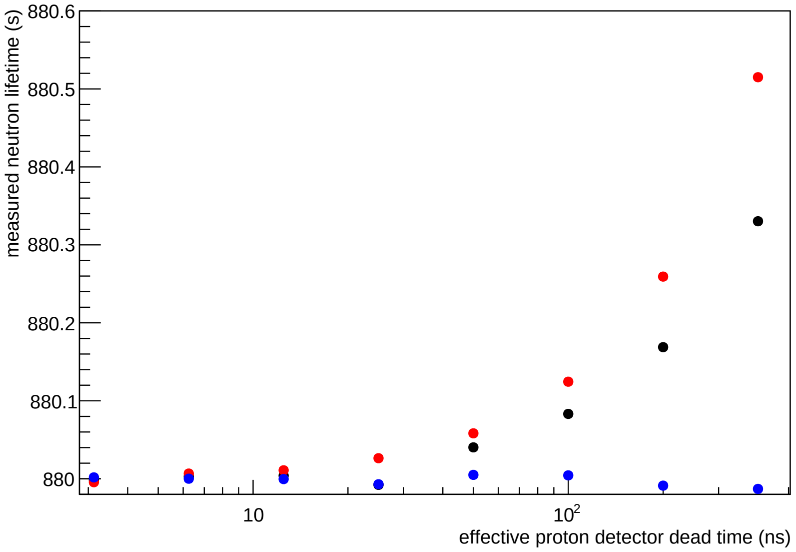

Figure 6.20: Systematic shift of measured neutron lifetime due to a proton-detector dead time, τ_d.

Finally, I determined the effect of a population of UCN with loss rates higher than that of beta decay in the storage volume. I added a small fraction of the number of initially stored low-field-seekers, N_i/N_lfs, with an increased loss rate and determined the deviation of the measured neutron lifetime from the true value (figs. 6.21-6.23).

The neutrons-only measurement is quite robust against UCN with loss rates higher than $10^{-2}\,\mathrm{s}^{-1}$ since they are mostly gone when the first measurement takes place after 900 s. The largest effect in all three measurements is caused by UCN with a loss rate of about $10^{-3}\,\mathrm{s}^{-1}$. To achieve the aspired accuracy of 0.1 s, the population of UCN with such a loss rate should be reduced to $3 \cdot 10^{-4}$ or less of the number of trapped low-field-seekers.

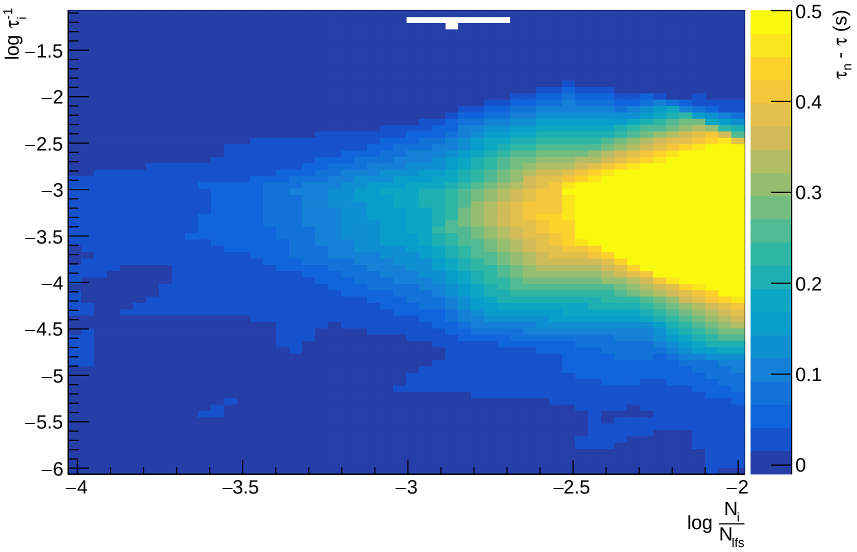

Figure 6.21: Deviation of the measured neutron lifetime, τ, from the real value, τ_n, due to a number of UCN, N_i, with a loss rate, τ_i^{-1}, additional to the beta-decay rate. The analysis used the neutrons-only model.

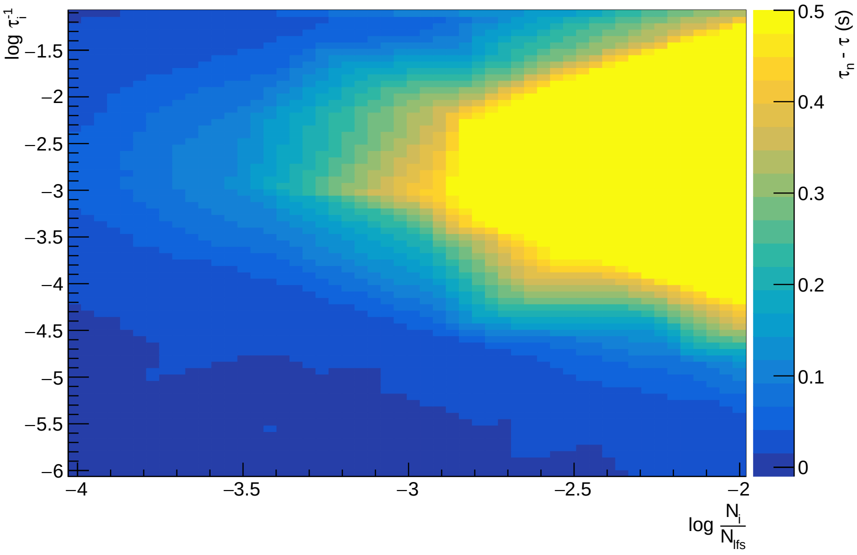

Figure 6.22: Deviation of the measured neutron lifetime, τ, from the real value, τ_n, due to a number of UCN, N_i, with a loss rate, τ_i^{-1}, additional to the beta-decay rate. The analysis used the protons-only model.

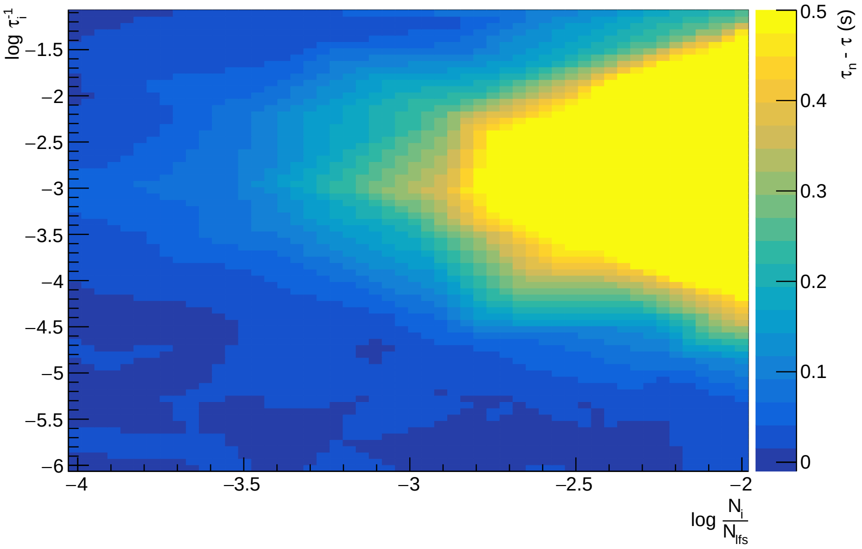

Figure 6.23: Deviation of the measured neutron lifetime, τ, from the real value, τ_n, due to a number of UCN, N_i, with a loss rate, τ_i^{-1}, additional to the beta-decay rate. The analysis used the combined model.

7 Conclusions

Much progress towards first measurements with PENeLOPE has been made.

Extensive tests of the first superconducting coils showed that the individual coils perform as required. A single bottom coil, a stack of three outer coils, and a single inner coil reached their nominal load, could be operated for at least an hour at this load, and could be ramped up or down in less than 100 s. However, extensive training is necessary to reach these high loads.

The required UCN polarization of 0.9999 can be achieved by efficient pre-polarization during filling and in-situ polarization with movable UCN absorbers. Polarizing foils with thin, magnetized iron films—scaled up to the guide diameters of 115 mm used at FRM II's UCN source—can achieve a pre-polarization of 95 %.

Depolarization of UCN at the walls during ramping of the magnet can convert high-field-seekers into marginally trapped low-field-seekers, introducing a large, yet unaccounted systematic effect into the neutron-lifetime measurement. The walls of the storage volume will have to be coated with materials with a probability of depolarization smaller than 10^{-5}—a thick nickel-phosphorus coating might be a viable candidate.

With the high expected intensity of the UCN source at FRM II, PENeLOPE should achieve a statistical precision of 0.2 s within twenty-four hours of continuous operation. A combined analysis of its two neutron-lifetime measurements can eliminate systematic effects due to fluctuations of UCN density during filling, cleaning, and ramping. Without any other corrections, PENeLOPE should be able to achieve a total systematic accuracy better than 0.22 s (see table 7.1).

7.1 Own contributions

With the simulation tool PENTrack, I optimized the experiment geometry for the filling and cleaning stages. I was able to work out a design for the UCN-feeder guide, which slightly reduces UCN density by 10 % to 15 % compared to an ideal feeder, but is simple to build, can compensate thermal contraction, and can separate the insulation vacuum from the experimental vacuum.

We conducted extensive tests of the first superconducting coils to test their performance. I was also able to show that the coils still can operate at their highest loads while only partially immersed in liquid helium and subjected to external heat loads—similar to the operating conditions in PENeLOPE.

We partly automated the coil-training procedure by upgrading the slow-control system of our coil-test experiment CoTEx. It now allows much faster analysis of quench temperatures, voltages, pressures, and liquid-helium levels and remote control of pumps,

Table 7.1: Estimated shift of measured neutron lifetime due to systematic effects.

Effect	Shift (s)	Notes
varying intial UCN density (see chapter 3.4):		
fluctuating source	negligible	can be compensated with monitor detector, [1]
thermal contraction	<0.07	shift of storage volume by 0.1 mm, [1]
adsorbed rest gas	<0.5	[1], [2]
timing of stages	<0.02	timing accuracy <10 ms, [1]
absorber position (see ch. 5.2)	<0.03	positioning accuracy <0.01 mm, [1]
loss of UCN during magnetic storage (see chapter 5.1):		
interaction with rest gas	<0.01	[2]
depolarization	<0.001	nominal central current of 12 500 A
marginally trapped neutrons	<0.02	with optimal cleaning time
UCN heating	negligible	magnet stability <100 ppm, central-current stability <1 %
high-field-seekers	(>100)	no polarization
high-field-seekers	(<1)	90 % pre-polarization, [3]
high-field-seekers	<0.03	pre- and in-situ polarization
depolarized high-field-seekers	(<0.3)	no pre-polarization, [3]
depolarized high-field-seekers	<0.03	90 % pre-polarization, [3]
proton measurement (see chapter 5.3.3):		
varying UCN distribution	negligible	distribution completely randomized during cleaning
interaction with rest gas	<0.1	[2]
proton-detector dead time	0.03	can be compensated in analysis
clock drift	<0.001	clock stability <1 ppm
neutron-detector dead time	TBD	can be compensated with precise characterization of UCN detector

[1] Can be compensated by combining proton and neutron measurement.

[2] A stable vacuum pressure of $(1.00 \pm 0.05) \cdot 10^{-8}$ mbar is assumed.

[3] A depolarization probability at the walls of $<10^{-5}$ is assumed.

valves, and power supplies. Additionally, I made the active quench protection much more reliable.

I characterized UCN-polarizing foils and spin flippers, and showed that they can achieve the required UCN pre-polarization of 90 % or more. For in-situ polarization with movable UCN absorbers, I built a complete actuation and vacuum-feed-through system with the required positioning precision of 0.01 mm, which can serve as a test bench for the absorbers itself.

With PENTrack, I estimated several potential systematic effects on the neutron-lifetime measurements due to UCN that cannot be losslessly stored in the trap. I showed that a major effect could be caused by depolarization of UCN on the guides and storage-volume walls.

To be able to operate the proton detector at a high post-acceleration potential, we worked out a proton-detector design that places the front-end electronics directly above PENeLOPE's storage volume, inside a pressurized tank and a radiation shield cooled by liquid nitrogen. Based on data from PENTrack, I suggest an optimized arrangement of the detectors—400 to 1000 Large-Area Avalanche Photo Diodes—to maximize extraction and detection efficiency of protons.

Finally, using the Bayesian Analysis Toolkit, I worked out a Bayesian analysis scheme for PENeLOPE. It can determine the neutron lifetime from a set of measurement cycles using only neutron-detector data, only proton-detector data, or both combined. With parameters estimated from PENTrack and the expected UCN-source intensity, I estimated the statistical precision of PENeLOPE. Additionally, I showed how different systematic effects influence the individual neutrons-only and protons-only analyses (table 7.1) and how a combined analysis can eliminate some of these effects and yield major improvements to PENeLOPE's accuracy.

7.2 Outlook

To validate the required coating with low probability of depolarization, we plan depolarization measurements of NiP coatings with different thicknesses, phosphor concentrations, and coating processes at the Depol experiment at Paul-Scherrer-Institut. This should give us valuable information to work out a process to coat the complete magnet.

Since all tests of superconducting coils were successful, we decided that not all produced coils have to be tested. As a last test of the almost complete topology, we will train an assembly of all four bottom coils, one inner coil, and one outer coils by the end of 2016.

Following this test, the whole magnet will be assembled. The design and construction of the cryostat is planned for 2017, and we expect delivery of the complete cryostat end of 2017. It will be integrated with its support platform, UCN guides, UCN polarizers, UCN valves, UCN absorbers, proton detector, and central current at the Maier-Leibnitz-Laboratorium, Garching.

There, the magnet will undergo final training using the helium liquefiers of the UCN source and we will perform tests of the vacuum system, absorber, and proton detector. The platform, UCN guides, and UCN valves are currently designed; the diameter of the

Replika guides will, however, be reduced from 115 mm to 100 mm, requiring new UCN polarizers and flippers. We already built first prototypes of UCN absorbers that could potentially fulfill the challenging requirements but will still need some improvements. The final design of the proton detector and its electronics is ongoing and should be finished by the end of 2016. For the central current, we worked out a final design and the first parts will arrive beginning of 2017.

Once the commissioning is finished, PENeLOPE will, together with the UCN source, move to the FRM II—possibly as early as 2018.

List of Figures

List of Tables

Bibliography

[1] W. Bothe and H. Becker. “Künstliche Erregung von Kern-γ-Strahlen”. In: *Zeitschrift für Physik* 66.5-6 (May 1930), pp. 289–306. ISSN: 14346001. DOI: `10.1007/BF01390908` (cit. on p. 7).

[2] James Chadwick. “Possible Existence of a Neutron”. In: *Nature* 129.No. 3252 (Feb. 1932), pp. 312–312. ISSN: 0028-0836. DOI: `10.1038/129312a0` (cit. on p. 7).

[3] W. Heisenberg. “Über den Bau der Atomkerne. I.” In: *Zeitschrift für Physik* 77.1-2 (Jan. 1932), pp. 1–11. ISSN: 14346001. DOI: `10.1007/BF01342433` (cit. on p. 7).

[4] E. Fermi. “Versuch einer Theorie der β-Strahlen. I”. In: *Zeitschrift für Physik* 88.3-4 (Mar. 1934), pp. 161–177. DOI: `10.1007/BF01351864` (cit. on p. 7).

[5] L. Meitner and O.R Frisch. “Disintegration of Uranium by Neutrons: a New Type of Nuclear Reaction”. In: *Nature* 143.3615 (Feb. 1939), pp. 239–240. ISSN: 0028-0836. DOI: `10.1038/224466a0` (cit. on p. 7).

[6] Otto Hahn and Fritz Strassmann. “Nachweis der Entstehung aktiver Bariumisotope aus Uran und Thorium durch Neutronenbestrahlung; Nachweis weiterer aktiver Bruchstücke bei der Uranspaltung”. In: *Die Naturwissenschaften* 27.6 (Feb. 1939), pp. 89–95. ISSN: 00281042. DOI: `10.1007/BF01488988` (cit. on p. 7).

[7] A. Steyerl. “A "neutron turbine" as an efficient source of ultracold neutrons”. In: *Nuclear Instruments and Methods* 125.3 (1975), pp. 461–469. ISSN: 0029554X. DOI: `10.1016/0029-554X(75)90265-7` (cit. on p. 8).

[8] A. Steyerl et al. “A new source of cold and ultracold neutrons”. In: *Physics Letters A* 116.7 (1986), pp. 347–352. ISSN: 03759601. DOI: `10.1016/0375-9601(86)90587-6` (cit. on p. 8).

[9] I. Altarev. “Universal liquid-hydrogen source of polarized cold and ultracold neutrons at the VVR-M reactor of the Leningrad Institute of Nuclear Physics”. In: *Pis’ma Zh. Eksp. Teor. Fiz.* 44.6 (1986), pp. 269–272 (cit. on p. 8).

[10] A. Saunders et al. “Performance of the Los Alamos National Laboratory spallation-driven solid-deuterium ultra-cold neutron source”. In: *Review of Scientific Instruments* 84.1 (2013), p. 013304. ISSN: 00346748. DOI: `10.1063/1.4770063` (cit. on p. 8).

[11] E. Korobkina et al. “An ultracold neutron source at the NC State University PULSTAR reactor”. In: *Nuclear Instruments and Methods in Physics Research, Section A: Accelerators, Spectrometers, Detectors and Associated Equipment* 579.1 (2007), pp. 530–533. ISSN: 01689002. DOI: `10.1016/j.nima.2007.04.116` (cit. on p. 8).

[12] Yasuhiro Masuda et al. "Spallation Ultracold Neutron Source of Superfluid Helium below 1 K". In: *Physical Review Letters* 108.13 (Mar. 2012), p. 134801. ISSN: 1079-7114. DOI: `10.1103/PhysRevLett.108.134801` (cit. on p. 8).

[13] J. Karch et al. "Performance of the solid deuterium ultra-cold neutron source at the pulsed reactor TRIGA Mainz". In: *European Physical Journal A* 50.4 (Apr. 2014), pp. 1–11. ISSN: 1434601X. DOI: `10.1140/epja/i2014-14078-9` (cit. on p. 8).

[14] F. M. Piegsa et al. "New source for ultracold neutrons at the Institut Laue-Langevin". In: *Physical Review C* 90.1 (July 2014), p. 015501. ISSN: 0556-2813. DOI: `10.1103/PhysRevC.90.015501` (cit. on p. 8).

[15] Bernhard Lauss. "Ultracold neutron production at the second spallation target of the Paul Scherrer Institute". In: *Physics Procedia*. Vol. 51. Elsevier, 2014, pp. 98–101. DOI: `10.1016/j.phpro.2013.12.022`. arXiv: `arXiv:1202.6003v1` (cit. on p. 8).

[16] A. P. Serebrov et al. "Supersource of ultracold neutrons at WWR-M reactor in pnpi and the research program on fundamental physics". In: *Physics Procedia*. Vol. 17. 2011, pp. 251–258. DOI: `10.1016/j.phpro.2011.06.044` (cit. on p. 8).

[17] Yun Chang Shin. "TRIUMF Ultra-cold Neutron Source Facility". In: *14th Annual Meeting of the Northwest Section of the APS*. Vancouver, Canada, 2012 (cit. on p. 8).

[18] Andreas Frei. *UCN density calculations for the new UCN source at the FRM II*. Tech. rep. Rev. 1. Forschungs-Neutronenquelle Heinz Maier-Leibnitz (FRM II), 2013 (cit. on pp. 8, 16, 116).

[19] Peter J. Mohr, David B. Newell, and Barry N. Taylor. *CODATA Recommended Values of the Fundamental Physical Constants: 2014*. 2015. DOI: `10.5281/ZENODO.22826` (cit. on pp. 8, 34).

[20] Joel Holdsworth. *The Feynman diagram for the beta-negative decay of a neutron into a proton.* 2007 (cit. on p. 9).

[21] William J. Marciano and Alberto Sirlin. "Improved calculation of electroweak radiative corrections and the value of V_{ud}". In: *Physical Review Letters* 96.3 (Jan. 2006), p. 032002. ISSN: 10797114. DOI: `10.1103/PhysRevLett.96.032002`. arXiv: `0510099 [hep-ph]` (cit. on p. 9).

[22] K.A. Olive. "Review of Particle Physics". en. In: *Chinese Physics C* 38.9 (Aug. 2014), p. 090001. ISSN: 1674-1137. DOI: `10.1088/1674-1137/38/9/090001` (cit. on pp. 9, 10, 12, 116).

[23] J. C. Hardy and I. S. Towner. "Superallowed $0^+ \to 0^+$ nuclear β decays: A new survey with precision tests of the conserved vector current hypothesis and the standard model". In: *Physical Review C - Nuclear Physics* 79.5 (May 2009), p. 055502. ISSN: 05562813. DOI: `10.1103/PhysRevC.79.055502`. arXiv: `0812.1202` (cit. on pp. 9, 10).

[24] A. T. Yue et al. “Improved determination of the neutron lifetime”. In: *Physical Review Letters* 111.22 (2013), p. 222501. ISSN: 00319007. DOI: `10.1103/PhysRevLett.111.222501`. arXiv: `1309.2623` (cit. on pp. 10, 12).

[25] A. Serebrov et al. “Measurement of the neutron lifetime using a gravitational trap and a low-temperature Fomblin coating”. In: *Physics Letters, Section B: Nuclear, Elementary Particle and High-Energy Physics* 605.1-2 (2005), pp. 72–78. ISSN: 03702693. DOI: `10.1016/j.physletb.2004.11.013`. arXiv: `0408009 [nucl-ex]` (cit. on pp. 10, 12).

[26] D. Dubbers et al. “A clean, bright, and versatile source of neutron decay products”. In: *Nuclear Instruments and Methods in Physics Research, Section A: Accelerators, Spectrometers, Detectors and Associated Equipment* 596.2 (2008), pp. 238–247. ISSN: 01689002. DOI: `10.1016/j.nima.2008.07.157` (cit. on p. 9).

[27] Maxim Pospelov and Josef Pradler. “Big Bang nucleosynthesis as a probe of new physics”. In: *Annual Review of Nuclear and Particle Science* 60 (2010), pp. 539–568. ISSN: 0163-8998. DOI: `10.1146/annurev.nucl.012809.104521`. arXiv: `1011.1054` (cit. on p. 11).

[28] S. S. Arzumanov, L. N. Bondarenko, V. I. Morozov, Yu. N. Panin, and S. M. Chernyavsky. “Analysis and correction of the measurement of the neutron lifetime”. In: *JETP Letters* 95.5 (May 2012), pp. 224–228. ISSN: 0021-3640. DOI: `10.1134/S0021364012050025` (cit. on p. 12).

[29] A. Steyerl, J. M. Pendlebury, C. Kaufman, S. S. Malik, and A. M. Desai. “Quasielastic scattering in the interaction of ultracold neutrons with a liquid wall and application in a reanalysis of the Mambo I neutron-lifetime experiment”. In: *Physical Review C* 85.6 (June 2012), p. 065503. ISSN: 0556-2813. DOI: `10.1103/PhysRevC.85.065503` (cit. on p. 12).

[30] G. Mention et al. “Reactor antineutrino anomaly”. In: *Physical Review D - Particles, Fields, Gravitation and Cosmology* 83.7 (2011), pp. 1–20. ISSN: 15507998. DOI: `10.1103/PhysRevD.83.073006`. arXiv: `1101.2755` (cit. on p. 12).

[31] V. Vladimirskiy. “Magnetic mirrors, channels and bottles for neutrons”. In: *Sov. Phys. JETP* 12 (1961), pp. 740–746 (cit. on p. 12).

[32] W. Paul, F. Anton, L. Paul, S. Paul, and W. Mampe. “Measurement of the neutron lifetime in a magnetic storage ring”. In: *Zeitschrift für Physik C Particles and Fields* 45.1 (Mar. 1989), pp. 25–30. ISSN: 0170-9739. DOI: `10.1007/BF01556667` (cit. on p. 12).

[33] V. F. Ezhov et al. “Magnetic storage of UCN for a measurement of the neutron lifetime”. In: *Nuclear Instruments and Methods in Physics Research, Section A: Accelerators, Spectrometers, Detectors and Associated Equipment* 611.2-3 (2009), pp. 167–170. ISSN: 01689002. DOI: `10.1016/j.nima.2009.07.071` (cit. on p. 12).

[34] D. J. Salvat et al. “Storage of ultracold neutrons in the magneto-gravitational trap of the UCN τ experiment”. In: *Physical Review C* 89.5 (May 2014), p. 052501. ISSN: 0556-2813. DOI: `10.1103/PhysRevC.89.052501` (cit. on pp. 12, 104, 108).

[35] K. K. H. Leung, P. Geltenbort, S. Ivanov, F. Rosenau, and O. Zimmer. "Neutron lifetime measurements and effective spectral cleaning with an ultracold neutron trap using a vertical Halbach octupole permanent magnet array". In: *Physical Review C* 94.4 (Oct. 2016), p. 045502. ISSN: 2469-9985. DOI: `10.1103/PhysRevC.94.045502` (cit. on p. 12).

[36] Marcus Beck et al. "The neutron lifetime experiment τSPECT". In: *DPG–Frühjahrstagung, Fachverband Physik der Hadronen und Kerne.* Darmstadt, 2016, HK 26.2 (cit. on p. 12).

[37] I. Altarev et al. "Direct experimental verification of neutron acceleration by the material optical potential of solid $^2H_2$". In: *Physical Review Letters* 100.1 (Jan. 2008), p. 14801. ISSN: 00319007. DOI: `10.1103/PhysRevLett.100.014801` (cit. on pp. 17, 28).

[38] R. Picker et al. "Investigation of titanium and polyethylene as UCN absorber materials with AbEx". In: *Nuclear Instruments and Methods in Physics Research, Section A: Accelerators, Spectrometers, Detectors and Associated Equipment* 611.2-3 (2009), pp. 297–301. ISSN: 01689002. DOI: `10.1016/j.nima.2009.07.089` (cit. on p. 18).

[39] E Fermi. "Motion of neutrons in hydrogenous substances". In: *Ricerca Scientifica* 7 (1936), pp. 13–52 (cit. on p. 19).

[40] Varley F. Sears. "Neutron scattering lengths and cross sections". In: *Neutron News* 3.3 (1992), pp. 26–37. ISSN: 1044-8632. DOI: `10.1080/10448639208218770` (cit. on pp. 19, 21, 34).

[41] R Golub, D Richardson, and S K Lamoreaux. *Ultra-Cold Neutrons.* Adam Hilger, 1991 (cit. on pp. 20, 58, 85).

[42] F. Atchison et al. "Diffuse reflection of ultracold neutrons from low-roughness surfaces". In: *European Physical Journal A* 44.1 (2010), pp. 23–29. ISSN: 14346001. DOI: `10.1140/epja/i2010-10926-x` (cit. on p. 22).

[43] A. Steyerl. "Effect of surface roughness on the total reflexion and transmission of slow neutrons". In: *Zeitschrift für Physik* 254.2 (Apr. 1972), pp. 169–188. ISSN: 1434-6001. DOI: `10.1007/BF01380066` (cit. on p. 22).

[44] Sergey Bochkanov. *ALGLIB.* 2015. URL: `http://www.alglib.net/` (cit. on p. 23).

[45] W Schreyer. "Monte Carlo-simulations for the neutron lifetime experiment PENeLOPE". Diploma thesis. Technische Universität München, 2011 (cit. on pp. 25, 33, 87, 88, 103).

[46] 3D Systems Inc. *Stereolithography interface specification.* 1988. URL: `http://www.fabbers.com/tech/STL_Format` (cit. on p. 25).

[47] The CGAL project. *CGAL 4.7 User and Reference Manual.* 4.7. CGAL Editorial Board, 2015. URL: `http://doc.cgal.org/4.7/Manual/packages.html` (cit. on p. 25).

[48] Rüdiger Picker. “PENeLOPE and AbEx: On the Way Towards a New Precise Neutron Lifetime Measurement”. PhD thesis. Garching: Technische Universität München, Aug. 2008. URL: `http://mediatum.ub.tum.de/?id=650460` (cit. on p. 29).

[49] J. Steinmann. *Progress report PENeLOPE work package 1c: cryogenic analysis.* Tech. rep. Babcock Noell, 2011 (cit. on p. 29).

[50] R. J. Corruccini and J. J. Gniewek. *Thermal expansion of technical solids at low temperatures.* U.S. Dept. of Commerce, National Bureau of Standards, 1961, p. 28. URL: `http://digicoll.manoa.hawaii.edu/techreports/PDF/NBS29.pdf` (cit. on pp. 32, 56).

[51] S. Materne et al. “PENeLOPE-on the way towards a new neutron lifetime experiment with magnetic storage of ultra-cold neutrons and proton extraction”. In: *Nuclear Instruments and Methods in Physics Research, Section A: Accelerators, Spectrometers, Detectors and Associated Equipment* 611.2-3 (2009), pp. 176–180. ISSN: 01689002. DOI: `10.1016/j.nima.2009.07.055` (cit. on pp. 32, 88).

[52] A P Serebrov et al. “Superconducting UCN polarizer for a new EDM spectrometer”. In: *Nuclear Instruments and Methods in Physics Research Section A: Accelerators, Spectrometers, Detectors and Associated Equipment* 545.1–2 (2005), pp. 490–492. ISSN: 0168-9002. DOI: `10.1016/j.nima.2005.01.316` (cit. on p. 34).

[53] William M. Haynes. *CRC Handbook of Chemistry and Physics.* 95th Ed. CRC Press, 2014 (cit. on pp. 34, 40).

[54] A I Egorov, V M Lobashev, V A Nazarenko, G D Porsev, and A P Serebrov. “Production, storage, and polarization of ultracold neutrons”. In: *Soviet Journal of Nuclear Physics* 19.2 (1974), pp. 147–152 (cit. on pp. 34, 42).

[55] R Herdin et al. “Experiment on the efficient polarization of ultracold neutrons”. In: *Nuclear Instruments and Methods* 148.2 (1978), pp. 353–357. ISSN: 0029-554X. DOI: `10.1016/0029-554X(70)90188-6` (cit. on pp. 34, 35, 42).

[56] T. Lauer. *Private communication.* 2013 (cit. on pp. 34–36, 40, 42).

[57] T. J L Jones and W. G. Williams. “Non-adiabatic spin flippers for thermal neutrons”. In: *Nuclear Instruments and Methods* 152.2-3 (1978), pp. 463–469. ISSN: 0029554X. DOI: `10.1016/0029-554X(78)90047-2` (cit. on p. 34).

[58] I. I. Rabi, N. F. Ramsey, and J. Schwinger. “Use of rotating coordinates in magnetic resonance problems”. In: *Reviews of Modern Physics* 26.2 (Apr. 1954), pp. 167–171. ISSN: 00346861. DOI: `10.1103/RevModPhys.26.167` (cit. on p. 34).

[59] A. T. Holley et al. “A high-field adiabatic fast passage ultracold neutron spin flipper for the UCNA experiment”. In: *Review of Scientific Instruments* 83.7 (2012), p. 73505. ISSN: 00346748. DOI: `10.1063/1.4732822` (cit. on p. 35).

[60] P. Geltenbort et al. "A compact, large-diameter adiabatic spinflipper for ultracold neutrons". In: *Nuclear Instruments and Methods in Physics Research, Section A: Accelerators, Spectrometers, Detectors and Associated Equipment* 608.1 (2009), pp. 132–138. ISSN: 01689002. DOI: `10.1016/j.nima.2009.06.038` (cit. on pp. 35, 38, 42).

[61] Tanja Huber. "Transport and Storage of Ultra-cold Neutrons in Replika-Guides". Diploma thesis. Technische Universität München, 2011 (cit. on p. 35).

[62] K Halbach. "Design of Permanent Multiple Magnets with Orientated Rare Earth Cobalt Material". In: *Nuclear Instruments and Methods* 169.1 (1980), pp. 1–10. ISSN: 0029-554X. DOI: `10.1016/0029` (cit. on p. 36).

[63] Reloop Global Distribution GmbH. *Reloop Dominance 702*. Schuckertstr. 28, 48153 Muenster/Germany, 2013 (cit. on p. 38).

[64] Stefan Schuldt. "Bau eines beweglichen Absorbers und Optimierung eines Polarisators für ultrakalte Neutronen". Bachelor's thesis. Technische Universität München, Sept. 2015 (cit. on pp. 38, 39, 46, 99, 100).

[65] HAMEG Instruments GmbH. *HZO50 AC/DC Messzange*. Industriestr. 6, 63533 Mainhausen/Germany, 2012 (cit. on p. 38).

[66] Martin Klein and Christian J. Schmidt. "CASCADE, neutron detectors for highest count rates in combination with ASIC/FPGA based readout electronics". In: *Nuclear Instruments and Methods in Physics Research Section A: Accelerators, Spectrometers, Detectors and Associated Equipment* 628.1 (2011), pp. 9–18. ISSN: 01689002. DOI: `10.1016/j.nima.2010.06.278` (cit. on pp. 40, 126).

[67] V. K. (Vladimir Kazimirovich) Ignatovich. *The physics of ultracold neutrons*. Clarendon Press, 1990, p. 397. ISBN: 9780198510154 (cit. on p. 42).

[68] Allen Caldwell, Daniel Kollar, and Kevin Kroninger. "BAT: The Bayesian Analysis Toolkit". In: *Comput. Phys. Commun.* 180.11 (2009), pp. 2197–2209. ISSN: 0010-4655. DOI: `10.1016/j.cpc.2009.06.026`. arXiv: `0808.2552 [physics.data-an]` (cit. on pp. 47, 113).

[69] A. D. Stoika, A. V. Strelkov, and M. Hetzelt. "Upscattering detected as the main reason for anomalous loss of ultra-cold neutrons in neutron storage experiments". In: *Zeitschrift für Physik B Condensed Matter and Quanta* 29.4 (1978), pp. 349–352. ISSN: 0340-224X. DOI: `10.1007/BF01324032` (cit. on p. 57).

[70] W. A. Lanford and R. Golub. "Hydrogen surface contamination and the storage of ultracold neutrons". In: *Physical Review Letters* 39.24 (1977), pp. 1509–1512. ISSN: 00319007. DOI: `10.1103/PhysRevLett.39.1509` (cit. on p. 57).

[71] W. Mampe, P. Ageron, and R. Gähler. "Ultra cold neutron life times in glow discharge cleaned bottles". In: *Zeitschrift für Physik B Condensed Matter* 45.1 (1981), pp. 1–14. ISSN: 0340224X. DOI: `10.1007/BF01294271` (cit. on p. 57).

[72] Y. Y. Kosvintsev, Y. A. Kushnir, V. I. Morozov, A. D. Stoĭka, and A. V. Strelkov. "Storage of ultracold low-energy neutrons in vessels with condensed metallic walls". In: *Soviet Journal of Experimental and Theoretical Physics Letters* 28 (Aug. 1978), p. 153 (cit. on p. 57).

[73] J. C. Bates. "A fluid walled neutron bottle". In: *Nuclear Instruments and Methods In Physics Research* 216.3 (1983), pp. 535–536. ISSN: 01675087. DOI: `10.1016/0167-5087(83)90526-4` (cit. on p. 57).

[74] Y. Y. Kosvintsev, V. I. Morozov, and G. I. Terekhov. "Storage of ultracold neutrons in a vessel long enough for β decay". In: *Soviet Journal of Experimental and Theoretical Physics Letters* 36 (Nov. 1982), p. 424 (cit. on pp. 57, 58).

[75] E Wallén. "Adsorption isotherms of He and H2 at liquid He temperatures". In: *Journal of Vacuum Science & Technology A: Vacuum, Surfaces, and Films* 15.2 (1997), pp. 265–274. ISSN: 07342101. DOI: `10.1116/1.580523` (cit. on p. 58).

[76] Johannes Amend. *Private communication.* 2015 (cit. on pp. 59, 61).

[77] L Bottura. *A Practical Fit for the Critical Surface of NbTi - LHC Project Report 358.* Tech. rep. European organization for nuclear research, 1999 (cit. on pp. 59, 60).

[78] Supercon Inc. *Certificate of compliance, wire lot no. 412E-3, type VSF-SSCI.* 2010 (cit. on p. 60).

[79] Supercon Inc. *Certificate of compliance, wire lot no. 412E-7, type VSF-SSCI.* 2012 (cit. on p. 60).

[80] Supercon Inc. *Certificate of compliance, wire lot no. 412E-10, type VSF-SSCI.* 2015 (cit. on p. 60).

[81] Supercon Inc. *Certificate of compliance, wire lot no. 412-E11, type VSF-SSCI.* 2016 (cit. on p. 60).

[82] S. Materne. "Tests of prototype magnets and study on a MCP based proton detector for the neutron lifetime experiment PENeLOPE". PhD thesis. Technische Universität München, 2013 (cit. on pp. 60, 61, 63, 105).

[83] Jochen Steinmann. *Final report: PENeLOPE—work package 1a.* Tech. rep. Babcock Noell GmbH, 2011 (cit. on pp. 60, 75, 78).

[84] Y. Iwasa. "Experimental and theoretical investigation of mechanical disturbances in epoxy-impregnated superconducting coils. 1. General introduction". In: *Cryogenics* 25.6 (June 1985), pp. 304–306. ISSN: 00112275. DOI: `10.1016/0011-2275(85)90013-X` (cit. on p. 60).

[85] Jochen Steinmann. *PENeLOPE—project status.* Tech. rep. Babcock Noell GmbH, 2011 (cit. on p. 61).

[86] Andreas Senft. "CoTEx 2.0—A New Coil Test Experiment". Diploma thesis. Technische Universität München, 2011 (cit. on pp. 61–63, 82).

[87] Jochen Steinmann. *PENeLOPE work package 1b: test coil—System description and handling instructions.* Tech. rep. Babcock Noell GmbH, 2011 (cit. on p. 61).

[88] Jochen Steinmann. *PENeLOPE work package 3: First Outer Coils—System description and handling instructions.* Tech. rep. Babcock Noell GmbH, 2013 (cit. on p. 65).

[89] Dominic Gaisbauer. "Setup and tests of the first coils of the neutron lifetime experiment PENeLOPE". Bachelor's thesis. Technische Universität München, 2013 (cit. on p. 65).

[90] DYNEX Semiconductor. *DS502ST Rectifier diode.* 2001 (cit. on p. 72).

[91] Richard V Aldridge. "On the behaviour of forward biased silicon diodes at low temperatures". In: *Solid-State Electronics* 17 (1974), pp. 617–619 (cit. on p. 73).

[92] D. L. Swartz and J. M. Swartz. *Diode and resistance cryogenic thermometry: A comparison.* 1974. DOI: `10.1016/0011-2275(74)90240-9` (cit. on p. 73).

[93] R.V. Aldridge, K. Davis, and M. Holloway. "An investigation of the effect of a magnetic field on the forward characteristics of some silicon diodes at low temperatures". In: *J. Phys. D* 8 (1975), pp. 64–68 (cit. on p. 73).

[94] Theodore L. Bergman, Adreienne S. Lavine, Frank P. Incropera, and David P. Dewitt. *Introduction to heat transfer.* 6th. John Wiley & Sons, Inc., 2012. ISBN: 978-0-470-50196-2 (cit. on p. 75).

[95] E.W. Lemmon, M.L. Huber, and M.O. McLinden. *NIST Standard Reference Database 23: Reference Fluid Thermodynamic and Transport Properties-REFPROP.* Gaithersburg, 2013. URL: `wolframalpha.com` (cit. on pp. 75, 77).

[96] E.D. Marquardt, J.P. Le, and Ray Radebaugh. "Cryogenic material properties database". In: *Cryocoolers 11.* Boston: Kluwer Academic Publishers, 2002, pp. 681–687. DOI: `10.1007/0-306-47112-4_84`. URL: `http://cryogenics.nist.gov` (cit. on pp. 75, 77).

[97] David C. Meeker. *Finite Element Method Magnetics.* 2013. URL: `femm.info` (cit. on p. 78).

[98] RUAG Space GmbH. *Thermal Insulation Products.* Stachegasse 16, 1120 Vienna, Austria, 2014. URL: `http://www.ruag.com/thermal` (cit. on p. 78).

[99] National Instruments. *NI LabVIEW for CompactRIO—Developer's Guide.* 2014. URL: `http://www.ni.com/pdf/products/us/fullcriodevguide.pdf` (cit. on pp. 78, 83).

[100] International Electrotechnical Commission. *IEC 60751 - Industrial platinum resistance thermometers and platinum temperature sensors.* 2008 (cit. on p. 79).

[101] Lake Shore Cryotronics Inc. *Cernox ^{TM} RTDs.* 2016. URL: `http://lakeshore.com/products/Cryogenic-Temperature-Sensors/Cernox/Models/pages/Specifications.aspx` (cit. on p. 79).

[102] Lake Shore Cryotronics Inc. *Model 218 Temperature Monitor.* 2015 (cit. on p. 79).

[103] Oerlikon Leybold Vacuum. *Penningvac PTR90 Operating Manual.* 2008 (cit. on p. 79).

[104] Oerlikon Leybold Vacuum. *Ionivac ITR90.* 2009 (cit. on pp. 79, 109).

[105] Leybold Vacuum. *Leybold Vacuum Center Two, Center Three Vacuum Gauge Controller.* 2004 (cit. on p. 79).

[106] WIKA Alexander Wiegand SE & Co. KG. *Druckmessumformer Für allgemeine industrielle Anwendungen Typ A-10.* 2016 (cit. on p. 79).

[107] American Magnetics Inc. *AMI liquid helium level sensor.* 2013 (cit. on p. 80).

[108] American Magnetics Inc. *Model 135 / 136 Liquid Helium Level Instrument.* 2000 (cit. on p. 80).

[109] Russell J. Donnelly and Carlo F. Barenghi. "The Observed Properties of Liquid Helium at the Saturated Vapor Pressure". In: *Journal of Physical and Chemical Reference Data* 27.6 (1998), p. 1217. ISSN: 00472689. DOI: `10.1063/1.556028` (cit. on p. 81).

[110] Maximilian Kolhep. "Füllstandsmessung für kryogene Flüssigkeiten". Bachelor's thesis. Technische Universität München, 2014 (cit. on p. 81).

[111] R S Crisp and J Rungis. "a Simple Liquid Helium Depth Gauge Using Carbon Resistors As Sensing Elements". In: *Journal Of Physics E-Scientific Instruments* 2.6 (1969), p. 541. ISSN: 00223735. DOI: `10.1088/0022-3735/2/8/331` (cit. on p. 81).

[112] Karsten Ahnert and Mario Mulansky. "Odeint – Solving Ordinary Differential Equations in C++". In: *AIP Conference Proceedings.* 1. 2011, pp. 1586–1589. ISBN: 9780735409569. DOI: `10.1063/1.3637934` (cit. on p. 87).

[113] Rüdiger Picker. "A new superconducting magnetic trap for ultra-cold neutrons". Diploma thesis. Technische Universität München, 2004 (cit. on p. 88).

[114] Christian Nielsen. *Manual — Magnet power supply 859 — System 8500.* 4040 Jyllinge, Denmark, 2009 (cit. on p. 89).

[115] Joachim Meichelböck. "Central Coil Design for the PENeLOPE Experiment". Bachelor's thesis. Technische Universität München, 2016 (cit. on p. 91).

[116] A Serebrov et al. "Depolarization of UCN stored in material traps". In: *Nuclear Instruments and Methods in Physics Research Section A: Accelerators, Spectrometers, Detectors and Associated Equipment* 440.3 (2000), pp. 717–721. ISSN: 0168-9002. DOI: `10.1016/S0168-9002(99)01068-2` (cit. on p. 92).

[117] A. P. Serebrov et al. "Depolarization of ultracold neutrons during their storage in material bottles". In: *Physics Letters, Section A: General, Atomic and Solid State Physics* 313.5-6 (2003), pp. 373–379. ISSN: 03759601. DOI: `10.1016/S0375-9601(03)00848-X` (cit. on p. 92).

[118] Z. Tang et al. “Measurement of spin-flip probabilities for ultracold neutrons interacting with nickel phosphorus coated surfaces”. In: *Nuclear Instruments and Methods in Physics Research Section A: Accelerators, Spectrometers, Detectors and Associated Equipment* 827 (2016), pp. 32–38. ISSN: 01689002. DOI: `10.1016/j.nima.2016.04.098` (cit. on pp. 92, 96).

[119] Raymond Rios. “Suppression of Ultracold Neutron Depolarization on Material Surfaces with Magnetic Holding Fields”. In: *APS April Meeting*. Denver, Colorado, 2009. URL: `http://meetings.aps.org/Meeting/APR09/Session/C14.3` (cit. on p. 93).

[120] Adam Tarte Holley. “Ultracold Neutron Polarimetry in a Measurement of the β Asymmetry”. PhD thesis. North Carolina State University, 2012. URL: `http://www.lib.ncsu.edu/resolver/1840.16/7583` (cit. on p. 93).

[121] E Humbert and A J Tosser. “Variations in the Curie temperature of electrodeposited NiP layers”. In: *Journal of Materials Science Letters* 7.2 (1998), pp. 167–168. ISSN: 02618028. DOI: `10.1023/A:1006507522246` (cit. on p. 96).

[122] Bosch Rexroth AG. *Instructions Linear Modules MKK / MKR / MLR*. 2010 (cit. on p. 97).

[123] MEWASA AG. *Membranbalgdaten axial*. 2014 (cit. on p. 97).

[124] Monroe Brothers Ltd. *PENeLOPE — Helium Vessel Pressure Relief*. Tech. rep. Monroe Brothers Ltd, 2012 (cit. on p. 97).

[125] Bosch Rexroth AG. *Rexroth IndraDrive Power Sections HCS01*. 2014 (cit. on p. 97).

[126] Bosch Rexroth AG. *Rexroth IndraDrive MPx-16 to MPx-20 and PSB Parameters*. 2015 (cit. on p. 97).

[127] MICRO-EPSILON Messtechnik GmbH & Co. KG. *Mounting Instructions mainSENSOR MDS-45-M18-SA*. Königbacher Str. 15, 94496 Ortenburg, Germany, 2013 (cit. on p. 99).

[128] L. Göltl et al. “An endoscopic detector for ultracold neutrons”. In: *European Physical Journal A* 49.1 (Jan. 2013), pp. 1–9. ISSN: 1434601X. DOI: `10.1140/epja/i2013-13009-8` (cit. on p. 104).

[129] Axel Reimer Müller. “Characterization of solid D2 as source material for ultra cold neutrons and development of a detector concept for the detection of protons from the neutron decay”. PhD thesis. Technische Universität München, 2008. URL: `http://mediatum.ub.tum.de/doc/672350/672350.pdf` (cit. on p. 105).

[130] A. R. Müller et al. “A low-temperature proton detector for a neutron lifetime experiment”. In: *Nuclear Instruments and Methods in Physics Research, Section A: Accelerators, Spectrometers, Detectors and Associated Equipment* 611.2-3 (2009), pp. 289–292. ISSN: 01689002. DOI: `10.1016/j.nima.2009.07.076` (cit. on p. 105).

[131] Christian Tietze. "Entwicklung eines Detektors zum Nachweis der Protonen aus dem β-Zerfall des Neutrons". Diploma thesis. Technische Universität München, 2009 (cit. on p. 105).

[132] Thomas Pöschl. "Detektion niederenergetischer Protonen aus dem freien Neutronenzerfall und Charakterisierung des Protonenbeschleunigers PAFF". Bachelor's thesis. Technische Universität München, 2012 (cit. on p. 105).

[133] Wolfgang Gebauer. "A Scintillator Based Proton Detector with Silicon Photomultiplier Readout for the Neutron Lifetime Experiment PENeLOPE". Diploma thesis. Technische Universität München, 2013 (cit. on p. 105).

[134] Christian Tietze. "PhD thesis—to be published 2017". PhD thesis. Technische Universität München, 2016 (cit. on p. 105).

[135] Hamamatsu Photonics K.K. *Delivery specification sheet Si APD Type No. S11048.* 2014 (cit. on pp. 105, 107).

[136] Dominik Steffen. "Self-Triggering Readout System with Advanced Online Data Processing for the Proton Detection of the Neutron Lifetime Experiment PENeLOPE". Master's thesis. Technische Universität München, 2014 (cit. on pp. 105, 112).

[137] Dominic Gaisbauer. "Development of the Front-end Electronics for the Proton Detection and Design of the Data Acquisition for the PENeLOPE Experiment". Master's thesis. Technische Universität München, 2015 (cit. on p. 105).

[138] N Pundak, C Geyari, and I Ben-Zvi. "Large diameter cryogenic seals". In: *Vacuum* 26.4-5 (1976), pp. 197–201. DOI: `10.1016/S0042-207X(76)80010-3` (cit. on p. 106).

[139] J. Bröcker. "Quellen systematischer Fehler bei der Messung der Neutronen-Lebensdauer mit einer magnetischen Flasche". Diplomarbeit. TU München, 2004 (cit. on p. 109).

[140] Tatsuo Tabata and Toshizo Shirai. "Analytic cross sections for collisions of H+, H2+, H3+, H, H2, and H- with hydrogen molecules". In: *Atomic Data and Nuclear Data Tables* 76.1 (2000), pp. 1–25. ISSN: 0092640X. DOI: `10.1006/adnd.2000.0835` (cit. on p. 109).

[141] William R. Leo. *Techniques for Nuclear and Particle Physics Experiments: A How-to Approach.* Second Rev. La Tour de Peilz, Switzerland: Springer-Verlag, 1994. ISBN: 978-3-540-57280-0. DOI: `10.1007/978-3-642-57920-2` (cit. on p. 111).

Acknowledgements

Special thanks go to

- Rüdiger Picker, for giving me the opportunity to start a scientific career in his group;
- Florian Haas, who sacrificed his private time and even his health to coordinate the mess we made;
- Stephan Paul, for providing for all the cool stuff I was allowed to play with and all the fun trips I was allowed to take;
- Stefan Materne and Andreas Senft, for setting up CoTEx 2.0, a great piece of equipment;
- Andreas Frei and Stephan Wlokka, for helping me out on UCN experiments and equipment;
- Thorsten Lauer and Thorsten Zechlau, for polarizing tips, parts, and beamtime;
- Thomas Deuschle and the UCN workshop crew, for repairing lots and lots of mishaps;
- Karin Frank, for taking care of all the boring administrative stuff;
- Peter Geltenbort and Thomas Brenner, for their support in all things ILL-related;
- Dominic Gaisbauer, Martin Losekamm, Michael Milde, and Thomas Pöschl, for keeping my spirit up;

and

- Albert and Susanne, for putting up with me for three decades and supporting me in each and every thing I did.